Electrical Conductivity of Grain Boundary in Accepter Doped Barium Zirconate

by

Susumu Imashuku

Department of Materials Science and Engineering,

Kyoto University

2009

Contents

Chapter 8

Effect of Cation Substitution on Conductivity and Microstructure of Sintered Barium Zirconate

Chapter 9

Processing of Fine Powder, Sintering Behavior and Grain-boundary Resistance for Yttrium-doped Barium Zirconate

Chapter 1

General Introduction

The broad objective of this work is to develop a firm understanding of the correlation among the thermodynamics, microstructure and conductivity of accepter doped barium zirconates, which are known to be as proton conductor, so as to allow the engineering of these compounds with the desired properties for the application in fuel cells. This work is particularly focused on proton conductivity in grain-boundary and dependence of dopant in barium zirconates.

This general introduction will provide a brief overview of fuel cells, structure of perovskite-type oxides, proton conduction mechanism and properties of barium zirconate.

1.1 Fuel Cells

A fuel cell is a device which converts chemical potential energy directly into electricity. W. Grove discovered a fuel cell in 1839. The Grove's fuel cell consists of platinum used as electrodes and dilutes sulfuric acid used as electrolyte using chemical reaction of hydrogen and oxygen.

Fuel cells can continually generate electricity by providing oxygen and a fuel such as hydrogen. Also, power generation efficiency of fuel cells is high because fuel cells do not pass though the form of heat energy during the conversion from chemical energy to electricity unlike thermal power generation system and nuclear power generation system. Due to these advantages, fuel cells are widely used for mobile devices such as laptop computers and mobile phones, vehicles such as automobiles and trains, and a power generation. Moreover, fuel cells are a clean energy source because they can reduce the emission of carbon dioxide (CO_2) and prevent the emission of nitrogen oxides (NO_x) and sulfur oxides (SO_x) which are

toxic for human beings. Thus, fuel cells are expected to be the best energy conversion device in 21st century.

Fuel cells are classified into several types according to the type of electrolytes used and the chemical reaction. There are five common types of fuel cells; polymer electrolyte membrane fuel cells (PEMFC), alkali fuel cells (AFC), phosphoric acid fuel cells (PAFC), molten carbonate fuel cells (MCFC) and solid oxide fuel cells (SOFC). An overview of these five types of fuel cells is summarized in Table 1.1, and a brief description of each in the following sections.[98Tag]

Table 1.1 Electrolyte, mobile ion species, operation temperature, fuels used and generating efficiency of five common types of fuel cells.

Type	Electrolyte	Mobile ion	Operating Temperature	Fuels	Generating efficiency
PEMFC polymer electrolyte membrane fuel cells	surfonated polymer	H^+	R.T.~100 °C	H_2, CH_3OH	30~40 %
AFC alkali fuel cells	potassium hydroxide	OH^-	100~250 °C	H_2	45~50 %
PAFC phosphoric acid fuel cells	phosphoric acid	H^+	160~190 °C	H_2	40~45 %
MCFC molten carbonate fuel cells	molten carbonate	CO_3^{2-}	600~700 °C	hydro-carbons	50~60 %
SOFC solid oxide fuel cells	yttria stabilized zirconia *etc*.	O^{2-}	900~1000 °C	hydro-carbons	55~70 %

Polymer Electrolyte Membrane Fuel Cells (PEMFC)

Polymer membrane which shows protonic conductivity is used as electrolyte, and an element in platinum group is used as catalyst. It is necessary for fuels of PEMFCs to be contained moisture because water molecules travel from the anode to cathode in the process of proton conduction. Thus, the operating temperature under 1 atm is limited to less than 100 °C. PEMFCs are being developed for automobiles and portable electric devices.

Alkali Fuel Cells (AFC)

Alkaline aqueous solution such as potassium hydroxide (KOH) solution is used as electrolyte within inert electrodes. AFCs have the most simple structure among fuel cells and operated at temperatures of 100 ~ 250 °C. Cheap electrocatalyst can be used, and it is possible to simplify the cell structure because aqueous solution is used in AFCs. Due to these advantages, AFCs are practically used in spacecrafts. However, it is necessary to use very pure oxygen gas as oxidant because carbon dioxide in air reacts with electrolyte and forms solid, non-conducting alkaline carbonate.

Phosphoric Acid Fuel Cells (PAFC)

Phosphoric acid (H_3PO_4) solution is used as electrolyte, and operating temperatures are in the range of 160 to 190 °C. Catalysts of PAFCs are poisoned in the presence of high concentration of carbon monoxide (CO) although it is better than PEMFC. Thus, when hydrocarbon gas such as natural gas and coal gas is used as a fuel, steam reforming and carbon monoxide conversion are needed. PAFCs are already commercially available as a co-generation system in factories and buildings (100 ~ 200 kW).

Molten Carbonate Fuel Cells (MCFC)

Molten carbonate such as lithium carbonate (Li_2CO_3) and potassium carbonate (K_2CO_3) is used as electrolyte, and carbonate ions travel in the electrolyte. MCFCs are operated at temperatures of 600 to 700 °C. Because of these high operating temperatures, platinum catalysts are not needed. Thus, catalysts of MCFCs are not poisoned in the presence of carbon monoxide, and it is possible to use not only hydrogen gas but also hydrocarbon gas as a fuel. MCFCs also have the advantage that it is possible to use waste heat efficiently.

Solid Oxide Fuel Cells (SOFC)

Oxide ion conductive oxides such as yttria stabilized zirconia (YSZ) and lanthanum gallate ($LaGaO_3$) are used as electrolyte, and operating temperature are in the range of 700 to

1000 °C. As MCFCs, because of the high operating temperature, platinum catalysts are not needed and hydrocarbon gas can be used as a fuel, but SOFCs need high heat-resistant materials which cause the cost of SOFCs very high. Power generation efficiency of SOFCs is the highest among other four types of fuel cells (55 ~ 70 %). It is possible to achieve 80 % as energy efficiency using waste heat. Thus, SOFCs are being developed for domestic and industrial power generators.

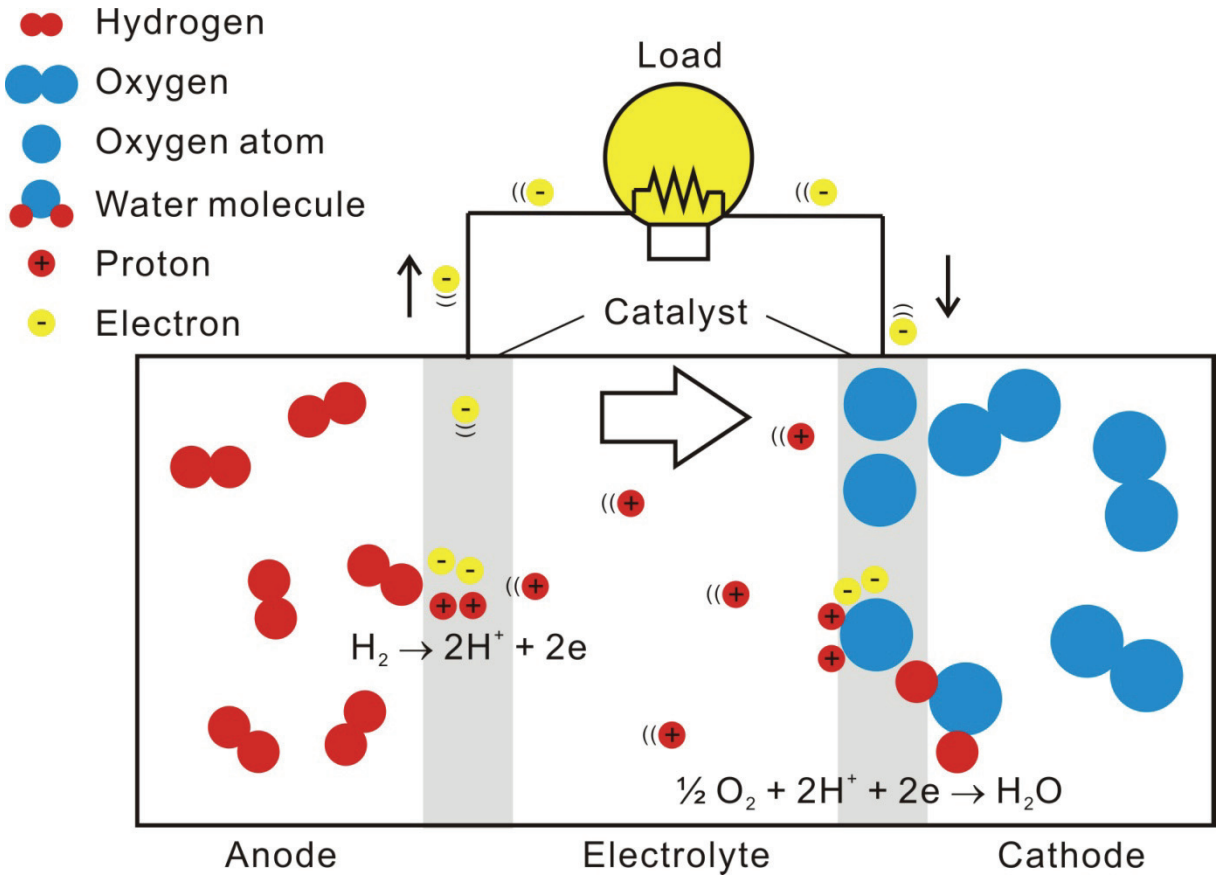

Figure 1.1 Schematic view of a fuel cell using proton conductive electrolytes.

High energy efficiency is required for fuel cells from the viewpoint of energy conservation. From that point, SOFCs are the most promising fuel cell, but as described above, SOFCs need high heat-resistant materials which are high-cost. One of the solutions of the problem is to make the operating temperatures lower to the extent where common materials

such as stainless steel can be used. The object of this work is to decrease the operating temperature of SOFCs to 500 °C by substituting the electrolyte from oxide ion conductive oxides to proton conductive oxides. Fig. 1.1 shows the schematic view of a fuel cell in which proton conductive oxides is used. Among proton conductive oxides, I focused on perovskite-type oxides which show protonic conduction.

1.2 Structure of Perovskite-type Oxides[98Tag]

The name "perovskite" derives from the mineral of calcium titanium oxide ($CaTiO_3$), "perovski", named after a Russian mineralogist, Count Lev Aleksevich Perovski. Later, the name "perovskite" is used for a group of oxides described as a general formula of ABO_3. Unit cell of perovskite structure can be expressed using cesium chloride (CsCl) type primitive cubic lattice. The atomic positions of unit cell in cesium chloride are Cs^+ (0, 0, 0) and Cl^- $(\frac{1}{2},\frac{1}{2},\frac{1}{2})$. Perovskite structure can be described by replacing cesium ion (Cs^+) by B-site cation and chloride anion (Cl^-) by A-site cation, and by arranging oxide ion at between two B-site cations. Coordination numbers of A-site and B-site cations are twelve and six, respectively. The ideal unit cell of perovskite is a primitive cubic lattice, but some perovskite-type oxides have rhombohedron, hexagonal and orthorhombic structures.

There are two ways to describe the structure of perovskite. One is to make a primitive cubic lattice of B-site cation, and arrange A-site cation at the center of the lattice and oxide ion at between B-site cations. This arrangement is called A-type arrangement. The other is to make a primitive cubic lattice of A-site cation, and arrange B-site cation at the center of the lattice and oxide ion at the position of face center positions of the lattice. This arrangement is called B-type arrangement. By moving atoms of A-type arrangement to $(\frac{1}{2},\frac{1}{2},\frac{1}{2})$ in parallel, the structure becomes B-type arrangement. The structures of cubic perovskite of A-type and B-type arrangement are shown in Fig. 1.2 (a) and (b), respectively. Perovskite structure is

formed by the stack of two atomic layers as viewed from the direction of [1,1,1]. One layer consists of A-site cation and oxide ion, and the other consists of B-site cation.

The structure of perovskite is the most stable when the summation of valences in A-site and B-site cation is six. A-site can be either monovalent cation (Na^{+}, K^{+}, etc.), divalent cation (Ca^{2+}, Sr^{2+}, Ba^{2+}, etc.) or trivalent cation (La^{3+}, etc.) and B-site can be occupied by pentad cation (Nb^{5+}, W^{5+}, etc.), tetravalent cation (Ce^{4+}, Ti^{4+}, etc.) or trivalent cation (Mn^{3+}, Cr^{3+}, Co^{3+}, etc.). In general, alkali metal cations or alkali earth metal cations are in A-site of perovskite structure, and transition metal cations occupy B-site of perovskite structure because ionic radius of A-site cation is larger than that of B-site cation. Characteristics of perovskite-type oxides are that (1) they are structurally stable even if vacancies of A-site cation or oxide ion forms, (2) it is possible to substitute other metal cations for either A-site cation or B-site cation and (3) they allow nonstoichiometric composition by the absence of A-site cation or oxide ion and their nonstoichiometric composition range is generally wide.

1.3. Proton Conductivity

Protonic conduction of perovskite-type oxides were first reported by *Iwahara et al*. on trivalent cation (Yb^{3+}, Y^{3+}, Sc^{3+}) doped strontium cerate ($SrCeO_3$). [81Iwa,83Iwa] Then, they reported that neodymium (Nd^{3+}) doped barium cerate ($BaCeO_3$), indium (In^{3+}) doped calcium zirconate ($CaZrO_3$), indium (In^{3+}) and yttrium (Y^{3+}) doped strontium zirconate ($SrZrO_3$) and trivalent cation (Ga^{3+}, In^{3+}, Y^{3+}, Dy^{3+}, Nd^{3+}) doped barium zirconate ($BaZrO_3$) also show protonic conduction. [88Iwa.93Iwa] Dopant cation is needed for protonic conduction of perovskite-type oxides.

Doping trivalent cation (M(III)) into the B(IV) site forms oxide ion vacancy as given in Eq. (1-1)

$$2B_B^{\times} + O_O^{\times} + M_2O_3 \rightarrow 2M_B' + V_O^{\cdot\cdot} + 2BO_2 \qquad (1\text{-}1)$$

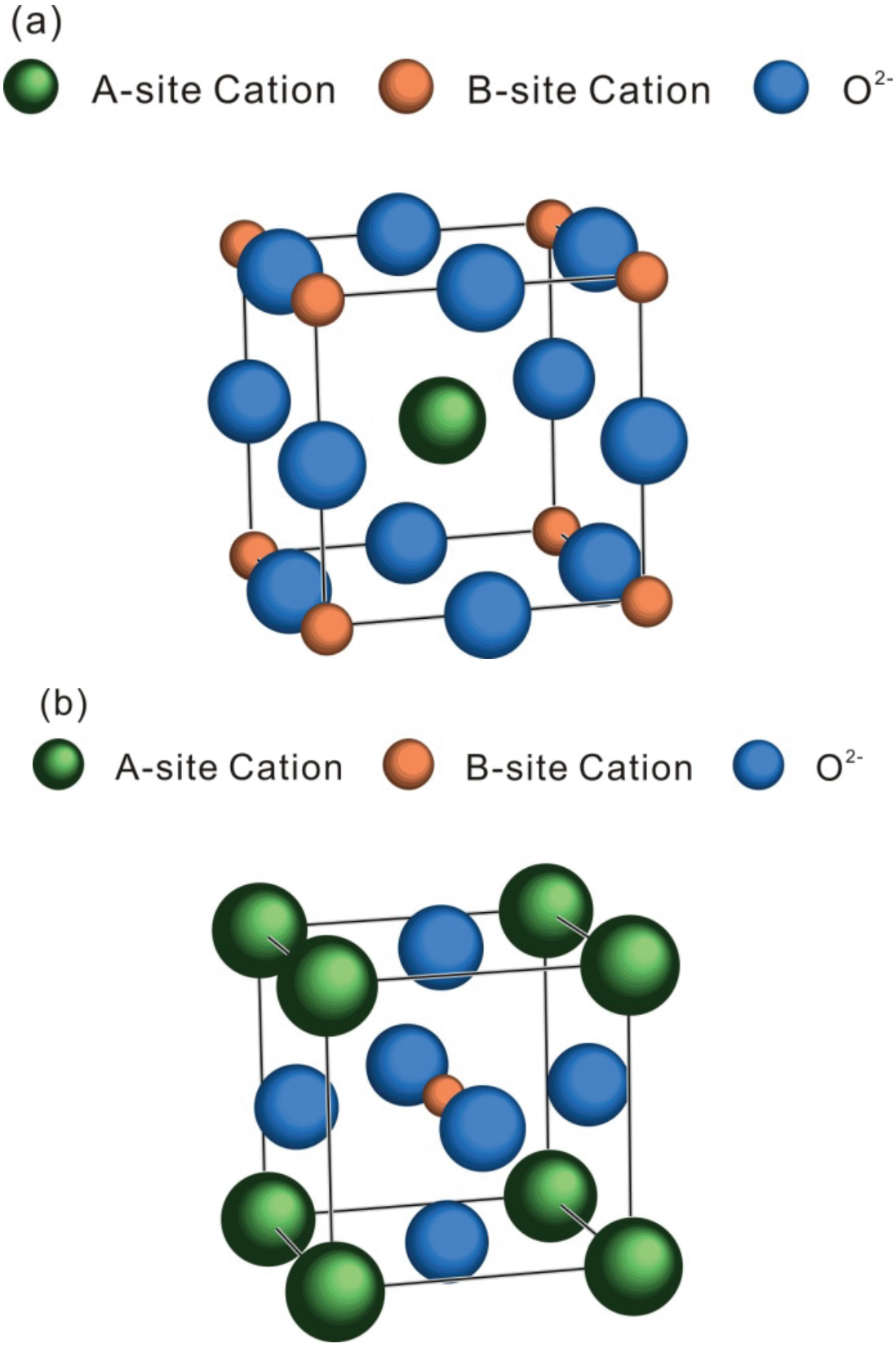

Figure 1.2 Structures of cubic perovskite of (a) A-type and (b) B-type arrangement

where the equation is written by Kröger-Vink notation. Then, water from the gas phase dissociates into a hydroxide ion and a proton. The hydroxide ion fills an oxide ion vacancy, and the proton forms a hydroxide ion with lattice oxygen. This reaction can be written by Eq. (1-2).

$$H_2O\,(gas) + V_O^{\cdot\cdot} + O_O^{\times} = 2OH_O^{\cdot} \quad (1\text{-}2)$$

Consequently, protons are introduced in the perovskite-type oxide where the trivalent cation is doped under wet conditions. This proton shows protonic conduction by rotating around an oxygen ion and jumping in the network of oxygen ions.

There is a possibility that other spices such as oxide ion, hole and electron are mobile in perovskite-type oxides. At a high oxygen partial pressure, oxygen vacancies react with oxygen molecules to produce holes like Eq. (1-3).

$$\frac{1}{2}O_2\,(gas) + V_O^{\cdot\cdot} = O_O^{\times} + 2h^{\cdot} \quad (1\text{-}3)$$

At a low oxygen partial pressure, oxygen ions in perovskite-type oxides decompose oxygen vacancies and oxygen gas to produce electrons like Eq. (1-4).

$$O_O^{\times} = \frac{1}{2}O_2\,(gas) + V_O^{\cdot\cdot} + 2e' \quad (1\text{-}4)$$

According to Eq. (1-3) and (1-4), the concentration of the mobile species in perovskite-type oxides can be expressed as

$$[h^{\cdot}] = K_1^{\frac{1}{2}}\,[V_O^{\cdot\cdot}]^{\frac{1}{2}}\,p_{O_2}^{\frac{1}{4}} \quad (1\text{-}5)$$

$$[e'] = K_2^{\frac{1}{2}}\,[V_O^{\cdot\cdot}]^{-\frac{1}{2}}\,p_{O_2}^{-\frac{1}{4}} \quad (1\text{-}6)$$

where K_1 and K_2 are the equilibrium constants of Eq.s (1-3) and (1-4), and $[h^{\cdot}]$, $[e']$ and $[V_O^{\cdot\cdot}]$ are the concentration of hole, electron and oxygen ion vacancy, respectively, and p_{O_2} is the oxygen partial pressure. Generally, at moderate temperatures, mobility of electron is the highest, and following hole, proton and oxide ion. Thus, there is a possibility that hole is the predominant specie of conduction at a high oxygen partial pressure and that electron at a low

oxygen partial pressure. Actually, it was reported that hole conduction of doped barium zirconates was dominant in wet air atmosphere.[00Boh,00Sch,01Sch,01Gor,05Wan,05Sha,07Tao,07Nom] But, electron conduction at a low oxygen partial pressure has not been reported. Also, oxygen ion conduction becomes dominating at higher temperature where dehydration of perovskite-type oxides occurs. It was reported that proton concentration of doped barium zirconate decreased at higher temperature.[00Sch,01Kre,06Ahm,06Tao,07Ahm,07TaO] In this way, predominant mobile species depend on oxygen partial pressure and temperature. In case of doped barium zirconates, protonic conduction is significant at intermediate temperature (400 ~ 600 °C) and low oxygen partial pressure (p_{O_2} < 10^{-4} atm). [93Iwa,07Nom]

1.4 Doped Barium Zirconate

Yttrium doped barium cerate exhibits the highest proton conductivity (about 10^{-2} S cm^{-1} at 600 °C in wet hydrogen[00Kat]) among the perovskite-type oxides which shows protonic conduction, and their application is anticipated for proton conductive electrolytes in fuel cells or steam electrolyzers. However, doped barium cerates decompose to barium carbonate ($BaCO_3$) and ceria (CeO_2) under atmosphere in the presence of carbon dioxide (CO_2).[93Gop,93Sch] Thus, it is difficult to apply the doped barium cerates for electrolytes in fuel cells.

In contrast, doped barium zirconates are more thermodynamically stable than doped barium cerates.[99Ryu] Fig. 1.3 shows the Gibbs energy change of hydrolysis reaction in barium cerate and barium zirconate at p_{H_2O} = 0.05 atm, and Fig. 1.3 (a) and (b) show the Gibbs energy change of carbonate formation reaction in barium cerate and barium zirconate at p_{CO_2} = 4 × 10^{-5} and 0.25 atm, respectively.[95Bar] It is clear that barium zirconate is much more stable than barium cerate in the presence of water and carbon dioxide. Therefore, barium zirconate has a great potential for proton conductive electrolytes in fuel cells or steam

electrolyzers. At early studies of doped barium zirconates, it was reported that this materials had poor proton conductivity.[93Iwa,93Man,95Sla,97Wie,99Ryu,01Gor] However, Kreuer *et. al.* reported that yttrium-doped barium zirconate had relatively high proton conductivity even at 140 °C (5 × 10^{-5} S cm^{-1})[99Kre] and then Bohn *et. al.* confirmed the high proton conductivity of yttrium-doped barium zirconate at high temperatures (3 × 10^{-3} S cm^{-1} at 600 °C in wet hydrogen). [00Boh] After their reports, many researchers are working on yttrium-doped barium zirconate and agreed that it exhibited high proton conductivity. [00Sch,01Kre,03Kre,05Wan,06Igu,07TaO,07Nom,07Bab, 07Duv,07Igu,07Ser,08Aza,08Ito] But, some researchers reported that proton conductivity of yttrium-doped barium zirconate is still low. [02Lai,03Sch,04Sni,05Sav] These differences in proton conductivity is connected to the difficulty in sintering of doped barium zirconates.[03Kre] Even if the proton conductivity reported by Kreuer *et. al.* and Bohn *et. al.* is true, the proton conductivities of yttrium-doped barium zirconates are quite low for application as an electrolyte in fuel cells.

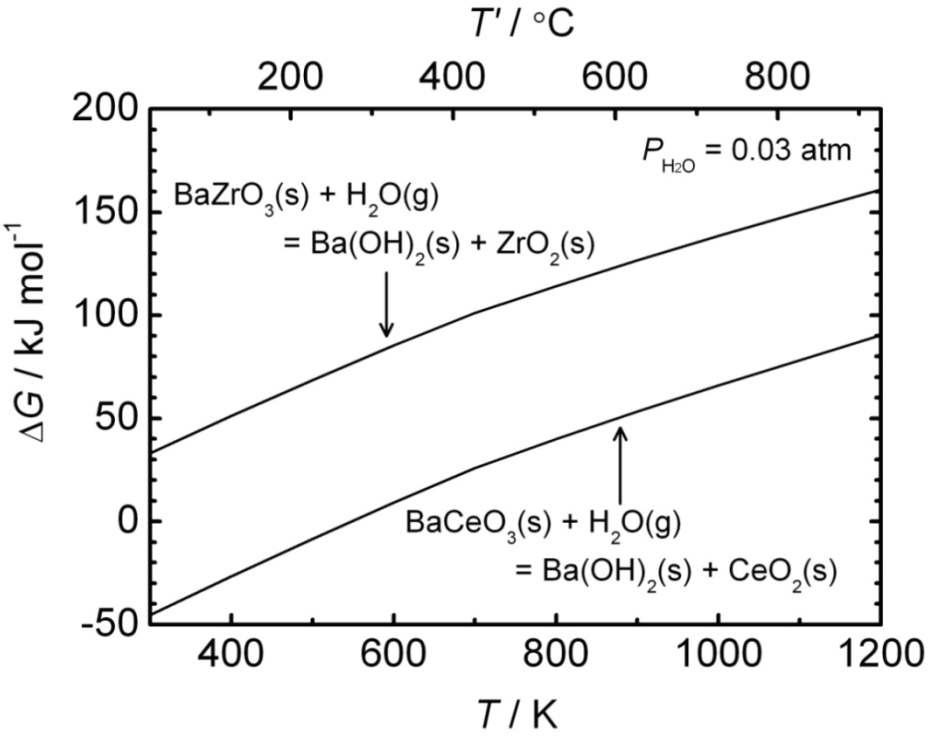

Figure 1.3 Gibbs energy change of hydrolysis reaction in barium cerate and barium zirconate at p_{H_2O} = 0.05 atm.

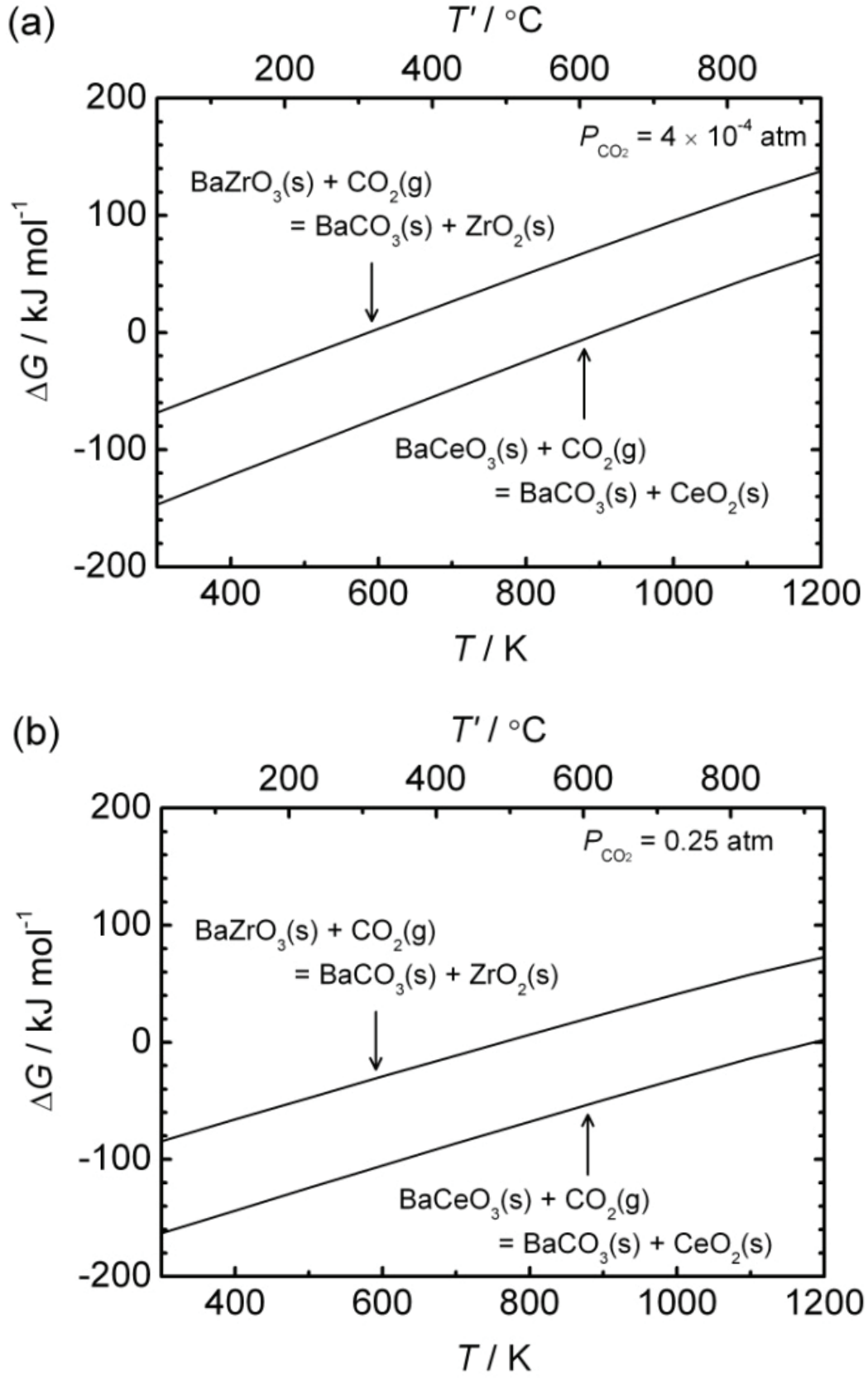

Figure 1.4 Gibbs energy change of carbonate formation reaction in barium cerate and barium zirconate at (a) p_{CO_2} = 4 × 10^{-4} atm and (b) p_{CO_2} = 0.25 atm.

It is necessary to investigate the discrepancy of proton conductivities of yttrium-doped barium zirconates and improve the low conductivity as application for electrolytes in fuel cells. Alternating current (AC) impedance spectroscopy is a powerful method for the answer because it is possible to calculate the resistance of bulk (grain-interior) and grain-boundary separately. In Chapter 2, we interprets impedance spectra obtained in AC 2-terminal measurement by combining with the results of DC 4-terminal measurement, and established the way of deciding a bulk and grain-boundary resistance of 15 % yttrium-doped barium zirconate by AC 2-terminal measurement.

Yttrium-doped barium zirconate has the highest bulk conductivity among the trivalent cation doped barium zirconates. On the other hand, reports on other trivalent cation doped barium zirconates are relatively limited. Thus, there might be a dopant which has higher proton conductivity than yttrium. In Chapter 3, we investigated various dopants from the viewpoint of microstructure and proton conductivity.

From the results of Chapter 3, we can classify trivalent cation doped barium zirconates into two classes from the viewpoints of development of microstructure and proton conductivity; “Y-type” dopant and “Sc-type” dopant. We assume that kinetic reason of cation diffusion, and the difference of phase relationship between the synthesizing temperature, 1300 °C, and sintering temperature, 1600 °C, have an influence on the microstructures of trivalent cation doped barium zirconates. First, we investigate phase relationship at sintering temperature, 1600 °C by establishing pseudoternary phase diagram of the BaO-ZrO_2-$MO_{1.5}$ system (M=Y and Sc). Chapter 4 and 5 deal with BaO-ZrO_2-$YO_{1.5}$ system and BaO-ZrO_2-$ScO_{1.5}$ system, respectively. Then, we speculate the phase relationship at synthesizing temperature, 1300 °C, by XRD analysis of scandium-doped barium zirconate and observation of a trace of phase separation in yttrium-doped barium zirconate heat-treated at 1600 °C.

After that, we investigate microstructures of $BaZr_{0.85}Y_{0.15}O_{3-\delta}$ and $BaZr_{0.85}Sc_{0.15}O_{3-\delta}$ by changing sintering time. Chapter 6 describes the details.

From the results of Chapter 3, we figured out that grain-boundary resistance is higher than bulk resistance and that total resistance is governed by grain-boundary resistance. Grain-boundary resistance is the product of number of grain-boundaries perpendicular to the direction of current flow and inverse of specific grain-boundary conductivity. Therefore, the grain-boundary concentration has to be reduced to improve the grain-boundary resistance, which means that it is necessary to have large grains of barium zirconate. From the results of Chapter 6, it is difficult to obtain well-grown grains of yttrium-doped barium zirconate which has the highest bulk conductivity among the trivalent cation doped barium zirconates because of the difference of phase relationship between the sintering temperature (1600 °C) and a synthesizing temperature (1300 °C) and kinetic reason of cation diffusion during sintering. In order to obtain large grains of yttrium-doped barium zirconate, we attempt three methods. First method is to co-dope scandium into yttrium co-doped barium zirconate. When scandium is doped into barium zirconate, the grains grow well. Thus, there is a possibility that we can obtain large grains of yttrium-doped barium zirconate by co-doping scandium. The details are discussed in Chapter 7. The second is to substitute A site ion or B site ion in yttrium-doped barium zirconate for isovalent cation. Chapter 8 describes the details. Third one is to obtain very fine synthesized powder as it is not necessary for cation to diffuse long distance during sintering. Chapter 9 deals with this method.

References

[81Iwa] H. Iwahara, T. Esaka, H. Uchida, and N. Maeda, *Solid State Ionics*, **3-4**, 359-363 (1981).

[83Iwa] H.Iwahara, H.Uchida, and S.Tanaka, *Solid State Ionics*, **9-10** (3), 1021-1026 (1983).

[88Iwa] H. Iwahara, H. Uchida, K. Ono, and K. Ogaki, *Journal of the Electrochemical Society*, **135,** 529-533 (1988).

[93Iwa] H. Iwahara, T. Tajima, T. Hibino, K. Ozaki, and H. Suzuki, *Solid State Ionics*, **61**, 65-69 (1993).

[93Gop] S. Gopalan and A.V. Virkar, *Journal of the Electrochemical Society*, **140** [4], 1060-1065 (1993).

[93Sch] M.J. Scholten, j. Schoonman, J.C.van Miltenburg, and H.A.J. Oonk, *Solid State Ionics*, **61**, 83-91 (1993).

[93Man] A. Manthiram, J.F. Kuo, and J.B. Goodenough, *Solid State Ionics*, **62**, 225-234 (1993).

[95Bar] I. Barin, *Thermochemical Data of Pure Substances,* 3rd ed., VCH Verlagsgesellschaft mbH, Weinheim (1995).

[95Sla] RCT. Slade, S.D. Flint, and N. Singh, *Solid State Ionics*, **82**, 135-141 (1995).

[97Wei] S. Wienstrijer and H.D. Wiemhijfer, Solid State Ionics, **101-103**, 1113-1117 (1997).

[98Tag] H. Tagawa, *Kotaisanngabutsu Nennryoudennchi to Chikyukannkyo*, Agune-shouhuusha, Tokyo (1998).

[99Ryu] K.H. Ryu and S.M Haile, *Solid State Ionics*, **125**, 355–367 (1999).

[99Kre] K. D. Kreuer, *Solid State Ionics*, 125, 285-302 (1999).

[00Kat] K. Katahira, Y. Kohchi, T. Shimura and H. Iwahara, *Solid Stae Ionics*, **138**, 91-98 (2000).

[00Boh] H. G. Bohn and T. Schober, *Journal of the American Ceramic Society*, **83,** 768-772 (2000).

[00Sch] T. Schober, and H.G. Bohn, *Solid State Ionics*, **127**, 351-360 (2000).

[01Sch] T. Schober, *Solid State Ionics*, **139**, 95-104 (2001).

[01Gor] V.P. Gorelov, V.B. Balakireva, Y.N. Kleschchev, and V.P. Brusentsov, *Inorganic Materials*, **37** [5], 535-538 (2001).

[01Kre] K. D. Kreuer, S. Adams, W. Munch, A. Fuchs, U. Klock, and J. Maier, *Solid State Ionics,* **145,** 295-306 (2001).

[02Lai] M. Laidoudi, I.A. Talib, and R. Omar, *Journal of Physics D: Applied Physics*, **35,** 397-401 (2002).

[03Kre] K.D. Kreuer, *Annual Review of Materials Research,* **33**, 333-359 (2003).

[03Sch] T. Schneller, T. Schober, *Solid State Ionics*, **164**, 131-136 (2003).

[04Sni] F.M.M. Snijkers, A. Buekenhoudt, J. Cooymans, and J.J. Luyten, *Scripta Materialia*, **50,** 655-659 (2004).

[05Wan] W. S. Wang and A. V. Virkar, *Journal of Power Sources*, **142,** 1-9 (2005).

[05Sha] N.V. Sharova and V.P. Gorelov, *Russian Journal of Electrochemistry,* **41** [10], 1130-1134 (2005).

[05Sav] C.D. Savaniu, J.C. Vazquez and J.T.S. Irvine, *Journal of Materials Chemistry*, 15, 598-604 (2005).

[06Ahm] I. Ahmed, S.G. Eriksson, E. Ahlberg, C.S. Knee, P. Berastegui, L.G. Johansson, H. Rundlöf, M. Karlsson, A. Matic, M. Karlsson, L. Börjesson, and D. Engberg, *Solid State Ionics*, **177**, 1395-1403 (2006).

[06Tao] S. Tao and J.T.S. Irvine, *Advanced Materials*, **18**, 1581-1584 (2006).

[06Igu] F. Iguchi, T. Yamada, N. Sata, T. Tsurui, and H. Yugami, *Solid State Ionics,* **177,** 2381-2384 (2006).

[07Tao] S. Tao and J.T.S. Irvine, *Journal of Solid State Chemistry*, **180**, 3493-3503 (2007).

[07Ahm] I. Ahmed, S.G. Eriksson, E. Ahlberg, C.S. Knee, H. Götlind, L.G. Johansson, M. Karlsson, A. Matic, and L. Börjesson, *Solid State Ionics*, **178**, 515-520 (2007).

[07Nom] K. Nomura and H. Kageyama, *Solid State Ionics,* **178**, 661-665 (2007).

[07Bab] P. Babilo, T. Uda and S. M. Haile, *Journal of Materials Research*, **22,** 1322-1330 (2007).

[07Duv] S.B.C. Duval, P. Holtappels, U.F. Vogt, E. Pomjakushina, K. Conder, U. Stimming, and T. Graule, *Solid State Ionics,* **178**, 1437-1441 (2007).

[07Igu] F. Iguchi, N. Sata, T. Tsurui, and H. Yugami, *Solid State Ionics,* **178**, 691-695 (2007).

[07Ser] J.M. Serraw, and W.A. Meulenberg, *Journal of the American Ceramic Society*, 90 [7], 2082-2089 (2007).

[08Aza] A.K. Azad, C. Savaniu, S. Tao, S. Duval, P. Holtappels, R.M. Ibberson, and J.T. S. Irvine, *Journal of Materials Chemistry*, **18**, 3414-3418 (2008).

[08Ito] N. Ito, H. Matsumoto, Y. Kawasaki, S. Okada, T. Ishihara, *Solid State Ionics*, **179**, 324-329 (2008).

Chapter 2

Identification of Electrolyte Resistance in AC Impedance Spectroscopy

2.1 Introduction

In this chapter, we interpret impedance spectra obtained in AC 2-terminal measurement by combining with the results of DC 4-terminal measurement, and established the way of deciding a bulk and grain-boundary resistance of 15 % yttrium-doped barium zirconate by AC 2-terminal measurement.

2.2 AC Impedance Spectroscopy

Alternating current (AC) impedance spectroscopy is a powerful method of evaluating the conductivity of ionic conductors in polycrystalline materials. There are several advantages of this method such that it is possible to eliminate the influence of the polarization of electrodes, which means that nonblocking electrodes do not need for this method, and that it is often possible to calculate the resistance of bulk (grain-interior) and grain-boundary separately.

Impedance spectrum of an ideal polycrystalline material and the corresponding equivalent circuit are shown as Fig. 2.1. There usually appear three arcs which are from the behavior in bulk and grain-boundary of electrolyte and in electrodes by the difference of their capacitances. As the capacitances of the arcs are smaller, the arcs appear at higher frequency, and the diameter of each arc corresponds to its resistance in the following reason.

When an AC voltage, $V(t) = V_0 \mathrm{e}^{\mathrm{i}\omega t}$, is applied to a circuit which consists of a resister and capacitor in parallel such as Fig. 2.2, a current in the resister, $I_\mathrm{R}(t)$, will be,

$$I_\mathrm{R}(t) = \frac{V_0 \mathrm{e}^{\mathrm{i}\omega t}}{R} = \frac{V(t)}{R} \tag{2-1}$$

and a current in the capacitor, $I_\mathrm{C}(t)$, will be,

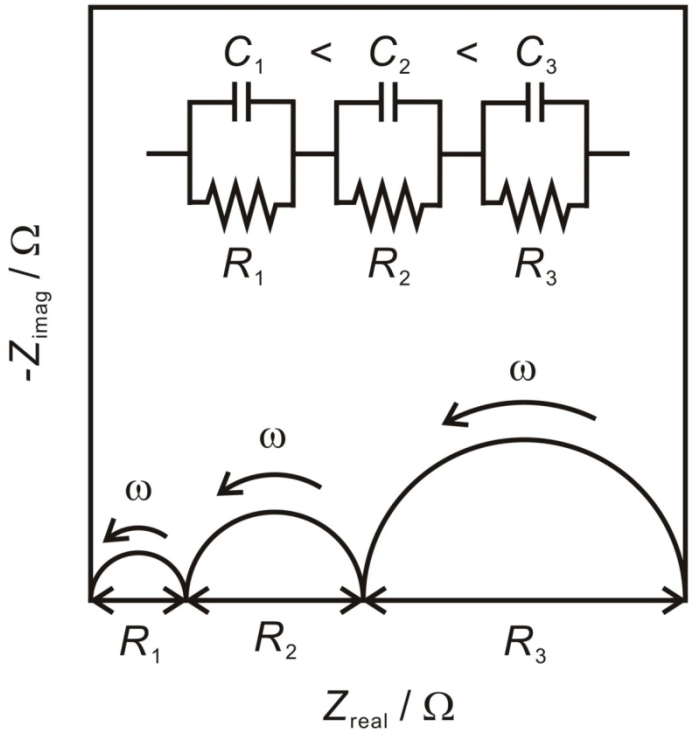

Figure 2.1 Impedance spectrum of an ideal polycrystalline material and the corresponding equivalent circuit.

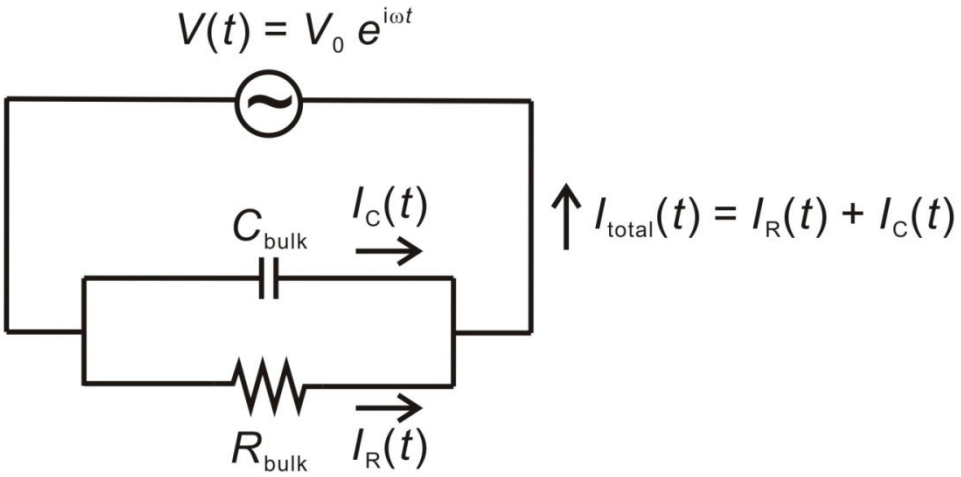

Figure 2.2 Circuit which consists of a resister and capacitor in parallel and applied AC voltage.

$$I_{\mathrm{C}}(t) = \frac{\mathrm{d}Q(t)}{\mathrm{d}t} = \frac{\mathrm{d}(CV(t))}{\mathrm{d}t} = \frac{\mathrm{d}(CV_0\mathrm{e}^{\mathrm{i}\omega t})}{\mathrm{d}t} = \mathrm{i}\omega CV_0\mathrm{e}^{\mathrm{i}\omega t} = \mathrm{i}\omega CV(t) \qquad (2\text{-}2)$$

Then, the total current, $I_{\mathrm{total}}(t)$ in the circuit will be,

$$I_{\mathrm{total}}(t) = I_{\mathrm{R}}(t) + I_{\mathrm{C}}(t) = \frac{V(t)}{R} + \mathrm{i}\omega CV(t) \qquad (2\text{-}3)$$

The complex impedance, Z, which is defined as the ratio of the voltage to current can be written as,

$$Z = \frac{V(t)}{I_{\text{total}}(t)} = \frac{V(t)}{\frac{V(t)}{R} + \mathrm{i}\omega C V(t)} = \frac{1}{\frac{1}{R} + \mathrm{i}\omega C} = \frac{\frac{1}{R} - \mathrm{i}\omega C}{(\frac{1}{R})^2 + (\omega C)^2} \quad (2\text{-}4)$$

The complex impedance, Z, can be separated into its real, Z', and imaginary, Z'', parts like

$$Z = Z' + \mathrm{i}Z'' = \frac{\frac{1}{R}}{(\frac{1}{R})^2 + (\omega C)^2} + \mathrm{i}\frac{(-\omega C)}{(\frac{1}{R})^2 + (\omega C)^2} \quad (2\text{-}5)$$

Subsequently, the value, $\left(Z' - \frac{R}{2}\right)^2 + Z''^2$, will lead to,

$$\left(Z' - \frac{R}{2}\right)^2 + Z''^2 = \left(\frac{R}{2}\right)^2 \quad (2\text{-}6)$$

The Eq. (2-6) means that the complex impedance, Z, shows a circle whose center is $\left(\frac{R}{2},\ 0\right)$ and radius is $\frac{R}{2}$ on complex plane. Therefore, the diameter of arc corresponds to resistance, R, in the RC circuit.

The bulk conductivity, σ_{bulk}, and specific grain-boundary conductivity, $\sigma^{\circ}_{\text{g.b.}}$, can be calculated from macrostructure and microstructure information using "brick layer model".[98Hai] At the brick layer model, a polycrystalline material consists of cubic grains whose size is G, grain-boundary whose thickness is g and electrodes as shown in Fig. 2.3 (a) where L is the sample length and S is the sample cross sectional area. Also, at the assumption that bulk conductivity is much larger than specific grain-boundary conductivity ($\sigma_{\text{bulk}} \gg \sigma^{\circ}_{\text{g.b.}}$), ions only go through the path which consists of bulk and grain-boundary as like arrows in Fig. 2.3 (a), and the equivalent circuit of the brick layer model can be drawn as Fig. 2.3 (b). Usually, grain size is much larger than grain-boundary thickness ($G \gg g$), so the length of bulk, L_{bulk}, and grain-boundary, $L_{\text{g.b.}}$, and the cross sectional area for the perpendicular direction to ion flow of bulk, S_{bulk}, and grain-boundary, $S_{\text{g.b.}}$, can be written as

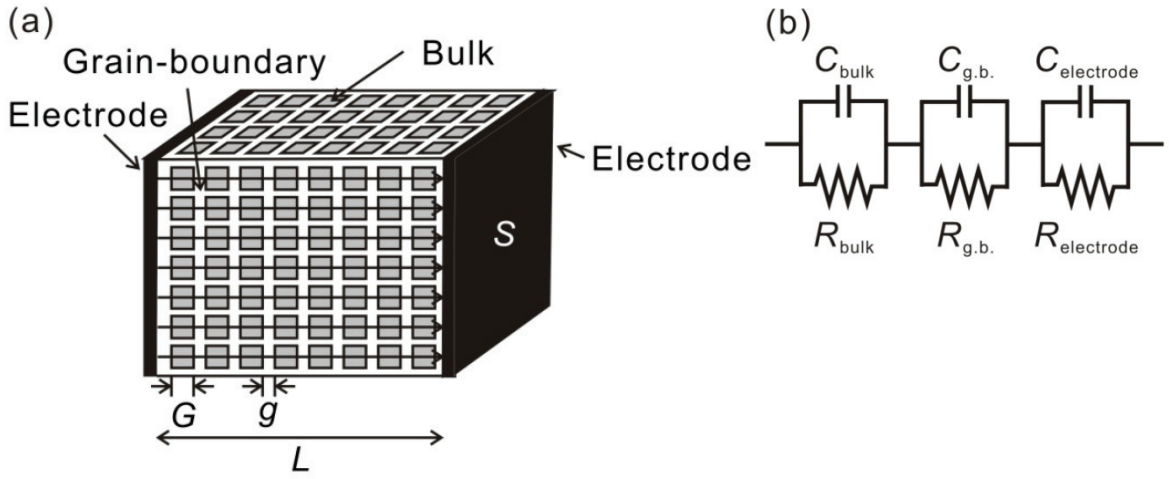

Figure 2.3 (a) Brick layer model of a polycrystalline material and (b) the equivalent circuit of brick layer model in a polycrystalline material.

$$L_{\text{bulk}} = \frac{G}{G+g} L \approx L \tag{2-7}$$

$$L_{\text{g.b.}} = \frac{g}{G+g} L \approx \frac{g}{G} L \tag{2-8}$$

$$S_{\text{bulk}} = \left(\frac{G}{G+g}\right)^2 S \approx S \tag{2-9}$$

$$S_{\text{g.b.}} = S \tag{2-10}$$

Thus, the resistance of bulk, R_{bulk}, and grain-boundary, $R_{\text{g.b.}}$, and the capacitance of bulk, C_{bulk}, and grain-boundary, $C_{\text{g.b.}}$, can be described as

$$R_{\text{bulk}} = \frac{L_{\text{bulk}}}{S_{\text{bulk}}} \frac{1}{\sigma_{\text{bulk}}} = \frac{L}{S} \frac{1}{\sigma_{\text{bulk}}} \tag{2-11}$$

$$R_{\text{g.b.}} = \frac{L_{\text{g.b.}}}{S_{\text{g.b.}}} \frac{1}{\sigma^{\circ}_{\text{g.b.}}} = \frac{L}{S} \frac{g}{G} \frac{1}{\sigma^{\circ}_{\text{g.b.}}} \tag{2-12}$$

$$C_{\text{bulk}} = \frac{S_{\text{bulk}}}{L_{\text{bulk}}} \varepsilon_{\text{bulk}} \epsilon_0 = \frac{S}{L} \varepsilon_{\text{bulk}} \epsilon_0 \tag{2-13}$$

$$C_{\text{g.b.}} = \frac{S_{\text{g.b.}}}{L_{\text{g.b.}}} \varepsilon_{\text{g.b.}} \epsilon_0 = \frac{S}{L} \frac{G}{g} \varepsilon_{\text{g.b.}} \epsilon_0 \tag{2-14}$$

Where $\varepsilon_{\text{bulk}}$ is the dielectric constant of bulk, $\varepsilon_{\text{g.b.}}$ is the dielectric constant of grain-boundary and ε_0 is the electric constant, respectively. Also, at the assumption that dielectric constant of

bulk is almost the same as that of grain-boundary ($\varepsilon_{bulk} \approx \varepsilon_{g.b.}$), we can obtain the following equation from the Eq. (2-13) and (2-14),

$$\frac{g}{G} = \frac{C_{\mathrm{bulk}}}{C_{\mathrm{g.b.}}} \tag{2-15}$$

Then, Eq. (2-12) can be rewritten using Eq. (2-15) as

$$R_{\mathrm{g.b.}} = \frac{L}{S} \frac{C_{\mathrm{bulk}}}{C_{\mathrm{g.b.}}} \frac{1}{\sigma^{\circ}_{\mathrm{g.b.}}} \tag{2-16}$$

Therefore, the bulk and specific grain-boundary conductivity can be calculated from only macrostructure information.

2.3 Experimental

2.3.1 Material Preparation

Crystalline powder of 15 % yttrium-doped barium zirconate ($BaZr_{0.85}Y_{0.15}O_{3-\delta}$) was synthesized by conventional solid-state reaction from barium carbonate ($BaCO_3$: 99.9%, Wako), zirconia (ZrO_2: 97.97% including 2% of hafnium, Tosoh) and yttria (Y_2O_3: 99.9 %, Shin-Etsu Chemical) based on a reported method.[07Bab] All the raw materials except for barium carbonate were heated at 800 °C for more than 10 hours to remove moisture prior to weighting. Raw materials were ball-milled for 24 hours using yttria-stabilized zirconia balls (Tosoh) in isopropyl alcohol and then heated at 1000 °C for 10 hours in air. After ball-milling for 8 hours, the powder was pressed into a pellet at 9.8 MPa. The pellet was then heated at 1300 °C for 10 hours in air. The procedure of ball-milling for 8 hours and heating at 1300 °C for 10 hours was repeated three times and only barium zirconate phase was confirmed by X-ray diffraction analysis (XRD, Rigaku Corporation, RINT2200, Cu-Kα) in the powder. The obtained powder was ball-milled for 100 hours. The powder was mixed with organic binder solution consisting of water (200 ml), polyvinyl alcohol (PVA) (2 g), glycerin (1 ml) and ethanol (10 ml). The ratio of the binder solution to the synthesized 15 % yttrium-doped

barium zirconate powder was 1 : 7 as a mass ratio. The powder was pressed into a pellet, whose diameter and thickness were about 10 and 1.5 mm, respectively, or a bar, whose height, width and thickness were about 5, 35 and 1 mm, respectively, at 392 MPa. Subsequently, the pellet and bar were heated at 600 °C for 8 hours to remove the binder solution and then sintered at 1600 °C for 24 hours. Barium oxide (BaO) has a significantly high vapor pressure at 1600°C (ca. 8×10^{-5} atm[95Bar]). There is a possibility for a part of BaO in the pellet and bar to vaporize during sintering at 1600 °C, which would cause deviation of the composition of the pellet and bar from the nominal composition. Therefore, the pellet and bar were embedded in sacrifice powders, which consists of 90 mass % of $BaZr_{0.85}Y_{0.15}O_{3-\delta}$ and 10 mass % of $BaCO_3$. The sacrifice powder and the pellet or bar were placed on an alumina boat. The sintering was conducted in a pure oxygen atmosphere, because the pellet and bar were pulverized when they were sintered in air.

2.3.2 Conductivity Measurement

Conductivity was measured by DC 4-terminal method and AC 2-terminal method. The sintered bar was used for DC 4-terminal measurement. Platinum wire was winded on the bar and silver paste (Fujikura Kasei) was painted on the platinum wire as electrodes. The data were collected using a potentiostat (Solartron SI 1287).

The sintered pellet and bar were used for AC 2-terminal measurement. Silver paste was painted on both surfaces of the pellet as electrodes after mechanically polishing the surface of the pellet. Electrodes for the bar were prepared in the same way for DC 4-terminal measurement. The data were collected using a frequency response analyzer (Solartron SI 1260) in the frequency range of 10 Hz to 7 MHz with applied voltage of 100 mV or 1 V. An equivalent circuit model was fitted to the data by using Zplot (Scribner Associates Inc., NC).

The data for DC 4-terminal method and AC 2-terminal method were collected in 20 ml min^{-1} argon gas with the water vapor pressure of 5.2×10^{-2} atm. The bar and pellet were held at 700 °C for more than 18 hours, in order to saturate water in the pellet quickly, and then cooled to 600 or 80 °C. After confirming that the data did not change for more than 5 hours at 600 or 80 °C, conductivity was measured. In case of measuring temperature dependence of conductivity, after confirming that the impedance spectra did not change for more than 3 hours at 600 °C, the pellets were cooled to 100 °C at a rate of 0.2 °C min^{-1} while measuring impedance at 50 minutes interval.

2.4 Results and Discussion

Figure 2.4 shows AC 2-terminal impedance spectrum of $BaZr_{0.85}Y_{0.15}O_{3-\delta}$ bars at 600 °C, and two arcs (Arc1 and Arc2) were observed. The impedance spectrum measured by AC 2-terminal method includes the impedance of electrolyte and electrodes. In order to determine the arcs due to the electrolyte, resistivity of the $BaZr_{0.85}Y_{0.15}O_{3-\delta}$ was measured by DC 4-terminal method by which resistivity of the electrodes can be eliminated. The time-dependant change of voltage between the two inner terminals was measured by DC 4-terminal measurement in the $BaZr_{0.85}Y_{0.15}O_{3-\delta}$ with applied DC current of 10 μA as shown in Fig. 2.5 (a) and (b), respectively. When the applied DC current was low (0.1 μA), the voltage was constant. On the other hand, when the applied DC current was high (10 μA), the voltage increased with time, which might be affected by polarization at the outer electrodes. Thus, the voltage of the $BaZr_{0.85}Y_{0.15}O_{3-\delta}$ was evaluated before the start of polarization, and the measurement was carried out while changing the applied DC current. The current-voltage characteristic of the $BaZr_{0.85}Y_{0.15}O_{3-\delta}$ at 600 °C is shown in Fig. 2.6. From Fig. 2.6, the resistivity of the $BaZr_{0.85}Y_{0.15}O_{3-\delta}$ at 600 °C was determined to be 110 Ω cm. Compared to

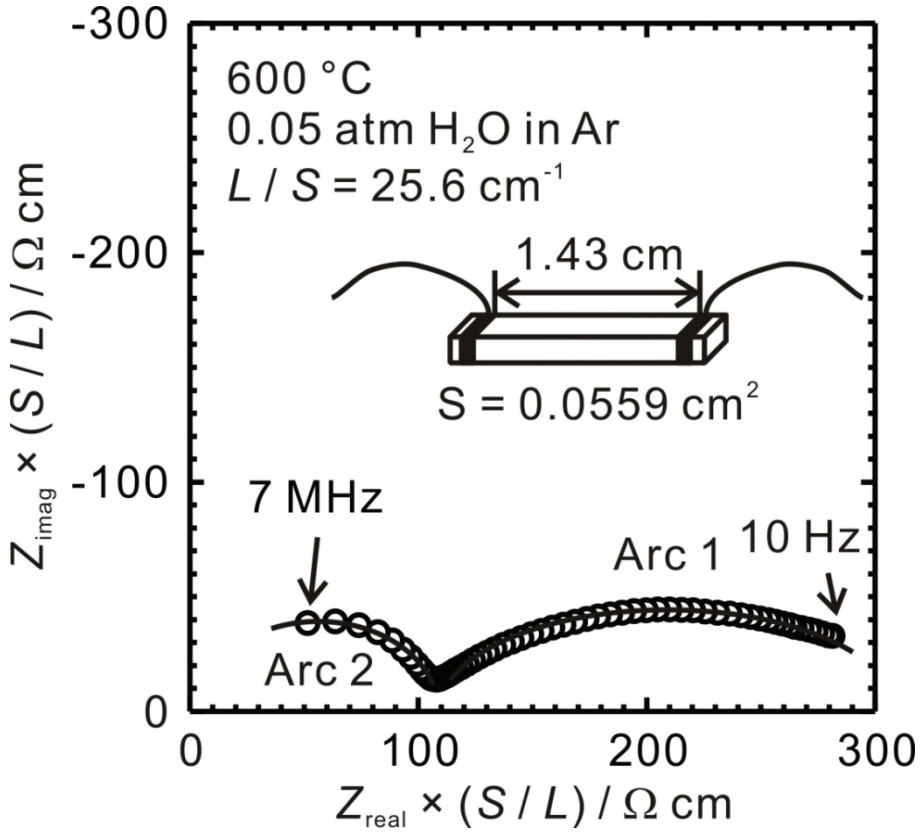

Figure 2.4 AC 2-terminal impedance spectrum at 600 °C in Ar-0.05 % H_2O using a bar of $BaZr_{0.85}Y_{0.15}O_{3-\delta}$.

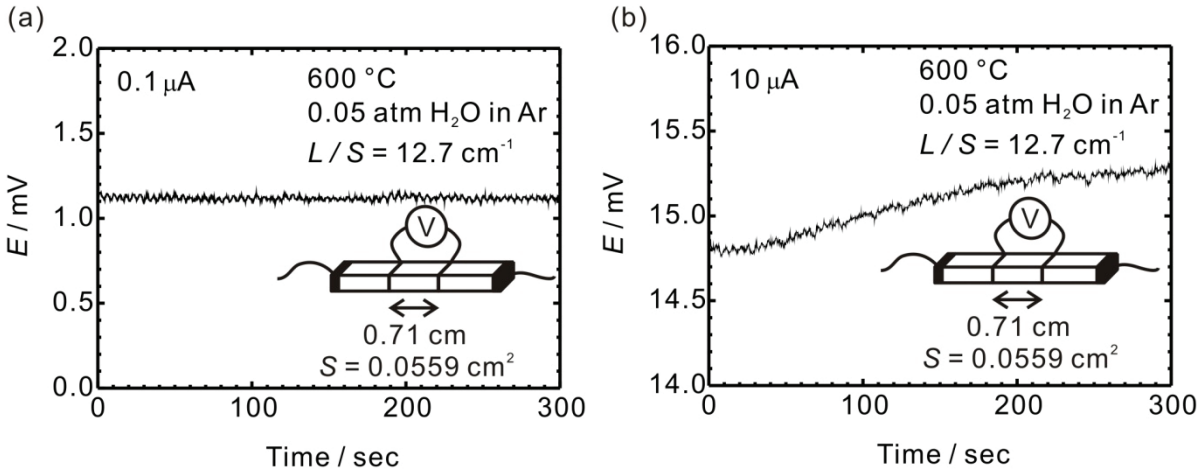

Figure 2.5 Time-dependant change of voltage between two inner terminals of $BaZr_{0.85}Y_{0.15}O_{3-\delta}$ bars. DC current of of (a) 0.1 and (b) 10 μA was applied in DC 4-terminal measurement at 600 °C in Ar-0.05 % H_2O.

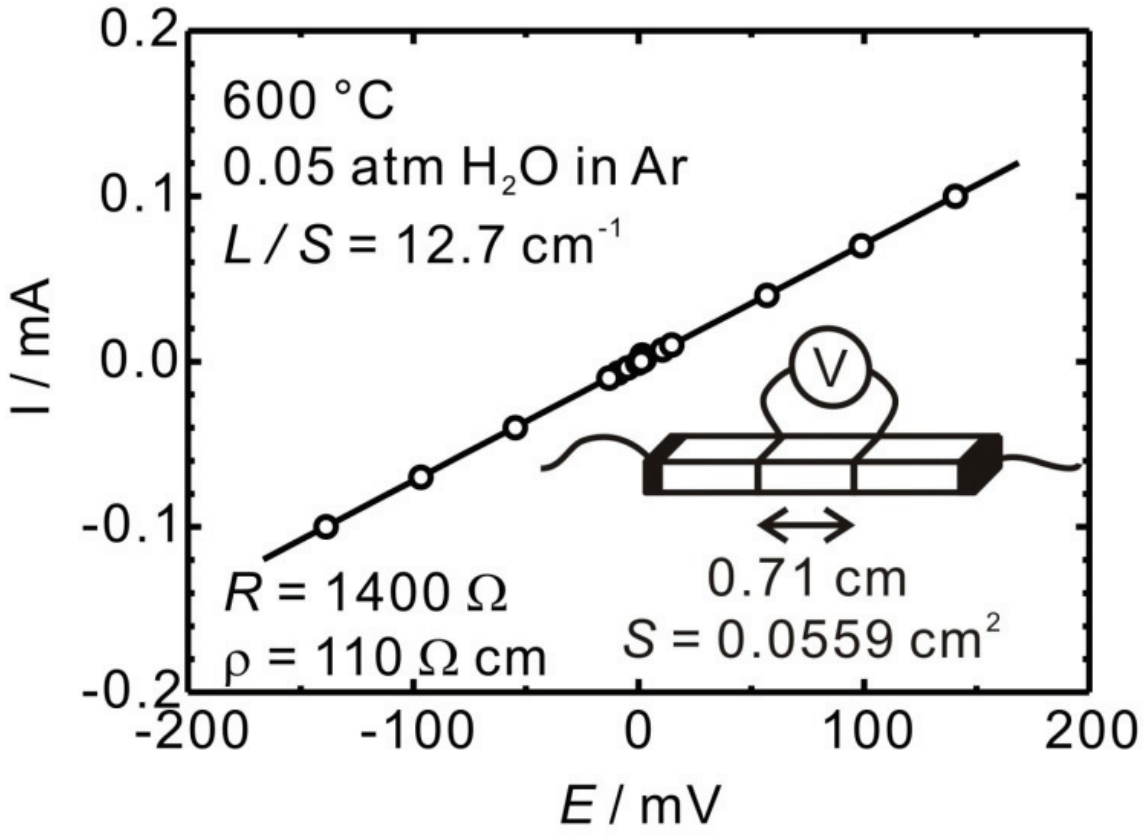

Figure 2.6 Current-voltage characteristic of $BaZr_{0.85}Y_{0.15}O_{3-\delta}$ bars in DC 4-terminal measurement at 600 °C in Ar-0.05 % H_2O.

Fig. 2.4, the resistivity of the $BaZr_{0.85}Y_{0.15}O_{3-\delta}$ measured by DC 4-terminal method, 110 Ω cm, corresponds to the value of the right edge of Arc 2. Therefore, we can say that Arc 1 comes from electrode and that Arc 2 comes from electrolyte.

Another experiment was conducted to determine the arc due to the electrolyte in AC 2-terminal measurement. From Eq. (2-11) and (2-12), resistance is proportional to length and inversely proportional to the cross-sectional area of the sample. Thus, we changed the length of the bar while keeping the cross-sectional area of bars constant. In this case, the resistance of the $BaZr_{0.85}Y_{0.15}O_{3-\delta}$ should be changed, while the resistance of electrodes should be constant. Fig. 2.7 (a) and (b) show impedance spectra of the $BaZr_{0.85}Y_{0.15}O_{3-\delta}$ at 600 °C measured by changing the distance between electrodes. As seen in Fig. 2.7 (a) and (b), Arc 1 did not change so much, while Arc 2 was changed. Also, the value of the right edge of Arc 2

was proportional to the distance between electrodes, and resistivities in both measurements are the same value. Thus, we conclude that Arc 1 is due to electrode and that Arc 2 is due to electrolyte.

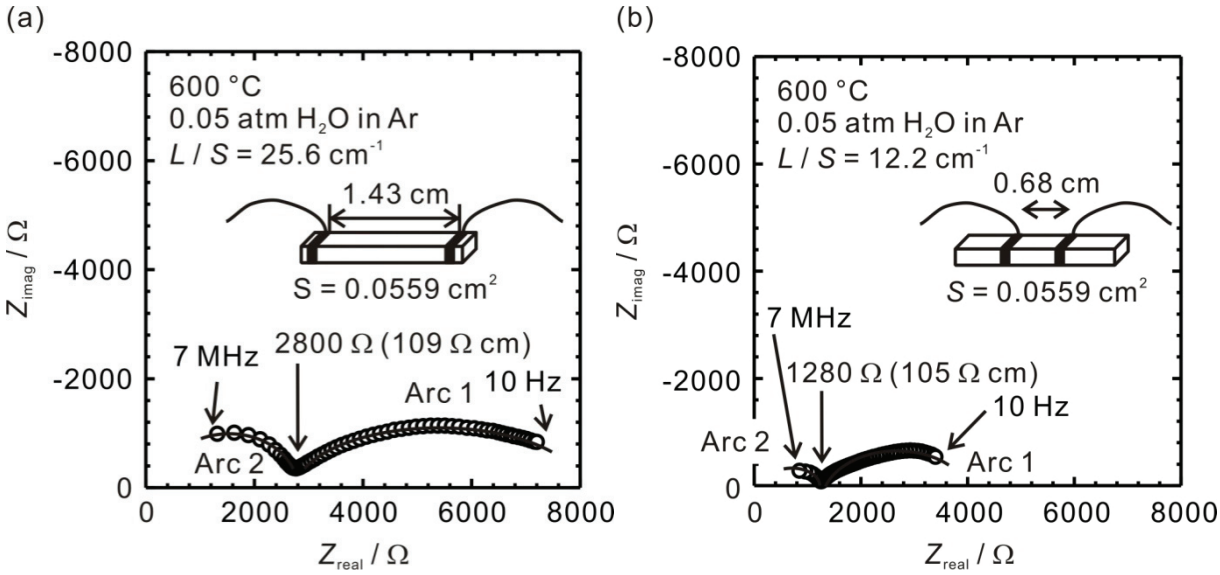

Figure 2.7 Change of AC 2-termonal impedance spectra with the length of bar at 600 °C in Ar-0.05 % H_2O using a bar of $BaZr_{0.85}Y_{0.15}O_{3-\delta}$. The length of a bar is (a) 1.43 and (b) 0.68 cm.

There should be two arcs of electrolyte; one from bulk and one from grain-boundary. However, only one arc was observed in Fig 2.7. We concluded that another arc should exist at a higher frequency region of Arc 2 and tried to detect the arc at the left side of Arc 2. But it was not clear as seen in Fig. 2.8. The reason for the unclear arc is considered to be that the capacitance of the arc at the left side of Arc 2 was too small (less than 10^{-13} F) to determine the resistance and capacitance accurately with the frequency response analyzer we used. Therefore, we changed $\frac{L}{S}$ of sample to increase the capacitance by the use of a pellet. Figure 2.9 shows the impedance spectrum of the $BaZr_{0.85}Y_{0.15}O_{3-\delta}$ in pellet form at 80 °C. In the figure, a new arc (Arc3) was observed clearly at the left side of Arc 2. To decide which arcs come from bulk and grain-boundary, the dielectric constants of boundary, the dielectric

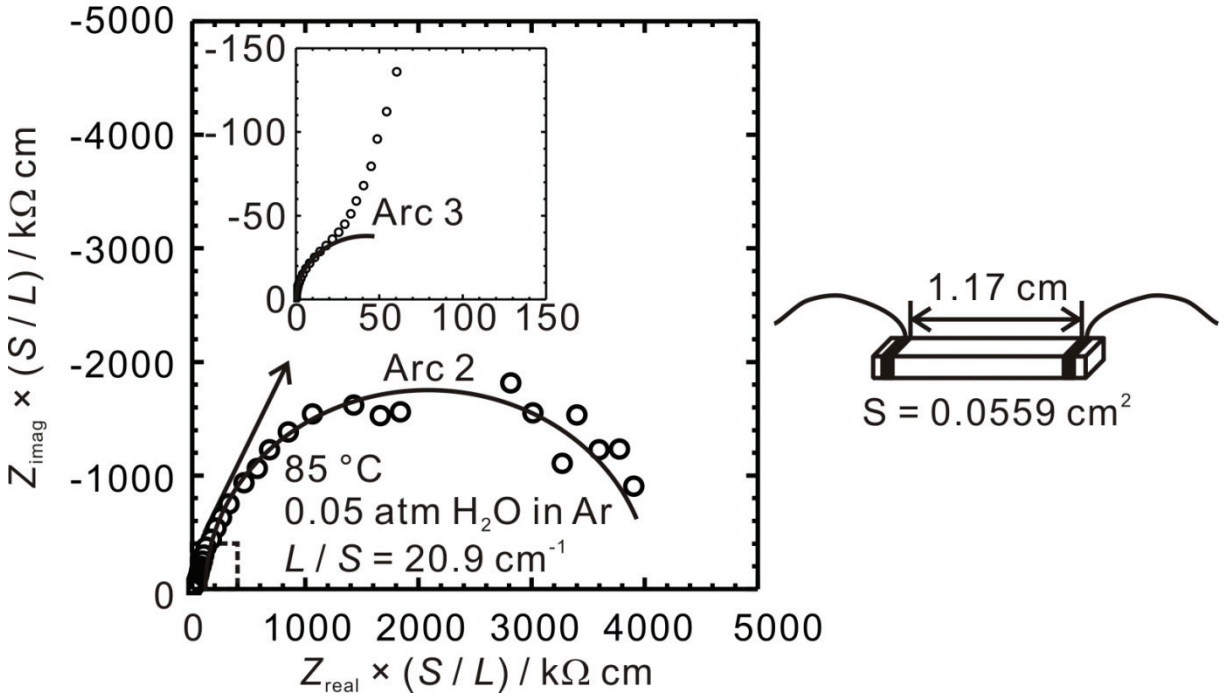

Figure 2.8 AC 2-terminal impedance spectrum at 85 °C in Ar-0.05 % H_2O using a bar of $BaZr_{0.85}Y_{0.15}O_{3-\delta}$.

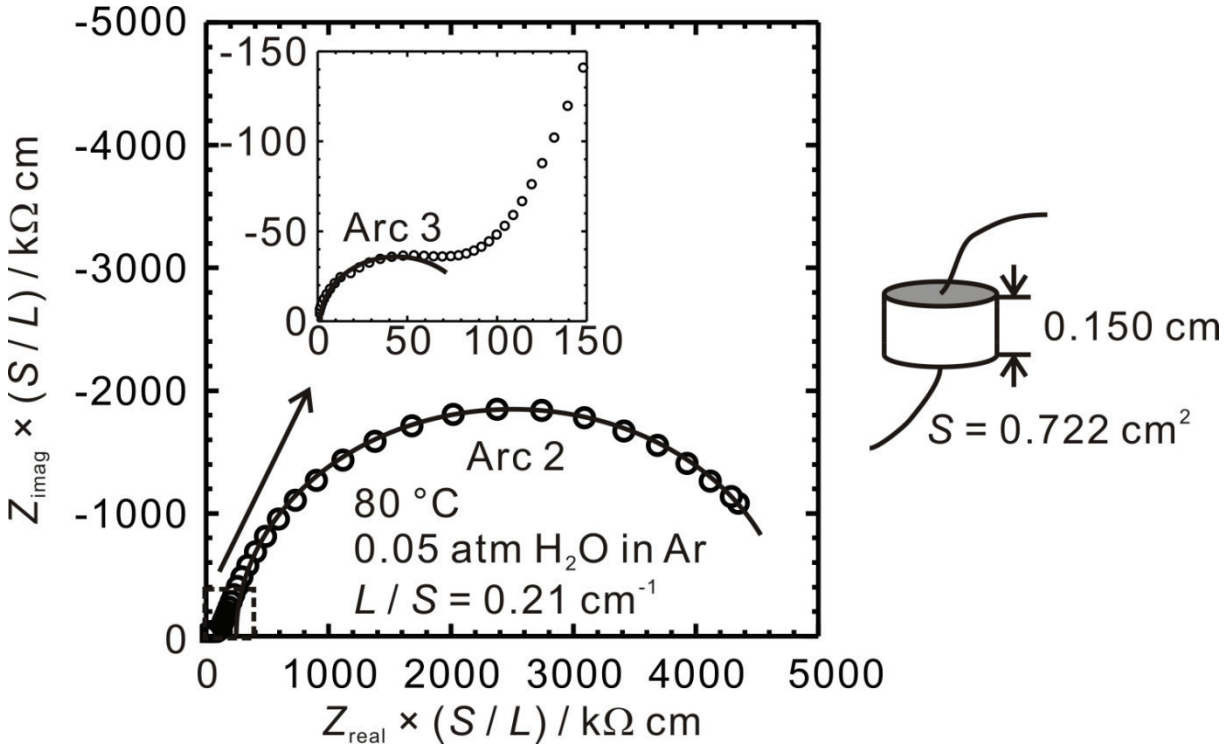

Figure 2.9 AC 2-terminal impedance spectrum at 80 °C in Ar-0.05 % H_2O using a pellet of $BaZr_{0.85}Y_{0.15}O_{3-\delta}$.

constants of Arc 2 and 3 were calculated from

$$C = \frac{S}{L} \epsilon \epsilon_0 \quad (2\text{-}17)$$

The calculated dielectric constants of Arc 2 and 3 were 7100 and 60, respectively. T he dielectric constant of bulk for gadolinium-doped barium cerate, which shows proton conduction and have perovskite structure, is reported as 40 to 50.[98Hai] Also, dielectric constants of bulk and grain-boundary for 20% yttrium-doped barium zirconate are reported as 46 and 6500, respectively.[07Bab] From these reports, we conclude that Arc 2 comes from grain-boundary and Arc 3 comes from bulk.

Next, we investigated the dependence of oxygen partial pressure (p_{O2}) on total conductivity of $BaZr_{0.85}Y_{0.15}O_{3-\delta}$ at 600 °C in order to determine the predominant mobile species. The total conductivity was calculated from length of sample, cross sectional area of sample and total resistance which was a high intercept of Arc 2. As discussed in Chapter 1, proton, oxide ion, hole and electron are candidates as mobile species in doped barium zirconates. The dependence of oxygen partial pressure on total conductivity of $BaZr_{0.85}Y_{0.15}O_{3-\delta}$ was investigated at 600 °C under wet conditions using AC 2-terminal measurement. The results are shown in Fig. 2.10 and Table 2.1. The various oxygen partial pressures were realized by changing the atmosphere as shown in Table 2.1. At low oxygen partial pressures ($p_{O2} < 3 \times 10^{-5}$ atm), the total conductivity was independent on oxygen partial pressure, which suggests that ion is predominant mobile species at these oxygen partial pressures. In contrast, at high oxygen partial pressures ($p_{O2} > 10^{-2}$ atm), the total conductivity increased with the increase of oxygen partial pressures. From the behavior of total conductivity, holes were the predominant mobile species at higher oxygen partial pressures considering Eq. (1-5). We could not find a region where electrons were the predominant mobile species in the examined range of partial pressure because we could not observe the phenomenon in which total conductivity increased with the decrease of oxygen partial

pressures. Additionally, the activation energy of 15% yttrium-doped barium zirconate is 0.45 eV for bulk conductivity, which was calculated from the conductivity measurement in argon gas with the water vapor pressure of 5.2×10^{-2} atm as shown in Fig. 2.10. This activation energy is almost the same magnitude as in high-temperature proton conductors[98Sch] and much lower than that for oxide ion conduction of yttrium-doped barium zirconate (1.1 eV). [00Boh] From these results, proton conduction is predominant in argon gas with the water vapor pressure of 5.2×10^{-2} atm at 600 °C ($p_{O2} = 3 \times 10^{-5}$).

Table 2.1 Dependence of oxygen partial pressure on total conductivity of $BaZr_{0.85}Y_{0.15}O_{3-\delta}$ at 600 °C in 0.05 % H_2O.

p_{O2} (atm)	Atmosphere	Total resistance (Ω)	Total conductivity / Scm^{-1}
4.6×10^{-25}	100% H_2	1990	8.68×10^{-3}
1.8×10^{-24}	50% H_2 – 50% Ar	1990	8.68×10^{-3}
4.6×10^{-23}	10% H_2 – 90% Ar	1990	8.70×10^{-3}
1.8×10^{-22}	5% H_2 – 95% Ar	1990	8.67×10^{-3}
3.2×10^{-5}	100% Ar	1910	9.05×10^{-3}
9.5×10^{-2}	10% O_2 – 90% Ar	1660	1.04×10^{-2}
9.5×10^{-1}	100% O_2	1480	1.17×10^{-2}

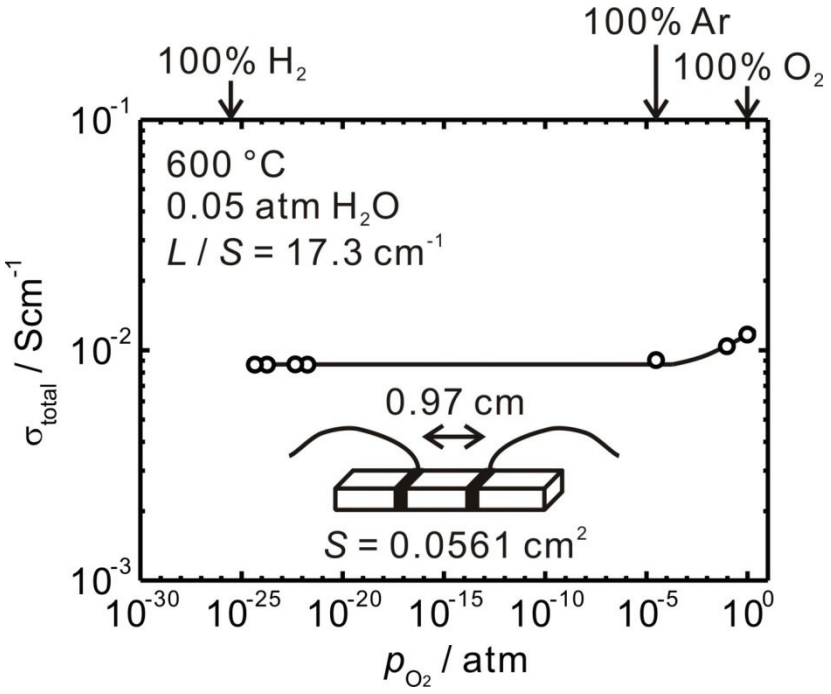

Figure 2.10 Dependence of oxygen partial pressure on total conductivity of $BaZr_{0.85}Y_{0.15}O_{3-\delta}$ at 600 °C in 0.05 % H_2O.

We also varied the concentration of yttrium in barium zirconate, and the results of conductivity measurement using pellets are shown in Fig. 2.10. Bulk conductivity and the inverse of grain-boundary resistances of yttrium-doped barium zirconate increased with increasing mole fraction of yttrium. 20 % yttrium-doped barium zirconate showed the highest conductivity. However, 20 % yttrium-doped barium zirconate has poor reproducibility in conductivity. Thus, we investigated 15 % yttrium-doped barium zirconate in this study.

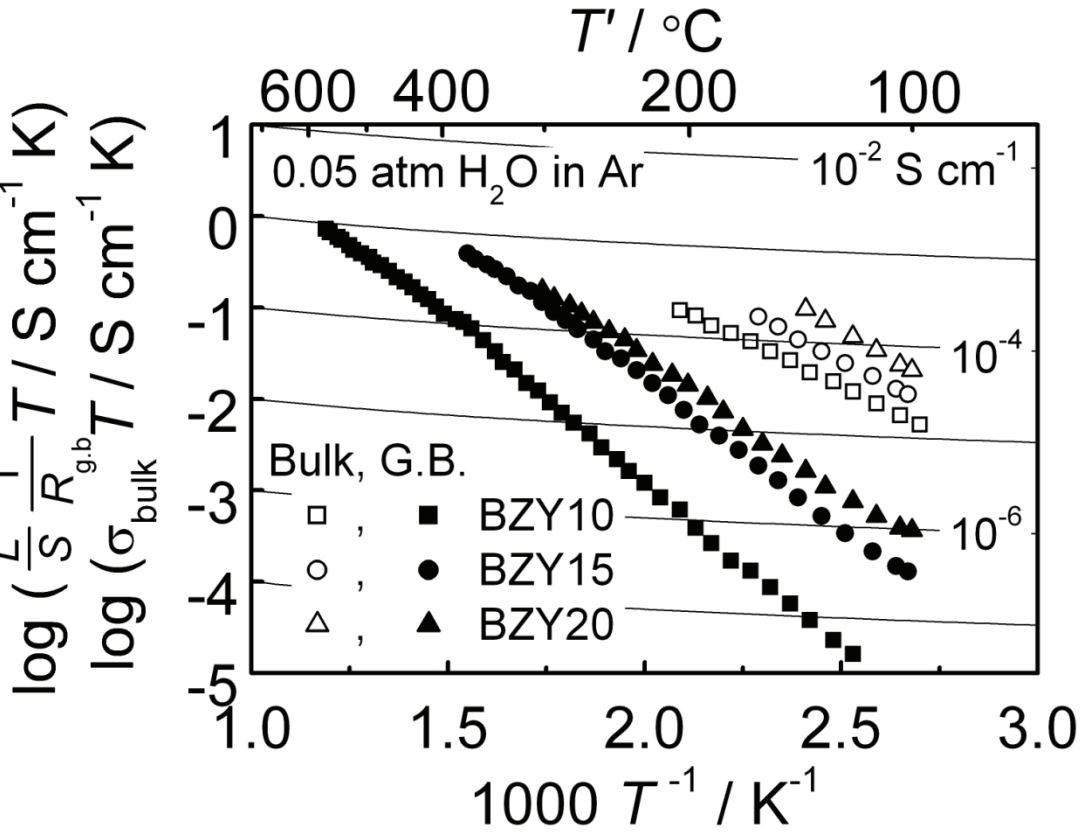

Figure 2.11 Bulk conductivities, σ_{bulk}, and inverse of grain-boundary resistances, $\frac{L}{S}\frac{1}{R_{g.b.}}$, of yttrium-doped barium zirconates in Ar-0.05 % H_2O as a function of temperature.

2.5 Conclusions

We identified three arcs, which are obtained by AC 2-terminal measurement of 15 % yttrium-doped barium zirconate, by combining results of DC 4-terminal measurement with changing a shape of samples. An arc which appears at the highest frequency region is due to

bulk and an arc due to grain-boundary appears next to the arc due to bulk. An arc due to electrode appears at the lowest frequency region. Also, it is found that grain-boundary resistance is higher than bulk resistance and total resistance is governed by grain-boundary resistance.

We also examined the dependence of oxygen partial pressure on total conductivity of $BaZr_{0.85}Y_{0.15}O_{3-\delta}$ at 600 °C under wet atmosphere. In the region of $p_{O2} < 3 \times 10^{-5}$ atm, proton conduction was dominant. When $p_{O2} > 10^{-2}$ atm, hole conduction appeared in addition to proton conduction.

References

[95Bar] I. Barin, *Thermochemical Data of Pure Substances,* 3rd ed., VCH Verlagsgesellschaft mbH, Weinheim (1995).

[98Hai] S.M. Haile, D. L. West and J. Campbell, *Journal of Materials Research*, **13** [6], 1576-1595 (1998).

[98Sch] T. Schober, *Solid State Ionics*, **109**. 1-11 (1998).

[00Boh] H. G. Bohn and T. Schober, *Journal of the American Ceramic Society*, **83,** 768-772 (2000).

[05Bab] P. Babilo and S. M. Haile, *Journal of the American Ceramic Society,* **88** [9]**,** 2362-2368 (2005).

[07Bab] P. Babilo, T. Uda and S. M. Haile, *Journal of Materials Research*, **22,** 1322-1330 (2007).

Chapter 3

Dependence of Dopant Cations on Microstructure and Proton Conductivity of Barium Zirconate

3.1 Introduction

As described in Chapter 1, yttrium-doped barium zirconate is known to have the highest bulk conductivity among the trivalent cation doped barium zirconates so far, and many researchers are working on Y-doped barium zirconate. However, reports on other trivalent cation doped barium zirconates are relatively limited.[93Man,95Sla,01Kre,02Lai,06Ahm1,07Ahm,08Ito] In this chapter, we explored a dopant which might have higher proton conductivity than yttrium. Then, we attempted to establish a general trend of dopant behavior in barium zirconate for microstructure and proton conductivity by examining and characterizing eleven dopant cations (Mg^{2+}, Sc^{3+}, In^{3+}, Yb^{3+}, Tm^{3+}, Er^{3+}, Y^{3+}, Ho^{3+}, Gd^{3+}, Nd^{3+}, La^{3+}, Bi^{3+} and Ga^{3+}).

3.2 Experimental

We made pellets having various compositions and dopants. When the dopant cation was magnesium (Mg), the mole fractions of magnesium were 0, 0.025, 0.50, 0.10 (X_{MgO} = 0, 0.025, 0.50, 0.10) at X_{BaO} = 0.50 ($BaZr_{1-x}Mg_xO_{3-\delta}$ (x=0, 0.05, 0.10, 0.20)) When the dopant cations were trivalent cations (M^{3+}) (M = Sc, In, Yb, Tm, Er, Y, Ho, Gd, Nd, La, Bi and Ga), the mole fraction of trivalent cation was 0.075 ($X_{MO1.5}$ = 0.075) at X_{BaO} = 0.50 ($BaZr_{0.85}M_{0.15}O_{3-\delta}$). Crystalline powders of various cation doped barium zirconates were synthesized by conventional solid state reaction and the detail is described in Chapter 2. The purity and source of raw materials are tabulated in Table 3.1. In the process of synthesis, if second phases were detected by XRD after third heating at 1300 °C, we considered that the second phases were equilibrium phase at 1300 °C, and proceeded to the next process without

Table 3.1 Purity and source of raw materials.

Raw material	Chemical formula	Purity (mass %)	Source
Barium carbonate	$BaCO_3$	99.9	Wako
Zirconium oxide*	ZrO_2	99.97 (including 2% of hafnium oxide)	Daiichi Kigenso
Magnesium oxide	MgO	99.9	Wako
Indium oxide	In_2O_3	99.9	Nacalai tesque
Ytterbium oxide	Yb_2O_3	99.9	Wako
Holmium oxide	Ho_2O_3	99.9	Wako
Gadolinium Oxide	Gd_2O_3	99.9	Wako
Neodymium oxide	Nd_2O_3	99.9	Nacalai tesque
Lanthanum oxide	La_2O_3	99.9	Wako
Bismuth oxide	Bi_2O_3	99.9	Furuuchi Chemical
Gallium oxide	Ga_2O_3	99.99	Wako
Scandium oxide	Sc_2O_3	99.99	Daiichi Kigenso
Yttrium oxide	Y_2O_3	99.9	Shin-Etsu Chemical
Erbium oxide	Em_2O_3	99.9	Wako
Thulium oxide	Tm_2O_3	99.9	Wako

* Scandium, yttrium, erbium and thulium doped barium zirconate were synthesized using a zirconia from a different supplier (99.97 % including 2% of hafnia (HfO_2), Tohso); the difference of zirconia was in grain size; 480 nm from Daiichi kigenso and 24 nm from Tosoh.

further heating at 1300 °C. During sintering, the sacrifice powders for Gd and Ga doped barium zirconates consists of 99 mass % of synthesized barium zirconate and 1 mass % of barium carbonate. The sacrifice powders for other cation doped barium zirconates consists of 90 mass % of synthesized doped barium zirconate and 10 mass % of barium carbonate.

Microstructures of the sintered pellets were observed by a scanning electron microscope (SEM, Keyence Corporation, VE-7800), and composition analysis of the sintered pellets was measured by an energy dispersive X-ray microanalyzer (EDX) (JEOL, JED-2300) equipped with a field emission-scanning electron microscope (FE-SEM) (JEOL, JSM-6500F) or by EDX (EDAX, Genesis-XM2) equipped with SEM (Keyence Corporation, VE-7800). The lattice parameters of the sintered pellets were determined by X-ray diffraction analysis (XRD, Rigaku Corporation, RINT2200, Cu-Kα). The density of the sintered pellets was measured by the Archimedes method in ionic liquid (trimethyl-*n*-hexylammonium bis((trifluoromethyl)sulfonyl) amide (TMHA-Tf_2N)).

Conductivity of the sintered pellets was measured by AC 2-terminal method as described in Chapter 2. The pellet was held at 700 °C for more than 18 hours, in order to saturate water in the pellet quickly, and then cooled to 500 °C. After confirming that the impedance spectra did not change for more than 3 hours at 500 °C, the pellets were cooled to 100 °C at a rate of 0.2 °C min^{-1} while measuring impedance at 50 minutes interval.

3.3 Results and Discussion

3.3.1 Solubility of Magnesium into B site of Barium Zirconate

The ionic radius of magnesium ion for six-fold coordination is 0.0720 nm[76Sha] and the ionic radius is the same as that of zirconium ion (0.0720 nm[76Sha]). Thus, we selected magnesium as a candidate for dopant in barium zirconate. XRD patterns of the sintered pellets were shown in Fig. 3.1. When the mole fraction of magnesium was 0 ($X_{MgO} = 0$), only the barium zirconate phase was detected. At $X_{MgO} = 0.025$, 0.05, and 0.10, barium zirconate phase and $BaAl_2O_4$ phase were identified.

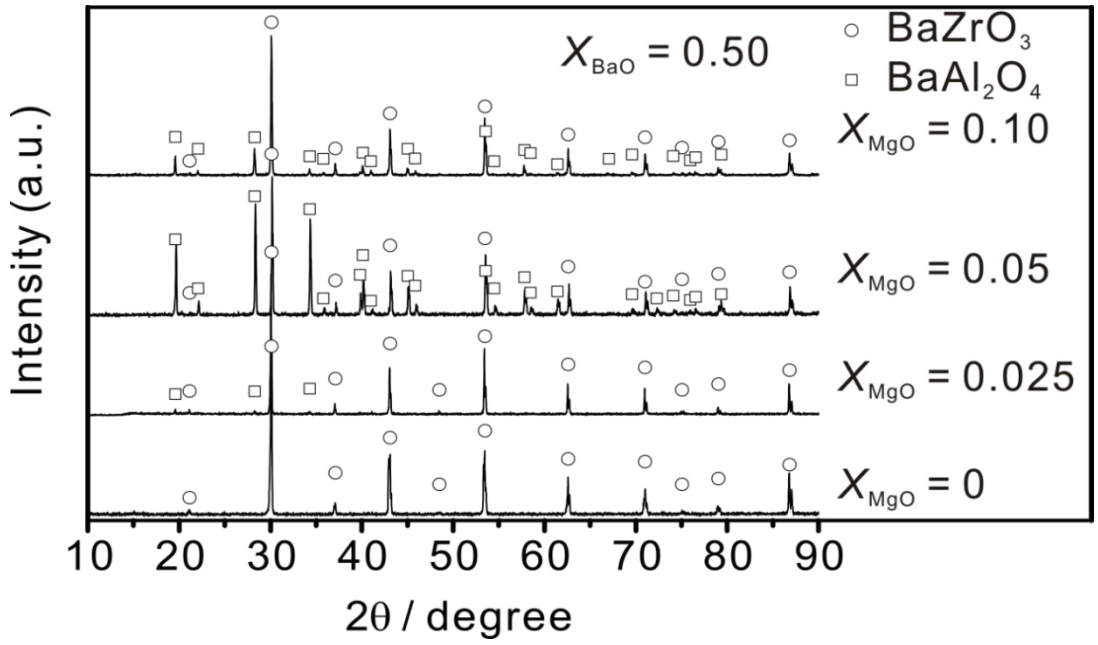

Figure 3.1 XRD patterns of pellets of X_{MgO} = 0, 0.025, 0.05 and 0.10 at X_{BaO} = 0.50 after heat-treatment at 1600 °C for 24 hours. Each symbol indicates diffraction patterns of ○ ($BaZrO_3$, JCPDS No. 00-006-0399) and □ ($BaAl_2O_4$, JCPDS No. 00-017-0306).

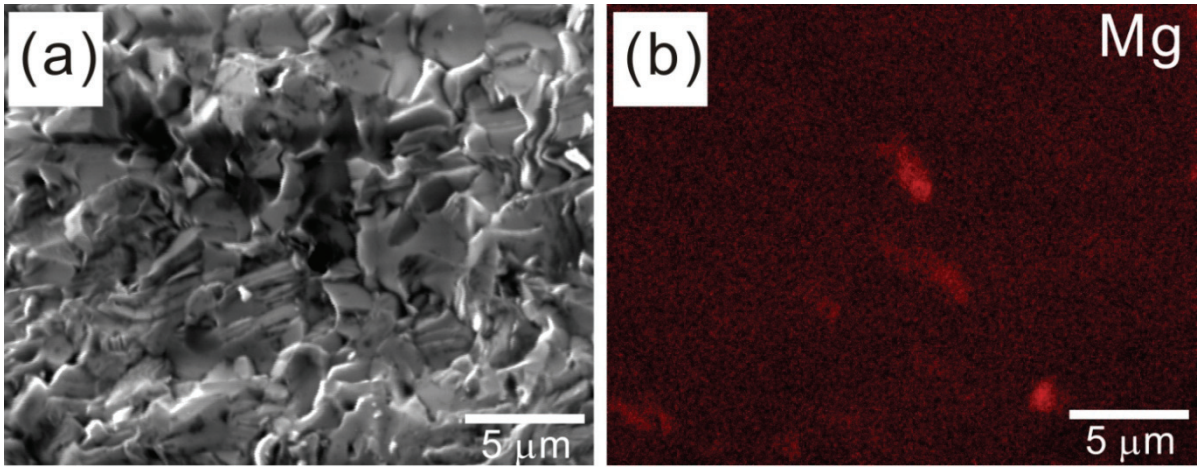

Figure 3.2 (a) SEM image and (b) element distribution map of Mg in a pellet of X_{MgO} = 0.025 at X_{BaO} = 0.50 after heat- treatment at 1600 °C for 24 hours.

Figure 3.2 shows an SEM image and element distribution map of the area in the pellet of X_{MgO} = 0.025 at X_{BaO} = 0.50. From the figures, we can see that there is a magnesium-concentrated area. According to EDX analysis, the magnesium-concentrated area consists of only magnesium and oxygen, which means that magnesium oxide (MgO) precipitates. We consider that because of the small atomic scattering factors of Mg and O compared to those of Ba and Zr, magnesium oxide was not detected by XRD. Thus, the solubility of magnesium into B site (zirconium site) of barium zirconate should be less than X_{MgO} = 0.025. The ionic radius of magnesium for six-fold coordination (0.0720 nm) is almost the same as that of scandium (Sc) (0.0745 nm[76Sha]), but the solubility of magnesium into B site in barium zirconate was much smaller than that of scandium ($X_{ScO1.5}$ = 0.29 which is described in Chapter 5). This is due to the fact that doping divalent magnesium requires twice as many oxygen vacancies as doping trivalent scandium from the view point of the electroneutrality condition and causes larger energetic instability. This suggests, in addition to ionic radius, that the valence state of the dopant cation is quite important for the solubility into B site in barium zirconate. When magnesium does not dissolve into barium zirconate, barium oxide becomes

extra. It is considered that this extra barium oxide reacted with alumina boat and formed $BaAl_2O_4$.

The existence of MgO phase even at $X_{MgO} = 0.025$ also implies that magnesium does not dissolves into A site (barium site) of barium zirconate and there is no reaction between magnesium oxide and barium zirconate. Thus, we propose that magnesium oxide is a more suitable material than alumina conventionally used as a boat or crucible for processing barium zirconate.

3.3.2 Solubility of Trivalent Cations (M^{3+}) (M= Sc, In, Yb, Tm, Er, Y, Ho, Gd, Nd, La, Bi and Ga) into B site of Barium Zirconate

We investigated, by XRD and EDX analysis, whether trivalent cations (Sc^{3+}, In^{3+}, Yb^{3+}, Tm^{3+}, Er^{3+}, Y^{3+}, Ho^{3+}, Gd^{3+}, Nd^{3+}, La^{3+}, Bi^{3+} and Ga^{3+}) can dissolve into barium zirconate when the mole fraction of the trivalent cation is 0.075 ($X_{MO1.5} = 0.075$) at $X_{BaO} = 0.50$.

Figure 3.3 (a) and (b) show XRD patterns of pellets after sintering at 1600 °C for 24 hours. In the case of scandium (Sc), indium (In), ytterbium (Yb), thulium (Tm), erbium (Er), yttrium (Y), holmium (Ho), gadolinium (Gd) and neodymium (Nd), only barium zirconate phase was detected. Diffraction peaks of second phases were identified in the case of lanthanum (La), bismuth (Bi) and gallium (Ga). Thus, the solubility of La, Bi and Ga into B site of barium zirconate is less than $X_{MO1.5} = 0.075$. Three studies have attempted to use Ga as a dopant.[93Iwa,04Oma,06Ahm2] Omata *et al.* reported that second phases were identified in the sample of $X_{GaO1.5} = 0.025$ after sintering at 1550 °C.[04Oma] Ahmed *et al.* reported that the sample of $X_{GaO1.5} = 0.050$ after sintering at 1500 °C was single phase.[06Ahm2] Iwahara *et al.* reported that the sample of $X_{GaO1.5} = 0.025$ after sintering at temperatures from 1500 to 1650 °C was single phase.[93Iwa] In our experiment, at $X_{GaO1.5} = 0.075$, the small amount of second

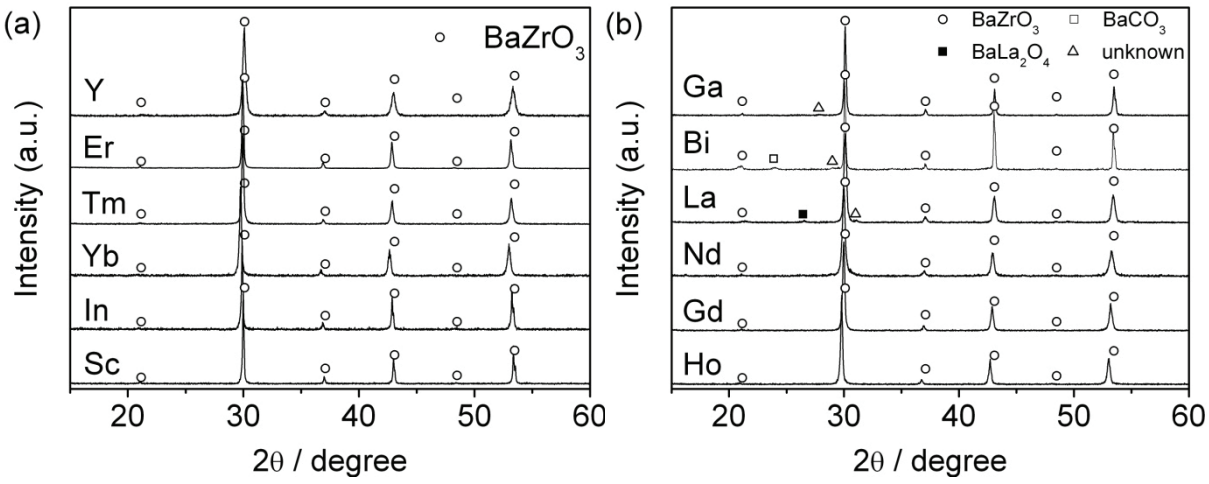

Figure 3.3 XRD patterns of pellets of $X_{MO1.5}$ = 0.075 at X_{BaO} = 0.50 after heat- treatment at 1600 °C for 24 hours ((a) M = Sc, In, Yb, Tm, Er, Y (b) M = Ho, Gd, Nd, La, Bi, Ga). Each symbol indicates diffraction patterns of ○ ($BaZrO_3$, JCPDS No. 00-006-0399), □ ($BaCO_3$, JCPDS No. 00-005-0378), ■ ($BaLa_2O_4$, JCPDS No. 00-042-1500) and ∆ (unknown peak).

phase in Ga-doped barium zirconate was detected. Therefore, the solubility of gallium into barium zirconate might be between $X_{GaO1.5}$ = 0.050 and 0.075 at 1600 °C.

The compositions of Sc, In, Yb, Y, Ho, Gd and Nd doped pellets were measured by EDX analysis and the results are shown on pseudoternary phase diagrams of BaO-ZrO_2-$MO_{1.5}$ system in Fig. 3.4. In the case of Sc, In and Gd, all the analyzed points were near the nominal composition, although there was some deviation to the BaO rich region which might have been caused by BaO-rich sacrifice powder. Thus, we regarded that Sc-doped, In-doped and Gd-doped barium zirconate have a single phase at 1600 °C. In the case of Yb, Y and Ho, the analyzed compositions varied from dopant poor composition to dopant rich composition with keeping the composition line of about X_{BaO} = 0.50. As described in Chapter 4 and 6, 15% Y-doped barium zirconate shows two phase separation into two pervskites or similar structures at the synthesizing temperature of 1300 °C. The trace of phase separation at 1300 °C has often been observed even after sintering at 1600 °C, although the equilibrium phase of 15% Y-doped barium zirconate at 1600 °C is single perovskite. The behaviors of Yb and Ho are also

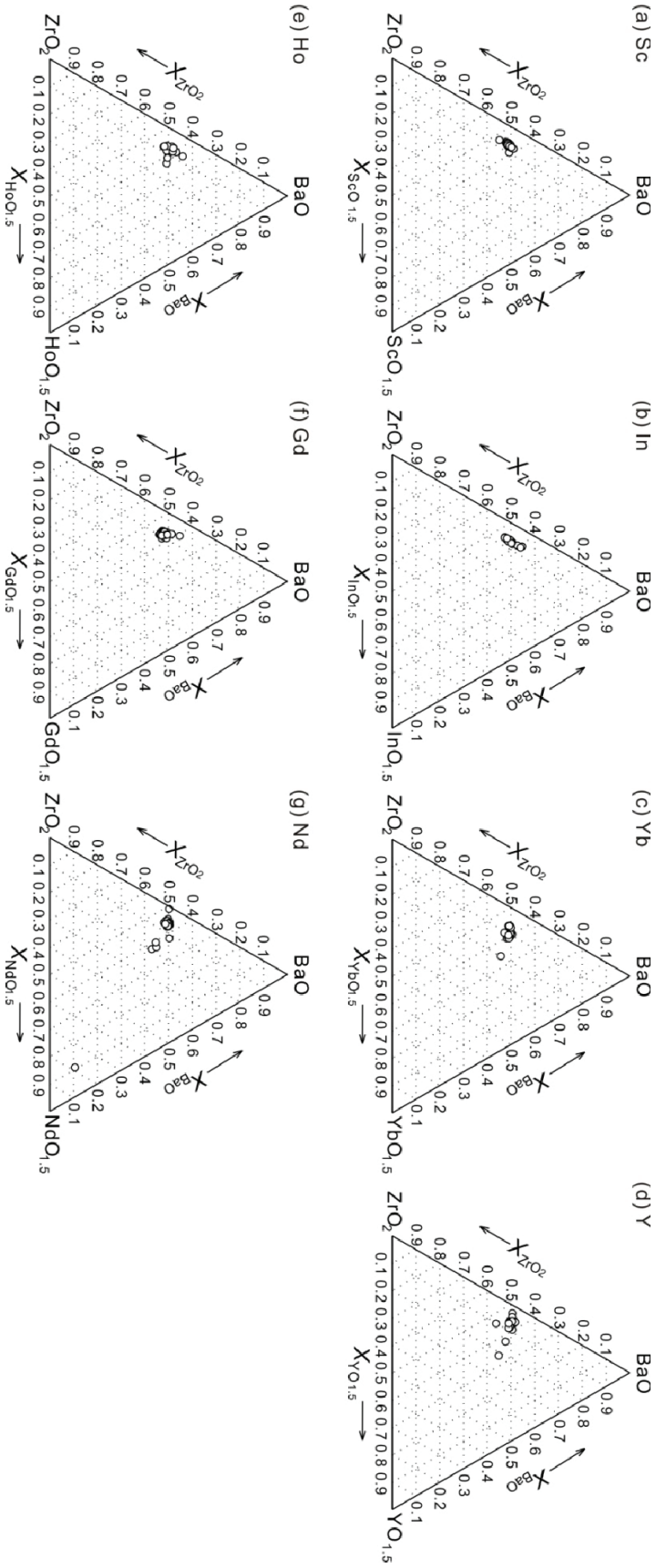

Figure 3.4 Results of EDX analysis on pseudoternary phase diagrams of $BaO\text{-}ZrO_2\text{-}MO_{1.5}$ system (M = (a) Sc, (b) In, (c) Yb, (d) Y, (e) Ho, (f) Gd and (g) Nd).

Table 3.2 Quantitative character of dopant cations for barium zirconate.

Dopant	Ionic radius (nm)	Solubility		Microstructure	Proton conductivity (Bulk)
		1600 °C	1300 °C		
Ga	0.0620	$< X_{GaO1.5} = 0.075$	–	–	–
Sc	0.0745	$> X_{ScO1.5} = 0.075$	–	Well grown	Bad
In	0.0800	$> X_{InO1.5} = 0.075$	–	Well grown	Bad
Yb	0.0868	$> X_{YbO1.5} = 0.075$	Phase separation	Bimodal	Good
Tm	0.0880	$> X_{TmO1.5} = 0.075$*	–*	Bimodal	Good
Er	0.0890	$> X_{ErO1.5} = 0.075$*	–*	Bimodal	Good
Y	0.0900	$> X_{HoO1.5} = 0.075$	Phase separation	Bimodal	Good
Ho	0.0901	$> X_{YO1.5} = 0.075$	Phase separation	Bimodal	Good
Gd	0.0938	$> X_{GdO1.5} = 0.075$	–	Well grown	Bad
Nd	0.0983	$< X_{NdO1.5} = 0.075$	–	–	–
Bi	0.1030	$< X_{BiO1.5} = 0.075$	–	–	–
La	0.1032	$< X_{LaO1.5} = 0.075$	–	–	–

*In the case of Tm and Er, the solubility was confirmed only by XRD.

similar in the points of sintered microstructure and proton conductivity described in later. Thus, we classified Yb and Ho as "Y-type" dopant. In the case of Nd, grains with close composition to Nd_2O_3 were observed in EDX analysis. Therefore, the solubility of Nd into B site of barium zirconate is judged to be less than $X_{NdO1.5} = 0.075$.

The solubility into B site of barium zirconate at $X_{MO1.5} = 0.075$ is summarized in Table 3.2 with ionic radius of the trivalent cations, summary of sintered microstructure and proton conductivity, which are explained later. One can see from the table that ionic radius has a large influence on the solubility into B site of barium zirconate. The ionic radii of Sc, In, Yb, Tm, Er, Y, Ho and Gd are relatively close to that of zirconium ion (Zr^{4+}: 0.072 nm[76Sha]), and the solubility of these cations into B site of barium zirconate is more than $X_{MO1.5} = 0.075$. In contrast, the ionic radii of Nd, La and Bi are much larger than that of zirconium ion, and the solubility of these cations into B site of barium zirconate is less than $X_{MO1.5} = 0.075$. In the case of Nd, La and Bi, there is a possibility that these cations were partially substituted for A site as reported for barium cerate, where the amount of trivalent cation substituted for A site increases as the ionic radius of the trivalent cation becomes larger than that of cerium

ion.[04Wu] We confirmed a large trace of liquid phase in self-sacrificed powders after sintering of Nd, La and Bi doped barium zirconate because the self-sacrificed powders were strongly hardened and extremely large needle-like grains (~10 μm) were observed in the self-sacrificed powders by SEM as shown in Fig. 3.5. This phenomenon might be reasonable if some or a large amount of dopant cation is assumed to be substituted for A site and barium oxide becomes extra.

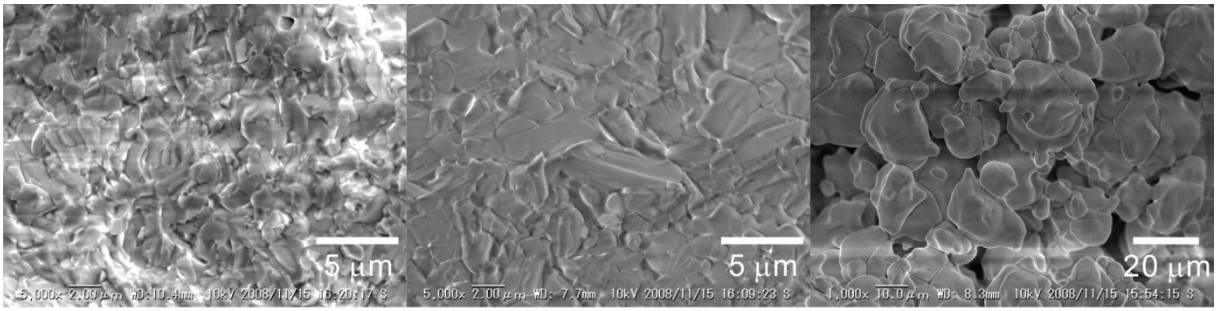

Figure 3.5 SEM images of sacrifice powders for Nd, La and Bi doped barium zirconate.

We can also say that it is difficult to keep the structure of barium zirconate when a trivalent cation smaller than zirconium ion is doped, as in the case of Ga (Ga^{3+}: 0.0620 nm[76Sha]). The solubility of Ga into B site of barium zirconate is also less than $X_{GaO1.5} = 0.075$.

On the base of a hard sphere model, the lattice parameter should increase with increasing dopant size when the dopant dissolves into B site of barium zirconate. Lattice parameters of pellets, in which only barium zirconate phase was obtained, were calculated from XRD patterns and plotted as a function of ionic radius of dopant cations in Fig. 3.6. We adopted the apparent lattice parameters of cubic perovskite for the pellets which might have a phase separation into two perovskite or similar structures. From Fig. 3.6, one can see a linear relationship between the lattice parameters and ionic radius of dopant cations, although the relationship is not exactly liner because of difference of chemical properties of dopant and

experimental error. Almost the linear relationship means that dissolution of dopant cation into B site of barium zirconate causes isotropic lattice strain in the structure of barium zirconate.

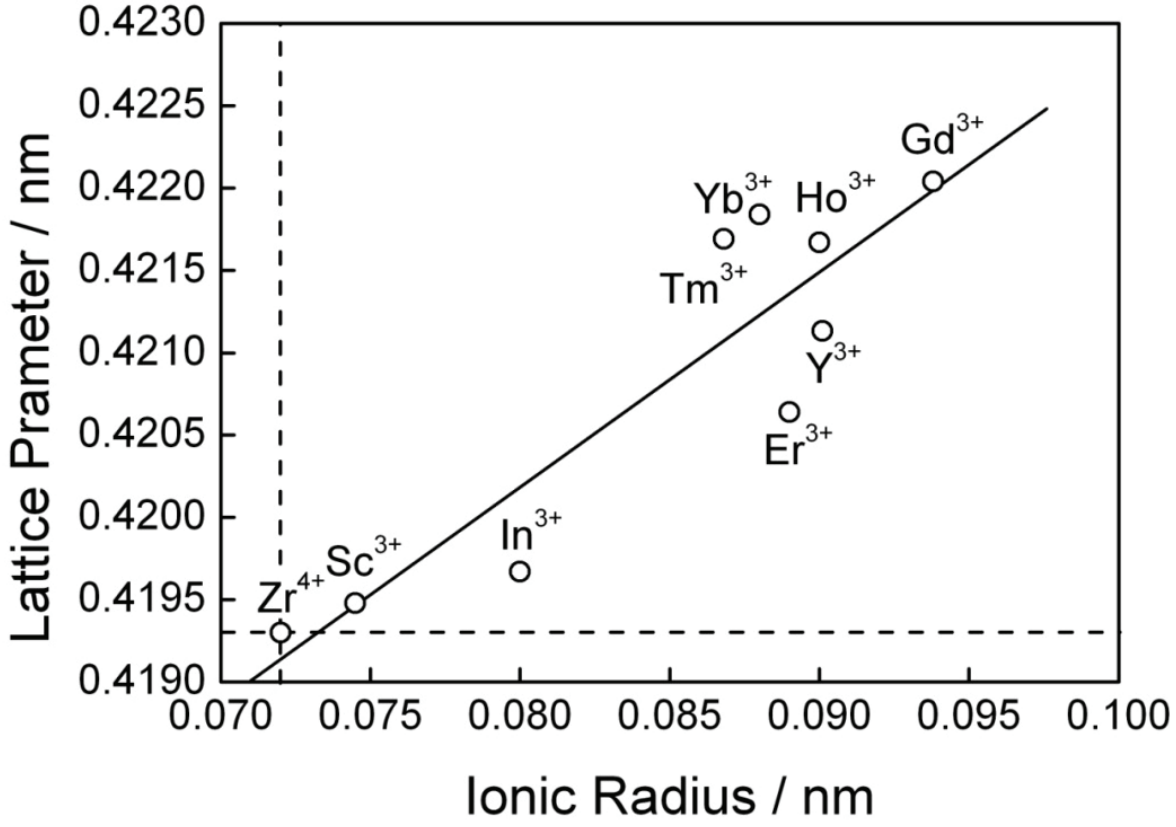

Figure 3.6 Lattice parameters of $BaZrO_3$, Sc, In, Yb, Tm, Er, Y, Ho and Gd doped barium zirconates as a function of ionic radius of the dopant cations.

3.3.3 Microstructure of Trivalent Cation (Sc, In, Yb, Tm, Er, Y, Ho, Gd) Doped Barium Zirconate

Microstructure of trivalent cation doped barium zirconate was observed by SEM. The SEM images are shown in Fig. 3.7. Good grain growth was observed in Sc, In and Gd doped barium zirconates. The microstructure of In-doped barium zirconate is quite similar to that of Sc-doped barium zirconate. As shown later, proton conductivity of In-doped barium zirconate is also same as that of Sc-doped barium zirconate. Thus, we can categorize In as an "Sc-type" dopant. We exclude Gd from the group of "Sc-type" dopants because of its large lattice parameter as shown in Fig. 3.6. In contrast, Yb, Tm, Er, Y and Ho doped barium zirconates

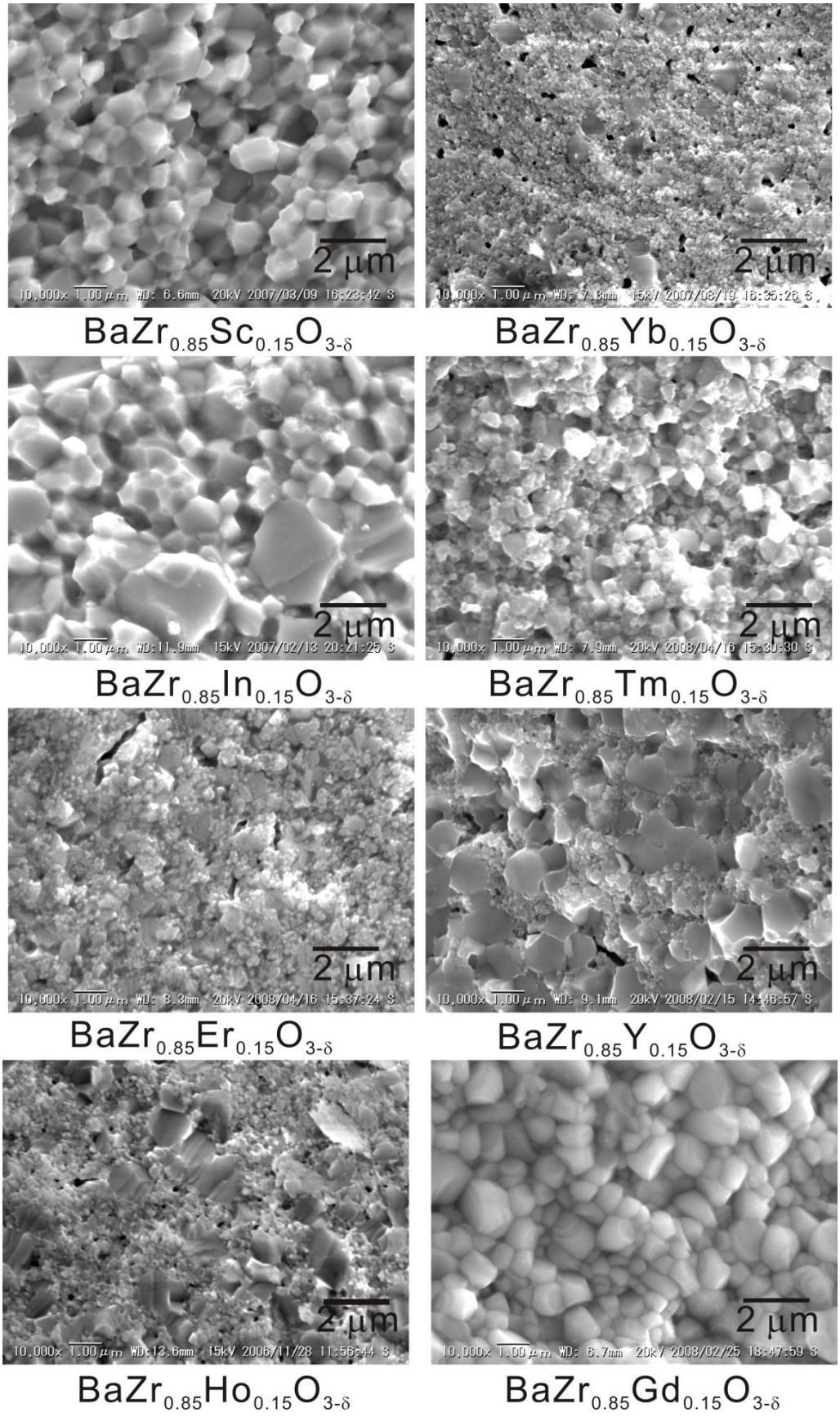

Figure 3.7 Cross-sectional SEM images of Sc, In, Yb, Tm, Er, Y, Ho and Gd doped barium zirconates.

have microstructure of mixtures of large (about 1 μm) and very fine grains (less than 100 nm). This microstructure is caused by the different phase relationships at synthesizing temperature (1300 °C) and sintering temperature (1600 °C) as described in Chapter 6. The different phase relationship requires cations to diffuse over long distances in order to reach equilibrium phase at 1600 °C, that is, 24 hours is not enough time for sintering to obtain the equilibrium phase at 1600 °C using powders synthesized by solid state reaction. In addition, the conductivity of Yb, Tm, Er, Y and Ho doped barium zirconates were higher than those of Sc and In doped barium zirconates as shown in the next section. Thus, we conclude that Yb, Tm, Er and Ho belong to "Y-type" dopants from proton conductivity data and microstructure of mixture of coarse and fine grains.

3.3.4 Bulk Conductivity of Trivalent Cation (Sc, In, Yb, Tm, Er, Y, Ho, Gd) Doped Barium Zirconate

Conductivities of Sc, In, Yb, Tm, Er, Y, Ho and Gd doped barium zirconates were evaluated from impedance spectra. There is a possibility that doped $BaZrO_3$ has electronic, oxide ion and proton conduction. At the atmosphere in this study, it is reported that electronic conduction is much smaller than proton conduction in doped $BaZrO_3$.[93Iwa] In addition, activation energy obtained in the lower temperature range than 300 °C coincided a typical activation energy for proton conduction in doped pervskites.[00Boh,01Kre] Therefore, we assumed that the measured electric conductivity of doped barium zirconate is dominated by proton conduction at temperatures lower than at least 300 °C. The bulk conductivities, σ_{bulk}, at 150 °C are plotted as a function of ionic radius of dopant cations in Fig. 3.8 (a). We summarized the qualitative characters of dopant cations in Table 3.2. In the table, we defined good proton conductivity as more than 10 μS cm^{-1} and that bad proton conductivity is less than 10 μS cm^{-1}. From the figure, "Y-type" dopant (Yb, Tm, Er, Y and Ho) has larger proton conductivity.

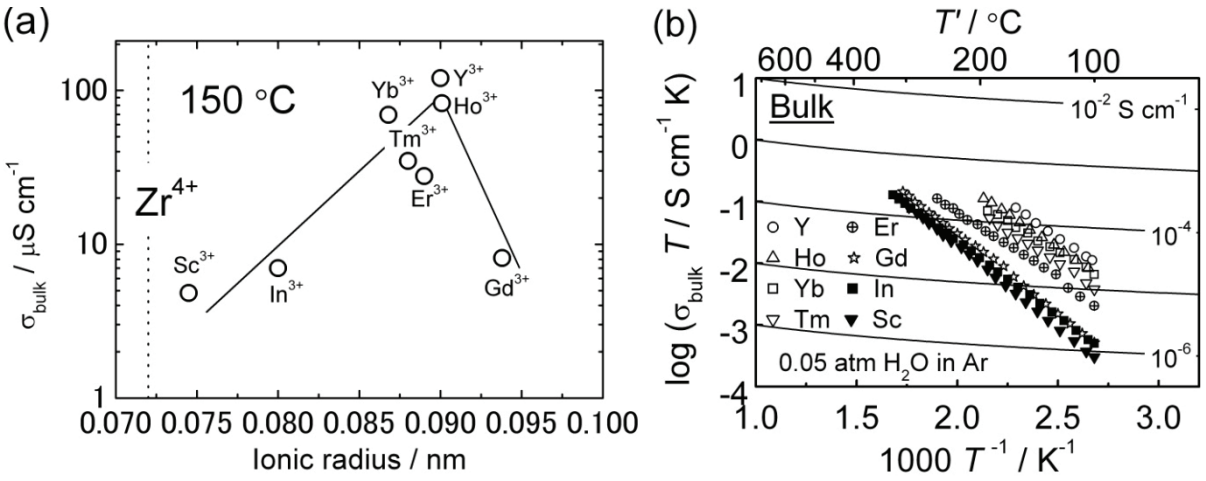

Figure 3.8 (a) Bulk conductivities, σ_{bulk}, of Sc, In, Yb, Tm, Er, Y, Ho and Gd doped barium zirconates as a function of ionic radius of dopant cations at 150 °C. (b) The bulk conductivities of Sc, In, Yb, Tm, Er, Y, Ho and Gd doped barium zirconates in Ar-0.05 % H_2O as a function of temperature plotted in the Arrhenius form.

Table 3.3 Dopant type, ionic radius of dopant cations, relative density, activation energies (E_σ) and pre-exponential terms (A) for bulk conductivity for trivalent cation doped barium zirconates.

Sample	Type	Ionic Radius (nm)	Relative Density (%)	σ_{bulk}	
				E_σ (eV)	A (S cm^{-1} K)
$BaZr_{0.85}Sc_{0.15}O_{3-\delta}$	Sc	0.0745	99.0	0.530	4.25×10^3
$BaZr_{0.85}In_{0.15}O_{3-\delta}$	Sc	0.0800	99.6	0.481	1.56×10^3
$BaZr_{0.85}Yb_{0.15}O_{3-\delta}$	Y	0.0868	99.9	0.386	1.14×10^3
$BaZr_{0.85}Tm_{0.15}O_{3-\delta}$	Y	0.0880	95.5	0.420	1.97×10^3
$BaZr_{0.85}Er_{0.15}O_{3-\delta}$	Y	0.0890	94.9	0.435	1.65×10^3
$BaZr_{0.85}Y_{0.15}O_{3-\delta}$	Y	0.0900	97.8	0.442	9.79×10^3
$BaZr_{0.85}Ho_{0.15}O_{3-\delta}$	Y	0.0901	98.0	0.435	5.40×10^3
$BaZr_{0.85}Gd_{0.15}O_{3-\delta}$	–	0.0938	97.9	0.510	4.11×10^3

Among "Y-type" dopants, Y was still the best dopant from the viewpoint of proton conductivity. In contrast, "Sc-type" dopant (Sc and In) has lower proton conductivity. This trend between proton conductivity and ionic radius is different from the data reported by Laidoudi *et al.*[02Lai] but coincided with data reported by Kreuer *et al.*[01Kre] Fig. 3.8 (b) shows the bulk conductivity of Sc, In, Yb, Tm, Er, Y, Ho and Gd doped barium zirconates in the

Arrhenius form. Activation energies (E_σ) and pre-exponential terms (A) for bulk conductivity of trivalent cation doped barium zirconates are shown in Table 3.3.

Gd-doped barium zirconate showed a different microstructure of sintered pellet from "Y-type" dopant and also showed apparently lower proton conductivity, making it similar to "Sc-type" dopant. However, in contrast to "Sc-type" dopant, the lattice parameter of Gd-doped barium zirconate was large; the largest among the dopant cations examined in this study. Considering these features, it is difficult to categorize Gd as a "Y-type" or "Sc-type" dopant. One may think that proton conductivity of Gd-doped barium zirconate becomes low because a part of Gd dissolves into A site of barium zirconate and proton concentration decreases. If a trivalent cation is substituted for A site, oxide ion vacancy decreases as given in E.q. (3-1),

$$2\,A_A^x + V_O^{\bullet\bullet} + M_2O_3 \rightarrow 2\,M_A^{\bullet} + O_O^x + 2\,AO \qquad (3\text{-}1)$$

which makes proton concentration decrease. It might be more important that occupying A site of trivalent cation may cause unflavored changes activation process for proton jump because the valence of trivalent cation is larger than that of barium ion (Ba^{2+}). Actually, we can understand this result from Table 3.3 where the activation energy for proton conduction in Gd-doped barium zirconate is larger than that in "Y-type" dopant doped barium zirconate. For example, when one A site is occupied with a trivalent cation, 24 paths for proton jump in barium zirconate is affected by the trivalent cation in A site. Fig. 3.9 describes this situation in unit cell. The substitution of trivalent cation for A site should also have a far-reaching influence on paths for proton jump. These mean that a small amount of trivalent cation which occupies A site has a big influence on activation process for proton jump. In addition, if Gd is occupied in A site, extra barium oxide might form a liquid phase because there might be a liquid phase at BaO-rich composition as seen in the case of Y-doped barium zirconate where liquid phase forms at increased composition of barium oxide from the

stoichiometric composition of 15% Y-doped barium zirconate as described in Chapter 6. We consider that the liquid phase promotes grain growth of Gd-doped barium zirconate in sintering.

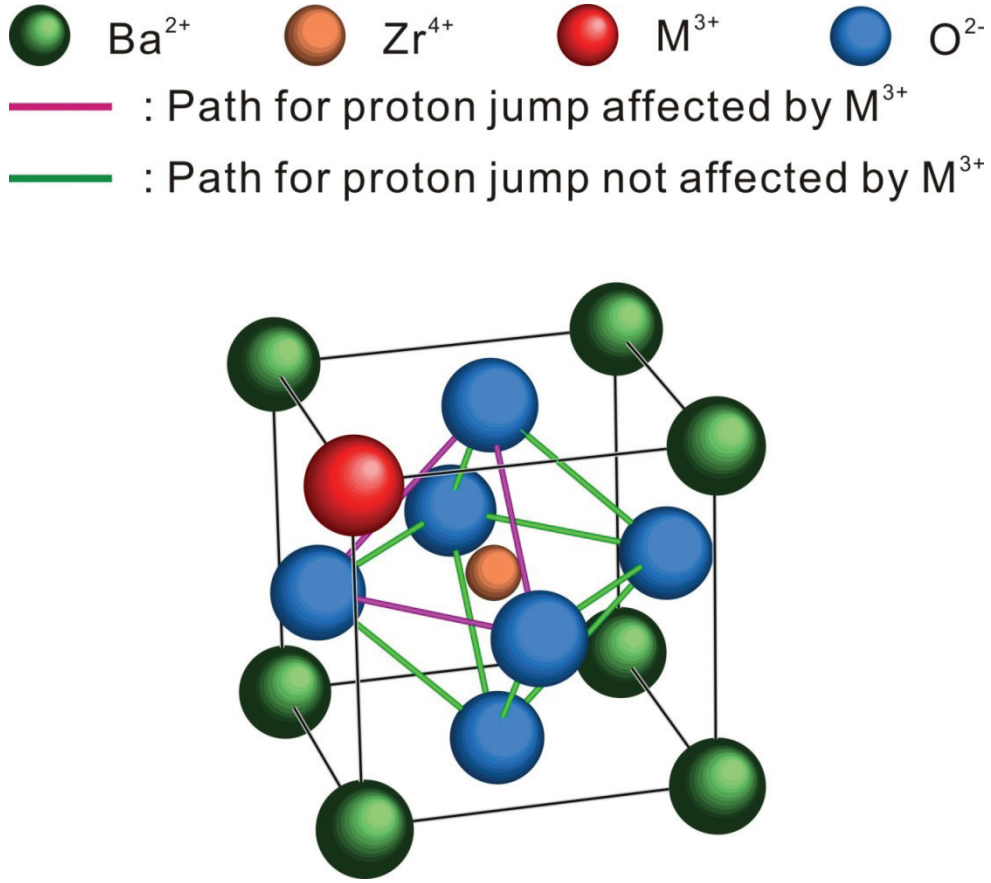

Figure 3.9 Structure of barium zirconate where trivalent cation doped in A site.

3.4 Conclusion

The results obtained in this work can be summarized as follows:

(1) We investigated the solubility of magnesium into B site of barium zirconate. The solubility of magnesium is less than 0.025 ($X_{MgO} = 0.025$).

(2) We investigated whether trivalent cations (Sc^{3+}, In^{3+}, Yb^{3+}, Tm^{3+}, Er^{3+}, Y^{3+}, Ho^{3+}, Gd^{3+}, Nd^{3+}, La^{3+}, Bi^{3+} and Ga^{3+}) can dissolve into B site of barium zirconate when the mole fraction of trivalent cation is 0.075 ($X_{MO1.5} = 0.075$). The solubilities of Sc, In, Yb, Tm, Er, Y, Ho and Gd were more than $X_{MO1.5} = 0.075$. There was a linear relationship between the

lattice parameters and ionic radii of dopant cations at $X_{MO1.5}$ = 0.075. This means that dissolution of dopant cation into B site of barium zirconate causes isotropic lattice strain in the structure of barium zirconate. On the other hand, the solubilities of Nd, La, Bi and Ga into B site of barium zirconate are less than 0.075. Ionic radii of these cations show large differences from that of zirconium ion. We can understand that large lattice strain leads to the less solubility.

(3) We classified trivalent cation doped barium zirconates into two classes from the viewpoints of development of microstructure and proton conductivity; "Y-type" dopant and "Sc-type" dopant. Yb, Ho, Er and Tm belong to "Y-type" dopants, which have a bimodal microstructure and larger proton conductivity. Among "Y-type" dopants, Y was still the best dopant from the view point of proton conductivity. In belongs to "Sc-type" dopant, which has well-grown grains and lower proton conductivity.

References

[76Sha] R. D. Shannon, *Acta Crystallographica Section A*, **32**, 751-767 (1976).

[93Man] A. Manthiram, J.F. Kuo, and J.B. Goodenough, *Solid State Ionics*, **62**, 225-234 (1993).

[93Iwa] H. Iwahara, T. Tajima, T. Hibino, K. Ozaki, and H. Suzuki, *Solid State Ionics*, **61**, 65-69 (1993).

[95Sla] RCT. Slade, S.D. Flint, and N. Singh, *Solid State Ionics*, **82**, 135-141 (1995).

[00Boh] H. G. Bohn and T. Schober, *Journal of the American Ceramic Society*, **83,** 768-772 (2000).

[01Kre] K. D. Kreuer, S. Adams, W. Munch, A. Fuchs, U. Klock, and J. Maier, *Solid State Ionics,* **145,** 295-306 (2001).

[02Lai] M. Laidoudi, I.A. Talib, and R. Omar, *Journal of Physics D: Applied Physics*, **35,** 397-401 (2002).

[04Oma] T. Omata, M. Takagi, and S.-O.-Y. Matsuo, *Solid State Ionics*, **168**, 99-109 (2004).

[04Wu] J. Wu, L.P. Li, W.T.P Esponosa, and S.M. Haile, *Journal of Materials Research*, **19**, 2366-2376 (2004).

[06Ahm1] I. Ahmed, S.G. Eriksson, E. Ahlberg, C.S. Knee, P. Berastegui, L.G. Johansson, H. Rundlöf, M. Karlsson, A. Matic, M. Karlsson, L. Börjesson, and D. Engberg, *Solid State Ionics*, **177**, 1395-1403 (2006).

[06Ahm2] I. Ahmed, E. Ahlberg, S.G. Eriksson, C.S. Knee, M. Karlsson, A. Matic, and L. Börjesson, *Ceramic Engineering and Science Proceedings*, **27**, 105-117 (2006).

[07Ahm] I. Ahmed, S.G. Eriksson, E. Ahlberg, C.S. Knee, H. Götlind, L.G. Johansson, M. Karlsson, A. Matic, and L. Börjesson, *Solid State Ionics*, **178**, 515-520 (2007).

[08Ito] N. Ito, H. Matsumoto, Y. Kawasaki, S. Okada, T. Ishihara, *Solid State Ionics*, **179**, 324-329 (2008).

Chapter 4

A Pseudoternary Phase Diagram of the BaO-ZrO_2-$YO_{1.5}$ System at 1600 °C and Solubility of Yttria into Barium Zirconate

4.1 Introduction

In the previous chapter, we classified trivalent cation doped barium zirconates into two classes from the viewpoints of development of microstructure and proton conductivity; "Y-type" dopant and "Sc-type" dopant. "Y-type" dopants have a bimodal microstructure and larger proton conductivity. "Sc-type" dopants have well-grown grains and lower proton conductivity. In this chapter, we try to investigate phase relationship at synthesizing temperature, 1300 °C, and sintering temperature, 1600 °C, in order to explain the difference of the sintering behavior between "Y-type" dopant and "Sc-type" dopant. But, the study of phase equilibrium at 1300 C was kinetically difficult. Therefore, in this chapter, phase relationship of the BaO-ZrO_2-$YO_{1.5}$ system at 1500 and 1600 °C was examined.

To achieve equilibrium in short time, it is necessary for raw materials to be well mixed and the grain size of used powder has to be fine. The powder of barium zirconate obtained by a conventional solid-state reaction is about 50 nm. On the other hand, it is reported that very fine powder of barium titanate ($BaTiO_3$) (10-15 nm) was obtained by a nitrate freeze-drying method.[96Mch] Thus, in this study, we applied a nitrate freeze-drying method.

4.2 Experimental

4.2.1 Material Preparation

The reagents used were barium nitrate ($Ba(NO_3)_2$: 99.9%, Wako), zirconyl nitrate dihydrate ($ZrO(NO_3)_2 \cdot 2H_2O$: 97.0%, Wako), and yttrium nitrate *n*-hydrate ($Y(NO_3)_3 \cdot nH_2O$: 99.9 %, Wako). Zirconyl nitrate dihydrate was dissolved in 0.1 M nitric acid (HNO_3) and then the solution was filtered to remove a small amount of zirconia (ZrO_2) in the solution. Yttrium

nitrate *n*-hydrate was dissolved in 0.1 M nitric acid. The concentrations of the two solutions were measured by inductive coupled plasma-atomic emission spectroscopy (ICP-AES) (Seiko Instruments Inc., SPS4000). The zirconyl nitrate solution contained 2.07 mass% of hafnium (Hf) as an impurity. The chemical properties of hafnium are quite similar to those of zirconium. Thus, hafnium is expected to substitute the zirconium site and behave as like zirconium. In addition, 2.07 mass% of hafnia (HfO_2) corresponds to only 1.08 mol% of hafnia in the ZrO_2-HfO_2 system. Such a small percentage does not affect on the phase relationship. Thus, we neglected the affect of hafnia on the results. Then, the two solutions of zirconyl nitrate and yttrium nitrate were mixed them and barium nitrate powder was mixed with the solution. The composition of the mixed solution was confirmed again by ICP-AES, and the barium concentration of the mixed solution was about 0.08 M. About 250 ml of the mixed solution was atomized using an ultrasonic spray nozzle (Sonotek, 06-5108) and rapidly frozen by leading the aerosol to fall into stirred liquid nitrogen as shown in Fig. 4.1. The frozen solution was vacuum-dried in a freeze dryer (DRC-1100 and FDU-2100, EYEA) operated at reduced pressure and temperature (5 Pa, –40 °C), with monitoring temperatures in the frozen solution by a thermocouple. The temperature in the frozen solution indicated a constant value (about -43 °C) until the sublimation of the solution finished. We could know the end of sublimation by checking that the temperature of the frozen solution began to rise. Then, the temperature of the freeze dryer was quite gradually increased to 25 °C. When the powder was completely dried at 25 °C, the vacuum chamber was backfilled with air and the resulting freeze-dried powder was stored in a sealed bottle. The powder was moved to electric furnace and heated at 500 °C for 10 hour in vacuum. The experimental condition of nitrate freeze dry method is considered in Chapter 9 in detail. Then, the powder after heating at 500 °C was ball-milled for 10 hours. The powder was pressed into a pellet at 392 MPa. Subsequently, the pellet was moved to a furnace already heated at 1600 °C and then kept at that temperature for

24 hours in air. The same procedure was repeated at 1500 °C for 100 hours. The heated pellets were quenched to room temperature. At elevated temperatures, barium oxide (BaO) has a significantly high vapor pressure (*ca*, 8×10^{-5} atm at 1600 °C[95Bar]). There is a possibility for a part of the barium oxide in the pellets to vaporize, which causes deviation of the pellet composition from the nominal compositions at 1500 and 1600 °C. Therefore, during the heat-treating, a sacrifice powders which consists of 90 mass % of the same composition as pellet and 10 mass% of barium carbonate ($BaCO_3$: 99.9 %, Wako) was used to suppress the vaporization of barium oxide from the samples except experiments of X_{BaO} = 0.30. The sacrifice powders were synthesized by a solid state reaction described in Chapter 2. The temperature of samples during heat-treating was checked using thermal history sensor (Referthomo type H, AS ONE). The temperature deviation in the experiments was within 1600 ± 10 and 1500 ± 5 °C.

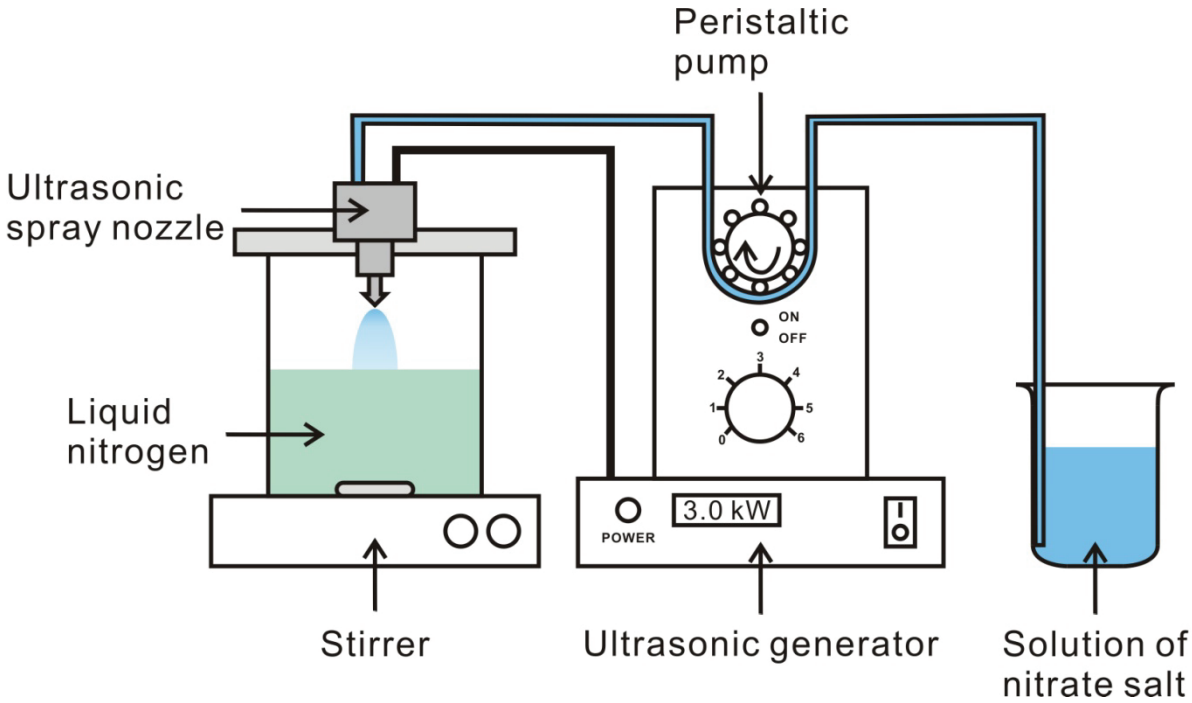

Figure 4.1 Schematic view of apparatus for obtaining atomized frozen powder.

Table 4.1 Nominal compositions, compositions of quenched samples and phases identified by X-ray diffraction in samples heat-treatment at 1600 °C for 24 hours in air. ○: detected, ×: undetected and –: not investigated.

Sample	Nominal composition			Composition after quench			Identified phase by XRD after 1600 °C			
	X_{BaO}	X_{ZrO2}	$X_{YO1.5}$	X_{BaO}	X_{ZrO2}	$X_{YO1.5}$	$BaZrO_3$	BZY424	ZrO_2 (cubic)	Y_2O_3
A	0.303	0.638	0.052	–	–	–	○	×	○	×
B	0.299	0.540	0.156	–	–	–	○	×	○	×
C	0.304	0.444	0.351	–	–	–	○	×	○	×
D	0.305	0.340	0.351	0.298	0.335	0.364	○	×	×	○
E	0.313	0.250	0.434	0.301	0.250	0.446	○	×	×	○
F	0.306	0.151	0.542	0.269	0.146	0.583	○	×	×	○
G	0.301	0.064	0.635	0.209	0.060	0.731	○	○	×	○
H	0.399	0.177	0.423	0.411	0.166	0.421	○	○	×	○
I	0.408	0.206	0.384	0.421	0.196	0.391	○	○	×	○
J	0.499	0.422	0.075	0.502	0.419	0.075	○	×	×	×
K	0.497	0.301	0.198	0.490	0.300.	0.207	○	×	×	×
L	0.490	0.260	0.247	0.493	0.251	0.253	○	○	×	×
M	0.496	0.200	0.302	0.472	0.206	0.320	○	○	×	×
N	0.296	0.299	0.402	–	–	–	–	–	–	–

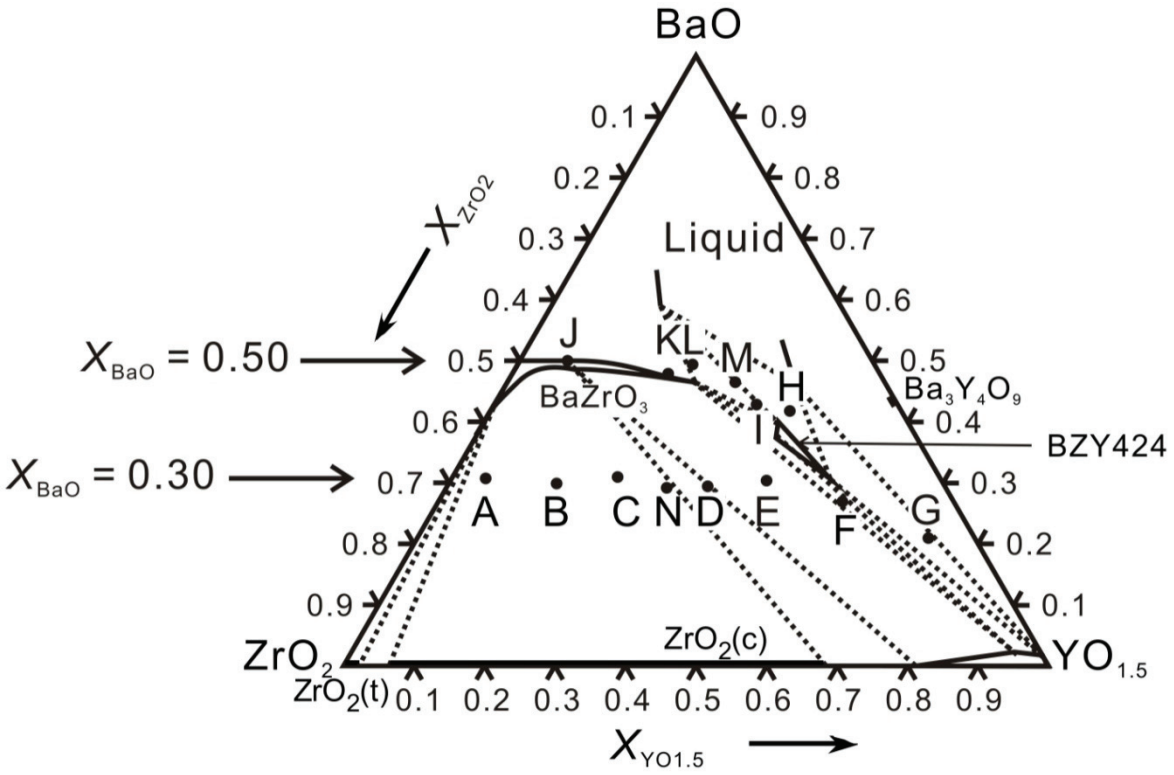

Figure 4.2 Nominal compositions (sample A to C) and compositions of quenched samples (sample D to M) used in this study. Abbreviations of sample names are referred to Table 4.1.

4.2.2 Chemical Analysis and Phase Identification

The nominal compositions and compositions of quenched samples examined in this work are listed in Table 4.1 with results of phase identification of quenched samples by X-ray diffraction analysis (XRD, PANalytical, X'Pert-ProMPD, Cu-Kα). Figure 4.2 shows the average compositions of quenched samples on a pseudoternary phase diagram of the BaO-ZrO_2-$YO_{1.5}$ system. The nominal compositions of samples were the compositions of freeze-dried powders which is measured by ICP-AES. In case of the measurement of ICP-AES, the freeze-dried powders were dissolved into 0.1 M nitric acid and diluted by 0.1 M nitric acid to the extent that the concentrations of barium ion were in between 1.0 and 10 ppm. Also, the quenched samples were crushed into powders and the powders dissolved into 5.7 M hydrochloride acid. Then, the solutions were diluted by deionized water to extend that the concentrations of hydrochloride acid became 0.06 M and that the concentrations of barium

ion were in between 1.0 and 10 ppm, and the compositions of the solutions were measured by ICP-AES. The compositions of quenched samples which zirconia precipitated (sample A, B and C) were not measured by ICP-AES. The compositions of each grain in quenched samples were analyzed by energy dispersive X-ray microanalysis (EDX) (JEOL, JED-2300) equipped with field emission-scanning electron microscope (FE-SEM) (JEOL, JSM-6500F). The compositions of each grain in samples by EDX were calibrated based on the assumption that the average compositions of samples analyzed by EDX are equal to the nominal compositions (sample A to C and N) or compositions of quenched samples (sample D to M) by ICP-AES. Diffraction patterns of the pellets were observed using transmission electron microscope (TEM) (JEOL, JSM-6500F).

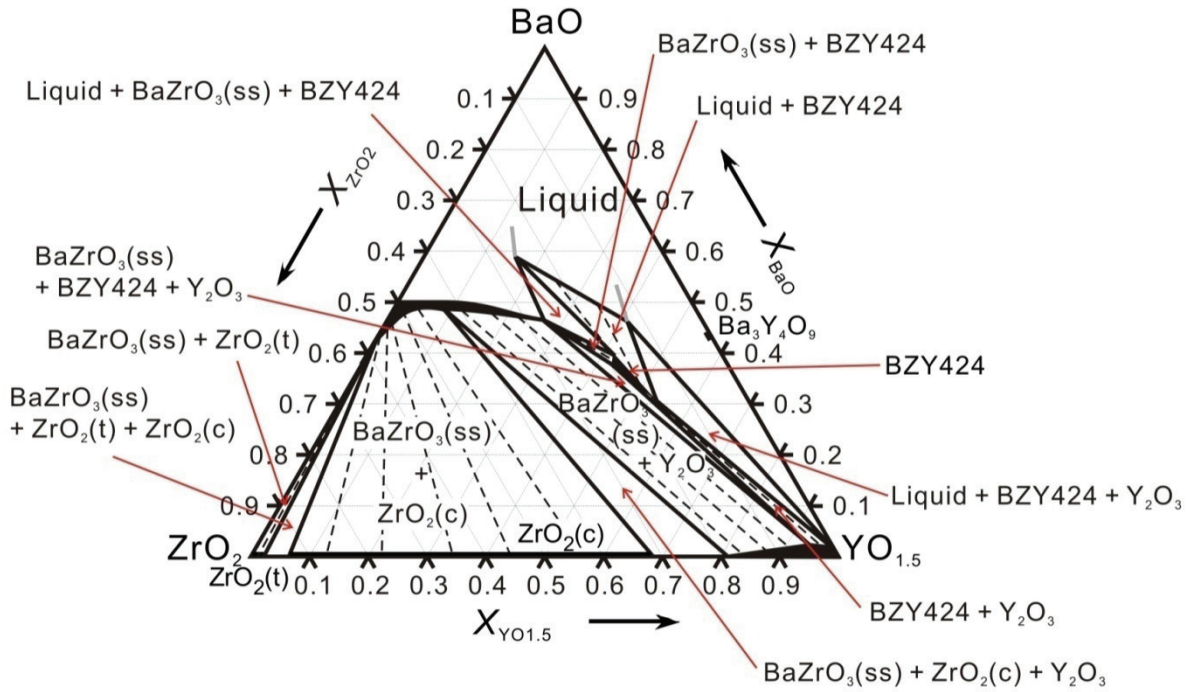

Figure 4.3 Established pseudoternary phase diagram of the BaO-ZrO_2-$YO_{1.5}$ system at 1600 °C. ZrO_2(t) and ZrO_2(c) denote tetragonal zirconia and cubic zirconia, respectively.

4.3. Results and Discussion

We established the pseudoternary phase diagram of the BaO-ZrO_2-$YO_{1.5}$ system at 1600 °C as shown in Fig. 4.3. To establish this phase diagram, we combined information of experimental pseudobinary phase diagrams of a BaO-ZrO_2 system[87Pas] and a BaO-$YO_{1.5}$ system[90Rot,91Ses,91Zha,94Hor], and a ZrO_2-$YO_{1.5}$ system[74Sri,88Stu] in air. There is only one reported phase diagram in the BaO-ZrO_2 system, but there are many phase diagrams in the BaO-ZrO_2 system. The phase relationship of the BaO-$YO_{1.5}$ system at 1600 °C in all the reported phase diagrams coincides. On the other hand, there are many proposed experimental phase diagrams of a ZrO_2-$YO_{1.5}$ system.[63Fan,71Rou,78Gor74Sri,75Sco, 83Pas,88Stu,96Yas] Among these phase diagrams, the phase relationship at 1600 °C coincides well, but the solubility of yttria into tetragonal and cubic zirconia phase at 1600 °C and the solubility of zirconia into yttria at 1600 °C are different.[71Rou,74Sri75Sco,88Stu] Combining with our experimental results, we adopted the solubility of yttria into tetragonal and cubic zirconia phase at 1600 °C from the phase diagram reported by Srivastava *et al.* [74Sri] and the solubility of zirconia into yttria at 1600 °C from the phase diagram reported by Stubican *et al.* [88Stu]

4.3.1 Analysis of X-ray Diffraction and Results of EDX Analysis of X_{BaO} = 0.30 at 1600 °C

Samples on the composition line of X_{BaO} = 0.30 were heat-treated at 1600 °C for 24 hours. XRD patterns of the samples are shown in Fig. 4.4 (a) and (b), and the identified phases are summarized in Table 4.1. As it was difficult to judge only by XRD whether zirconia phase or yttria phase exists because of their similarity in diffraction patterns, the results of EDX was utilized to determine the phases. The compositions of each grain in the samples were analyzed by EDX and the results on pseudoternary phase diagrams of BaO-ZrO_2-$YO_{1.5}$ system are shown in Fig.4.5 (a) and (b). Some compositions analyzed by EDX

(a)

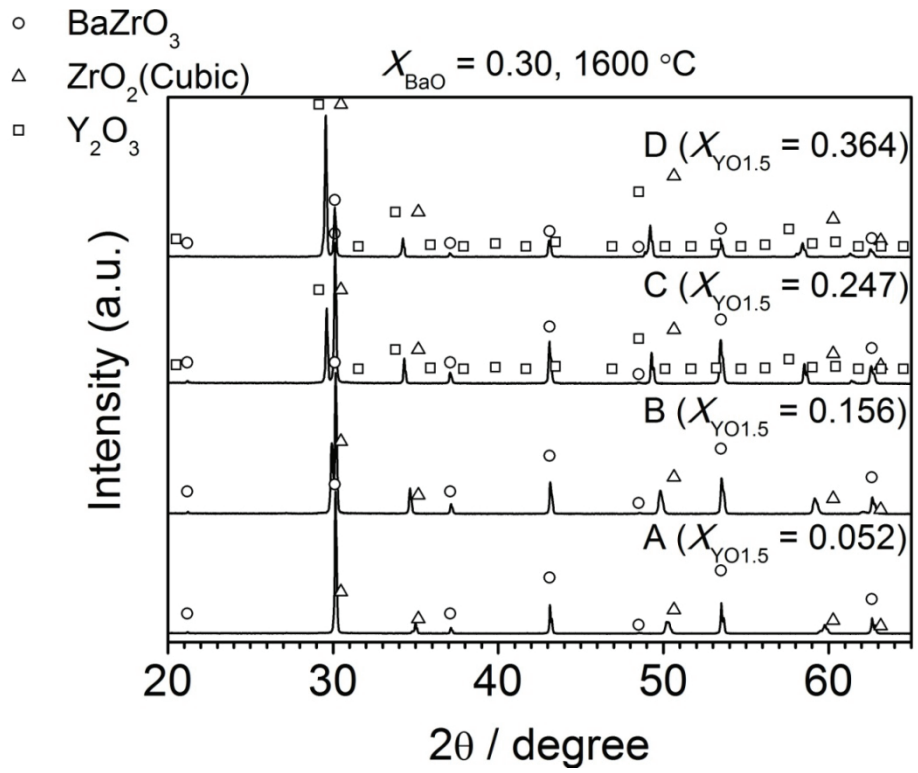

(b)

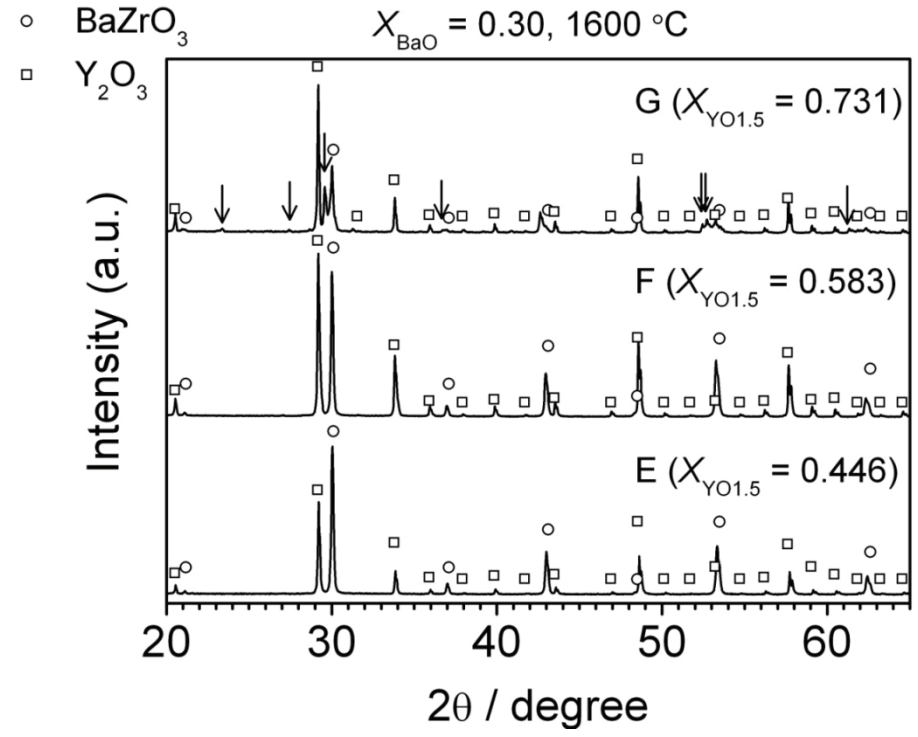

Figure 4.4 XRD patterns of samples at X_{BaO} = 0.30 after heat-treating at 1600 °C for 24 hours ((a) sample A to D, (b) sample E to G). Each symbol indicates diffraction patterns of ○ ($BaZrO_3$, JCPDS No. 00-006-0399), △ (ZrO_2, JCPDS No. 00-027-0997) and □ (Y_2O_3, JCPDS No. 00-043-1036).

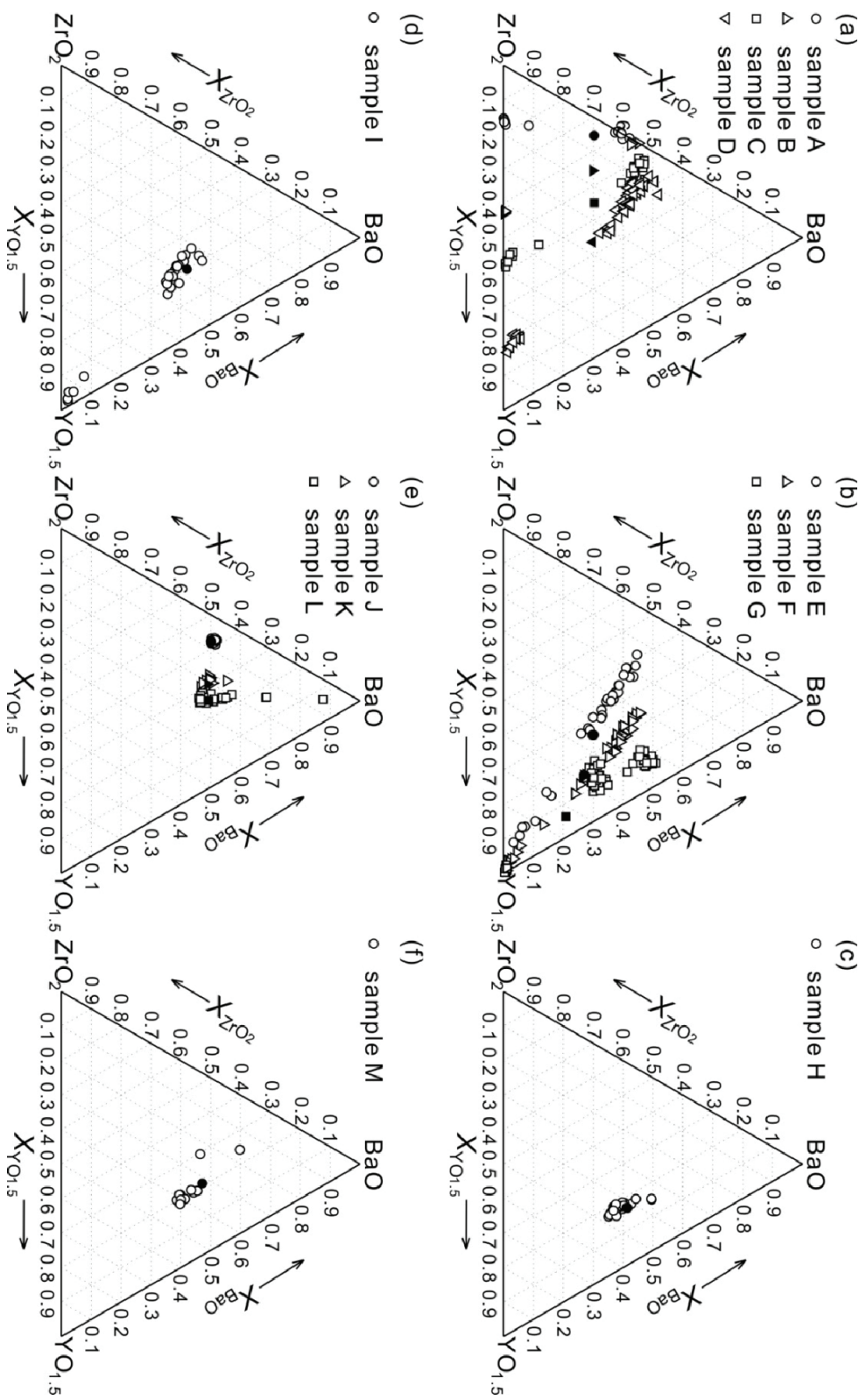

Figure 4.5 Results of EDX analysis in samples after heat-treating at 1600 °C for 24 hours on pseudoternary phase diagrams of BaO-ZrO_2-$MO_{1.5}$ system ((a) sample A to D, (b) sample E to G, (c) sample H, (d) sample I, (e) sample J to L, (f) sample M). Filled point is an average composition of each sample.

Table 4.2 Compositions of each grain in samples after heat-treating at 1600 °C for 24 hours by EDX analysis.

Sample	Barium zirconate (Pervskite)			New phase (Pervskite)			ZrO_2			Y_2O_3			Trace of liquid phase	
	X_{BaO}	X_{ZrO2}	$X_{YO1.5}$	X_{BaO}	X_{ZrO2}	$X_{YO1.5}$	X_{BaO}	X_{ZrO2}	$X_{YO1.5}$	X_{BaO}	X_{ZrO2}	$X_{YO1.5}$	X_{BaO}	X_{ZrO2}	$X_{YO1.5}$
A	0.42	0.58	0.00	(n.d.)			0.00	0.85	0.15	(n.d.)			(n.d.)		
B	0.43	0.56	0.01	(n.d.)			0.00	0.57	0.43	(n.d.)			(n.d.)		
C	0.49	0.47	0.04	(n.d.)			0.00	0.42	0.58	(n.d.)			(n.d.)		
D	0.49	0.44	0.07	(n.d.)			(n.d.)			0.01	0.16	0.83	(n.d.)		
E	0.45	0.41	0.14	(n.d.)			(n.d.)			0.03	0.07	0.89	(n.d.)		
F	0.46	0.24	0.31	0.38	0.20	0.43	(n.d.)			0.01	0.00	0.99	(n.d.)		
G	(n.d.)			0.31	0.16	0.53	(n.d.)			0.01	0.00	0.99	0.47	0.12	0.41
H	(n.d.)			0.36	0.18	0.47	(n.d.)			(n.d.)			0.50	0.15	0.35
I	0.44	0.25	0.31	0.35	0.17	0.48	(n.d.)			0.02	0.02	0.96	0.46	0.22	0.32
J	0.50	0.42	0.08	(n.d.)			(n.d.)			(n.d.)			(n.d.)		
K	0.47	0.31	0.23	(n.d.)			(n.d.)			(n.d.)			(n.d.)		
L	0.46	0.28	0.26	(n.d.)			(n.d.)			(n.d.)			0.69	0.17	0.15
M	0.47	0.30	0.24	0.40	0.19	0.42	(n.d.)			(n.d.)			0.60	0.24	0.16

were average values of two or more grains which have different compositions, because the spot size of the electron beam in FE-SEM is wider than some single grains and the penetrated beam diverges in the grains. If compositions analyzed by EDX were average values of two different grains, the compositions are on the line connecting composition points of the different grains. Considering this point, we observed four types of grains by combining the result of XRD in this study and the compositions were summarized in Table 4.2. When the mole fraction of yttria was 0.052 ($X_{YO1.5}$ = 0.052 (sample A)) and 0.156 ($X_{YO1.5}$ = 0.156 (sample B)), cubic barium zirconate phase ($BaZrO_3$(ss)) and cubic zirconia phase were identified by XRD analysis. As seen in Fig. 4.4 (a), the peak positions of the cubic zirconia phase in sample B shifted to lower angles than those of the cubic zirconia phase in JCPDS card [No. 00-027-0997, lattice parameter, a = 0.50900 nm], which is due to dissolution of yttria into the cubic zirconia phase as reported by Pascual *et. al*.[83Pas] When $X_{YO1.5}$ = 0.247 (sample C) and 0.364 (sample D), cubic barium zirconate phase ($BaZrO_3$(ss)) was identified by XRD analysis, but we could not determine whether peak patterns other than cubic barium zirconate phase ($BaZrO_3$(ss)) belong to yttria phase or cubic zirconia phase. On the other hand, a grain in sample C, whose composition is X_{BaO} = 0, X_{ZrO2} = 0.42 and $X_{YO1.5}$ = 0.58, was detected by EDX analysis, and it is reported that the solubility of yttria into zirconia is $X_{YO1.5}$ = 0.69 at 1600 °C.[74Sri] Thus, we considered that sample C consists of cubic barium zirconate phase ($BaZrO_3$(ss)) and cubic zirconia phase. In the same way, a grain in sample D, whose composition is X_{BaO} = 0.01, X_{ZrO2} = 0.16 and $X_{YO1.5}$ = 0.83, was detected by EDX analysis, and it is reported that the solubility of zirconia into yttria is X_{ZrO2} = 0.19 at 1600 °C.[88Stu] Thus, we consider that sample D consists of cubic barium zirconate phase ($BaZrO_3$(ss)) and yttria phase. When $X_{YO1.5}$ = 0.446 (sample E) and 0.583 (sample F), cubic barium zirconate phase ($BaZrO_3$(ss)) and yttria phase were identified by XRD analysis (Fig. 4.4. (b)). The intensities of the peaks of the yttria phase increased with increasing mole fraction of yttria. On the other

hand, there were two kinds of which consist of barium, yttrium and zirconium in sample F by EDX analysis. One is cubic barium zirconate phase ($BaZrO_3$(ss)), and the other is a new phase. But we could not distinguish between these two phases by XRD. These two phases seemed to have similar perovskite structures. When $X_{YO1.5}$ = 0.750 (sample G), cubic barium zirconate phase ($BaZrO_3$(ss)), yttria phase and unknown phase shown as arrows were identified by XRD. From the result of EDX analysis (Table 4.2), the detected phase in sample G (X_{BaO} = 0.47, X_{ZrO2} = 0.12 and $X_{YO1.5}$ = 0.41) corresponds to the new phase in sample F. Thus, we call the new phase as BZY424 phase in this paper. Also, another grain, whose composition is X_{BaO} = 0.47, X_{ZrO2} = 0.12 and $X_{YO1.5}$ = 0.41, was observed by EDX analysis in sample G and a trace of liquid phase (tabular grains) was observed by SEM as shown in Fig. 4.6. The existence of liquid phase at BaO-rich region at 1600 °C was reported by Kojima *et. al*.[06Koj] Thus, the grain, whose composition is X_{BaO} = 0.47, X_{ZrO2} = 0.12 and $X_{YO1.5}$ = 0.41, is considered to be a trace of liquid phase.

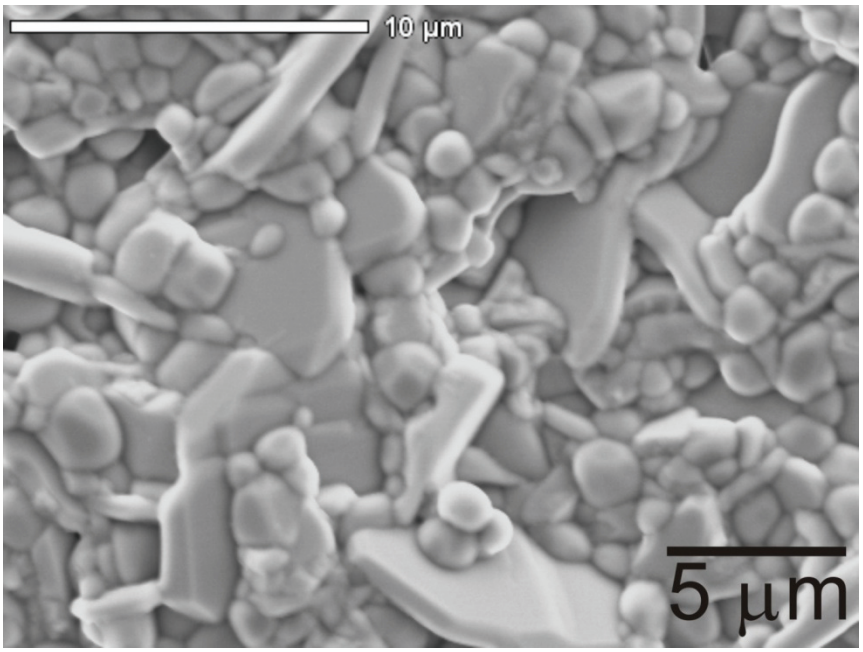

Figure 4.6 SEM images of sample G after heat-treating at 1600 °C.

4.3.2 Analysis of X-ray Diffraction and Results of EDX Analysis of Samples of the New Phase BZY424

To investigate the new phase (BZY424 phase), we made samples whose composition is near to the new barium zirconate phase. The compositions of quenched samples were X_{BaO} = 0.411, X_{ZrO2} = 0.166 and $X_{YO1.5}$ = 0.421 (sample H), and X_{BaO} = 0.418, X_{ZrO2} = 0.204 and $X_{YO1.5}$ = 0.376 (sample I). The compositions of grains in the samples analyzed by EDX are shown on pseudoternary phase diagrams of BaO-ZrO_2-$YO_{1.5}$ system in Fig. 4.5 (c) and (d), and the compositions of each grain in the samples were surmised in Table 4.2. Both samples had a grain whose composition is near to BZY424 phase, but sample I was not in single phase region. Combining the results of EDX analysis in sample F, G, H, I and M (M is described latter), BZY424 phase is not rigid stoichiometric phase and form wide solid solution. The composition of BZY424 seems to change from ~ 0.31 to ~ 0.40 in X_{BaO}, from ~ 0.16 to ~ 0.25 in X_{ZrO2} and from ~ 0.42 to ~ 0.53 in $X_{YO1.5}$.

There was a grain whose composition is X_{BaO} = 0.50, X_{ZrO2} = 0.15 and $X_{YO1.5}$ = 0.35 in sample H, and a grain whose composition is X_{BaO} = 0.46, X_{ZrO2} = 0.22 and $X_{YO1.5}$ = 0.32 in sample I. We assume that these grains also correspond to liquid phase because these compositions are similar to that of liquid phase in sample G. As seen in Table 4.2, four types of grains existed in sample I, which violate the phase rule. Some kinds of grains might be decomposition products of liquid phase during cooling. Considering a phase relationship and other experimental results, there is a possibility that yttria phase is the decomposition product of liquid phase.

XRD patterns of sample H and I are shown in Fig. 4.7, and the identified phases are summarized in Table 4.1. In sample H and I, there were clear peak patterns of yttria phase, and some of diffraction peaks coincide with these from cubic barium zirconate phase ($BaZrO_3$(ss)). However, combining the results of EDX analysis, the peaks other than those of

yttria should be peaks of BZY424 phase and/or a trace of liquid phase in sample H, and a part of cubic barium zirconate phase ($BaZrO_3$(ss)) and BZY424 phase and/or a trace of liquid phase in sample I, respectively. The unknown phase in sample G might be peak patterns of BZY424 phase.

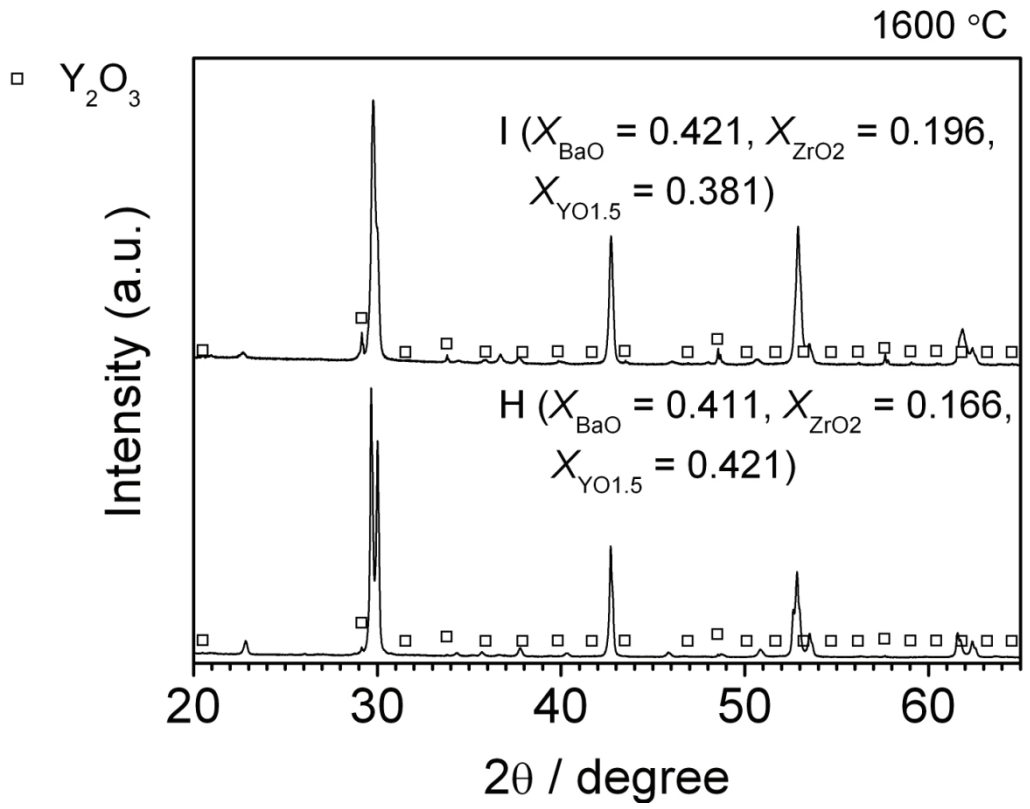

Figure 4.7 XRD patterns of sample H and I after heat-treatment at 1600 °C for 24 hours. Each symbol indicates diffraction patterns of □ (Y_2O_3, JCPDS No. 00-043-1036).

4.3.3 Analysis of X-ray Diffraction and Results of EDX Analysis of Samples of X_{BaO} = 0.50 at 1600 °C

Figure 4.8 (a) shows XRD patterns of samples at X_{BaO} = 0.50 which were heat-treated at 1600 °C for 24 hours, and the identified phases are summarized in Table 4.1. In sample J ($X_{YO1.5}$ = 0.075) and K ($X_{YO1.5}$ = 0.207), only the cubic barium zirconate phase ($BaZrO_3$(ss)) was detected. By EDX analysis, it was confirmed that almost all grains of the barium zirconate phase in sample J and K had the same compositions as the average compositions of

(a)

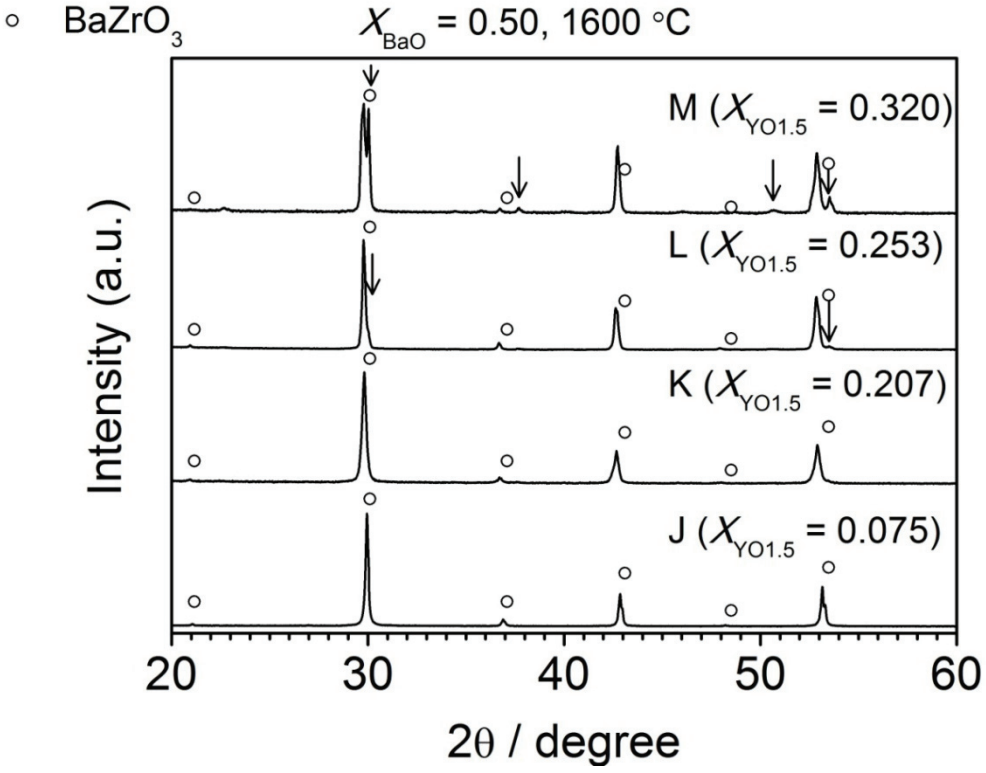

(b)

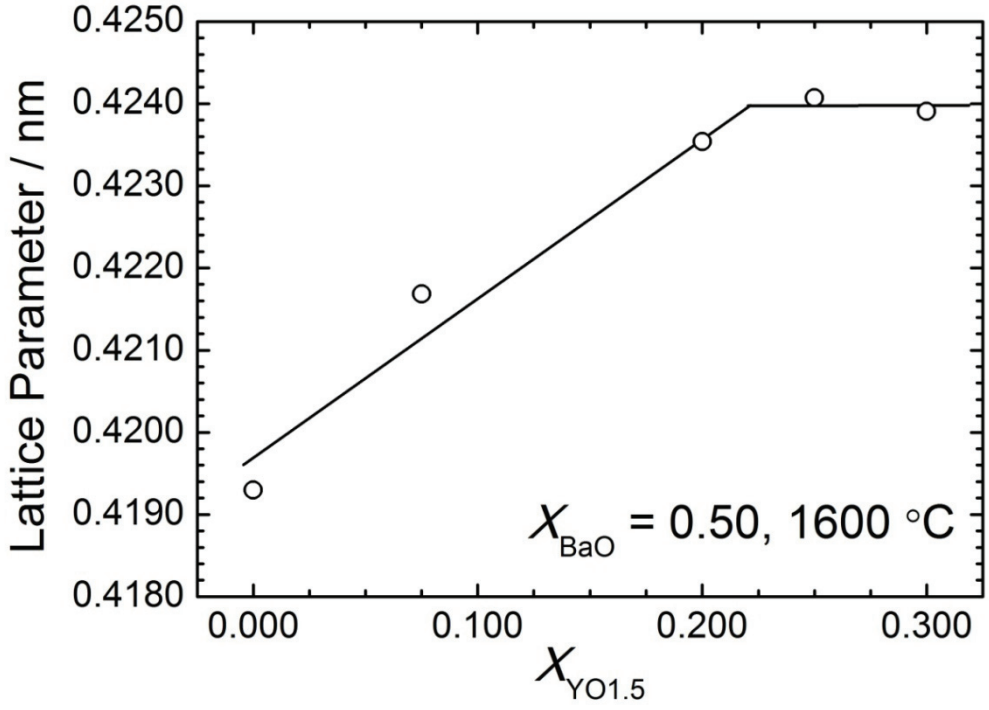

Figure 4.8 (a) XRD patterns of samples at X_{BaO} = 0.50 after heat- treatment at 1600 °C for 24 hours. Each symbol indicates diffraction patterns of ○ ($BaZrO_3$, JCPDS No. 00-006-0399). (b) Lattice parameters of barium zirconate phase as a function of the mole fraction of yttria, $X_{YO1.5}$.

each sample as shown in Fig. 4.5 (e). In sample L ($X_{YO1.5}$ = 0.253) and M ($X_{YO1.5}$ = 0.320), peak patterns of cubic barium zirconate phase ($BaZrO_3$(ss)) and BZY424 phase shown as arrows were identified by XRD analysis. Also, grains at BaO-rich region in sample L and M were observed by EDX analysis as shown in Fig 4.5 and Table 4.2. These grains are considered to be a trace of liquid phase. Fig. 4.8 (b) shows variation of lattice parameters of cubic barium zirconate phase ($BaZrO_3$(ss)) in sample J to M as a function of the mole fraction of yttria, $X_{YO1.5}$ with reported lattice parameter of $X_{YO1.5}$ = 0 in JCPDS card [No. 00-006-0399, lattice parameter, a = 0.419300 nm]. Lattice parameters of cubic barium zirconate phase ($BaZrO_3$(ss)) increased by doping yttrium until between $X_{YO1.5}$ = 0.198 and 0.247 because the ionic radius of yttrium ion (Y^{3+}: 0.0900 nm[76Sha]) is larger than that of zirconium ion (Zr^{4+}: 0.072 nm[76Sha]) and yttrium ions are doped into zirconium sites. After that, the lattice parameters were almost constant because these compositions locate in two or three phase region in the phase diagram. Thus, the solubility of yttria into cubic barium zirconate at X_{BaO} = 0.50 is between $X_{YO1.5}$ = 0.207 and 0.253. By EDX analysis, the mole fraction of yttria in cubic barium zirconate phase of sample L and M were 0.24 and 0.26, respectively. Thus, the solubility of yttria into barium zirconate is determined to be $X_{YO1.5}$ = 0.25 at 1600 °C. Also, in sample K, L and M, cubic barium zirconate phase ($BaZrO_3$(ss)) had barium deficiency as shown in Table 4.2. This might be because a part of yttrium cation dissolves into Ba site.

4.3.4 Phase Relationship of the BaO-ZrO_2-$YO_{1.5}$ System at 1500 °C

It is reported by Oyama *et al.* that another barium zirconate phase, whose composition is X_{BaO} = 0.50, X_{ZrO2} = 0.33 and $X_{YO1.5}$ = 0.17, exists at temperatures lower than 1600 °C, which is called as BZ(II) in their reports.[06Koj,08Oya] We examined to confirm the existence of the reported barium zirconate phase at 1500 °C. Samples on the composition line of X_{BaO} = 0.30 (sample C, D and N) were heat-treated at 1500 °C for 100 hours in air. XRD patterns of

these samples are shown in Fig. 4.9 and compositions of grains in the samples analyzed by EDX are shown on pseudoternary phase diagrams of BaO-ZrO_2-$YO_{1.5}$ system in Fig. 4.10. The compositions of each grain in the samples were surmised in Table 4.3. At $X_{YO1.5}$ = 0.247 (sample C), cubic barium zirconate phase ($BaZrO_3$(ss)) and cubic zirconia phase were identified. There were two kinds of grains of barium zirconate phase in sample C as shown in Fig 4.10 (a) and Table 4.3. A grain, whose composition was X_{BaO} = 0.50, X_{ZrO2} = 0.39 and $X_{YO1.5}$ = 0.12, was detected by EDX, and the composition was close to $Ba_3Zr_3YO_{3-\delta}$ which was different from BZ(II) phase reported by Oyama *et al*. The structure of the grain whose composition is close to $Ba_3Zr_3YO_{3-\delta}$ was confirmed to be close to cubic pervskite by electron diffraction patterns of TEM. When $X_{YO1.5}$ = 0.351 (sample D) and 0.402 (sample N), cubic barium zirconate phase ($BaZrO_3$(ss)), yttria phase and unknown phase were detected. But, we could not find two kinds of grains of barium zirconate phase by EDX analysis like sample C as shown in Fig. 4.10 (d) and (c). This might be because grains in sample D and N were so fine that it was difficult to analyze the composition of each grain by EDX analysis. We consider that equilibrium phases were obtained by the heat-treatment at 1500 °C for 100 hours because the powder synthesized at 500 °C for 10 hours in vacuum from the powder mixed by nitrate freeze-drying method is very fine. Thus, another barium zirconate phase, whose composition is close to $Ba_3Zr_3YO_{3-\delta}$, exists at 1500 °C, and the solubility of yttria into barium zirconate is $X_{YO1.5}$ = 0.02 at 1500 °C.

Table 4.3 Compositions of each grain in samples after heat-treating at 1500 °C for 100 hours by EDX analysis.

	Barium zirconate (Perovskite)			Another new phase (Perovskite)			ZrO_2			Y_2O_3		
	X_{BaO}	X_{ZrO2}	$X_{YO1.5}$	X_{BaO}	X_{ZrO2}	$X_{YO1.5}$	X_{BaO}	X_{ZrO2}	$X_{YO1.5}$	X_{BaO}	X_{ZrO2}	$X_{YO1.5}$
C	0.49	0.49	0.02	0.50	0.39	0.12	0.00	0.50	0.49	(	n.d.	)
D	0.46	0.47	0.06	(	n.d.	)	(	n.d.	)	0.02	0.21	0.77
N	0.45	0.51	0.03	(	n.d.	)	(	n.d.	)	0.02	0.09	0.89

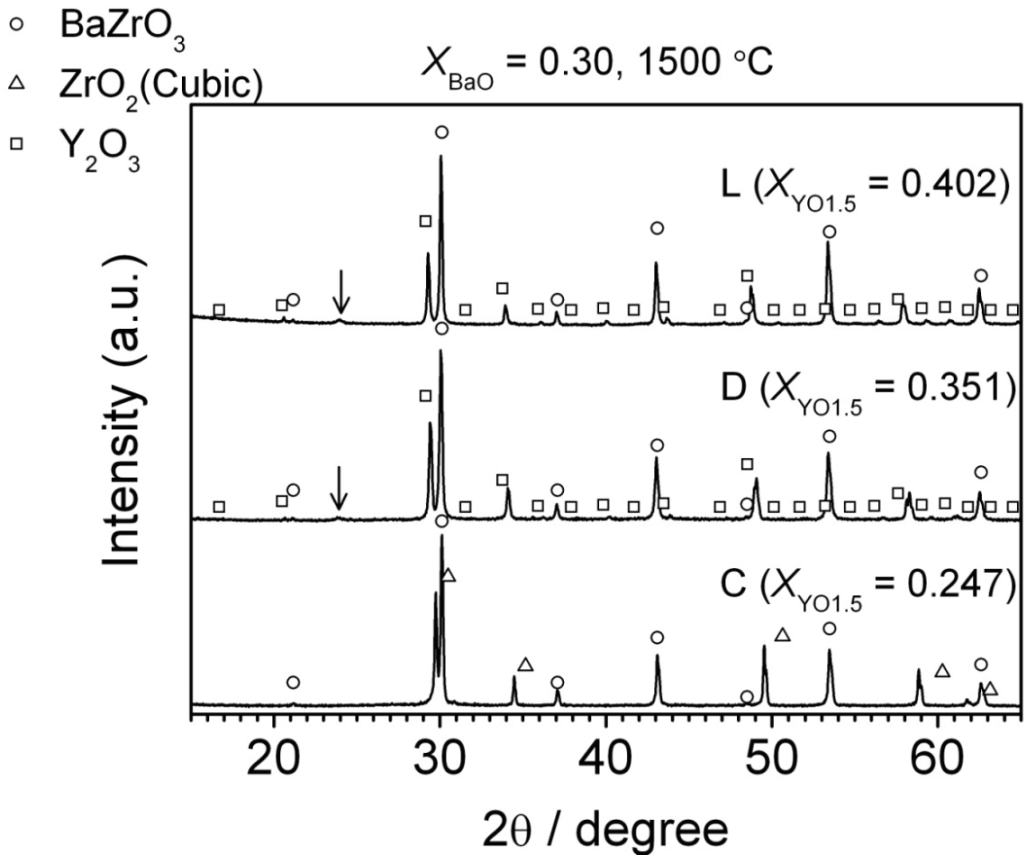

Figure 4.9 XRD patterns of samples at X_{BaO} = 0.30 after heat-treating at 1500 °C for 100 hours ((a) $X_{YO1.5}$ = 0.247, 0.351 and 0.402). Each symbol indicates diffraction patterns of ○ ($BaZrO_3$, JCPDS No. 00-006-0399), △ (ZrO_2, JCPDS No. 00-027-0997), □ (Y_2O_3, JCPDS No. 00-043-1036).

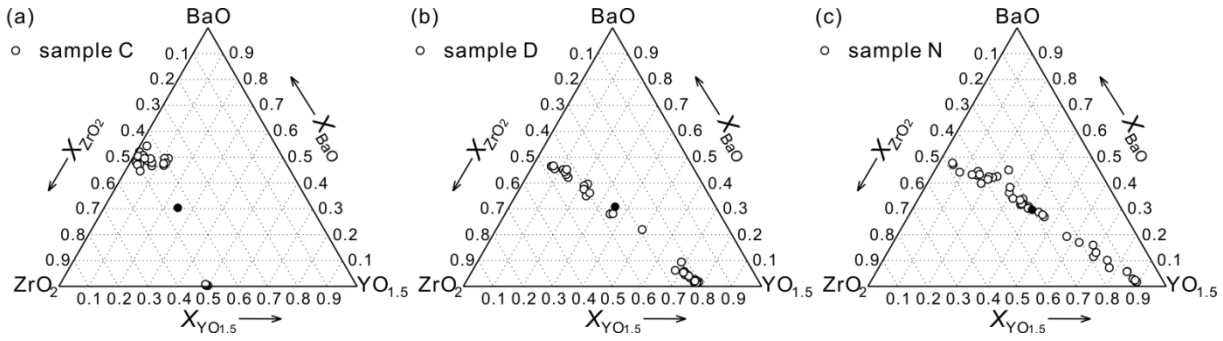

Figure 4.10 Results of EDX analysis in samples after heat-treating at 1500 °C for 100 hours on pseudoternary phase diagrams of BaO-ZrO_2-$MO_{1.5}$ system ((a) sample C, (b) sample D, (c) sample N). Black point is an average composition of each sample.

4.4. Conclusions

A part of the pseudoternary phase diagram in the BaO-ZrO_2-$YO_{1.5}$ system at 1600 °C was established. According to the phase diagram, there is a new phase (BZY424 phase). The composition of BZY424 phase seems to change from ~ 0.31 to ~ 0.40 in X_{BAO}, from ~ 0.16 to ~ 0.25 in X_{ZrO2} and from ~ 0.42 to ~ 0.53 in $X_{YO1.5}$. Diffraction patterns of BZY424 phase is similar to cubic barium zirconate phase ($BaZrO_3$(ss)). Also, the solubility of yttria into cubic barium zirconate is $X_{YO1.5}$ = 0.25 on the composition line where the mole fraction of barium oxide is 0.50 (X_{BaO} = 0.50) at 1600 °C.

There is another new phase whose composition is close to $Ba_3Zr_3YO_{3-\delta}$ at 1500 C and the structure is close to cubic perovskite. Also, the solubility of yttria into cubic barium zirconate is $X_{YO1.5}$ = 0.02 on the composition line where the mole fraction of barium oxide is 0.50 (X_{BaO} = 0.50) at 1500 °C.

References

[63Fan] F.K. Fan, A.K. Kuznetsov, and E.K. Keler, *Bulletin of the Academy of Sciences of the Ussrdivision of Chemical Science*, 4, 542-549 (1963).

[71Rou] A. Rouanet, Revue Internationale des Hautes Temperatures et des Refractaires, **8** [2], 161-180 (1971).

[74Sri] K.K. Srivastava, R.N. Patil, C.B. Choudhary, K.V.G.K. Gokhale, and E.C. Subbarao, *Transactions and Journal of the British Ceramic Society*, **73** [5], 85-91 (1974).

[75Sco] H.G. Scott, *Journal of Materials Scinence*, **10** [9], 1527-1535 (1975).

[76Sha] R. D. Shannon, *Acta Crystallographica Section A*, **32**, 751-767 (1976).

[83Pas] C. Pascual and P. Duran, *Journal of the American Ceramic Society*, **66,** 23-27 (1983).

[87Pas] J.O.A. Paschoal, H. Kleykamp and F. Thümmler, *Journal of Nuclear Materials*, **151**, 10-21 (1987).

[88Stu] V.S. Stubican, *Advances in Applied Ceramics*, **24A**, 71-82 (1988).

[90Rot] R.S. Roth, p 153-168 in *Proceedings of User Aspects of Phase Equilibria*, Petten, June 25-27, (1990).

[91Ses] J. Sestak, J. Kamarad, P. Holba, A. Triska, E. Pollert, and M. Nevriva, *Thermochimica Acta*, **174**, 99-114 (1991).

[91Zha] W. Zhang, K. Osamura, Materials Transactions, **32** [11], 1048-1052 (1991).

[94Hor] I. Horsak, J. Sestak, and B. Stepanek, *Thermochimica Acta*, **234**, 233-243 (1994).

[95Bar] I. Barin, *Thermochemical Data of Pure Substances,* 3rd ed., VCH Verlagsgesellschaft mbH, Weinheim (1995).

[96Mch] J.M. McHale, P. C. McIntyre, K. E. Sickafus, and N. V. Coppa, *Journal of Materials Research*, **11** [5], 1199-1209 (1996).

[96Yas] M. Yashima, M. Kakihana, and M. Yoshimura, *Solid State Ionics*, **86-88**, 1131-1149 (1996).

[06Koj] A. Kojima, K. Tanaka, Y. Oyama, S. Yamaguchi, and T. Higuchi, p 157-158 in *Abstracts of spring meeting for the Mining and Materials Processing Institute of Japan,* Tokyo, Mar. 27-29, (2006).

[08Oya] Y. Oyama, X. Li, S. Miyoshi, and S. Yamaguchi, p 120 in *Abstracts of the 14th International Conference on Solid State Protonic Conductors*, Kyoto, Sep. 7-11, (2008).

Chapter 5

A Pseudoternary Phase Diagram of the BaO-ZrO_2-$ScO_{1.5}$ System at 1600 °C and Solubility of Scandia into Barium Zirconate

5.1 Introduction

Following Chapter 4, we investigated phase relationship of the BaO-ZrO_2-$ScO_{1.5}$ system at 1300 and 1600 °C in order to explain the difference of the sintering behavior between "Y-type" dopant and "Sc-type" dopant.

5.2 Experimental

All samples were synthesized by conventional solid state reaction from barium carbonate ($BaCO_3$: 99.9 %, Wako), zirconia (ZrO_2: 99.97 % including 1.5~2 mass% of hafnia (HfO_2), Daiichi Kigenso) and scandia (99.9 %, Pacific Metals) in the similar way expressed in Chapter 2. We neglected the affect of hafnia on the results for the same reason as described in Chapter 4. Flow charts of synthesis procedures of samples are shown in Fig. 5.1. A powder bed of 90 mass% of scandium-doped barium zirconate and 10 mass% of barium carbonate was used to suppress the vaporization of barium oxide when mole fraction of barium oxide is 0.50 ($X_{BaO} = 0.50$).

The nominal compositions of samples examined in this study are listed in Table 5.1 with results of phase identification by X-ray diffraction analysis (XRD, Rigaku Corporation, RINT2200, Cu-Kα). Figure 5.2 shows the nominal compositions of prepared samples on a pseudoternary phase diagram of the BaO-ZrO_2-$ScO_{1.5}$ system. Chemical analysis and phase identification were carried out using EDX, ICP-AES and XRD.

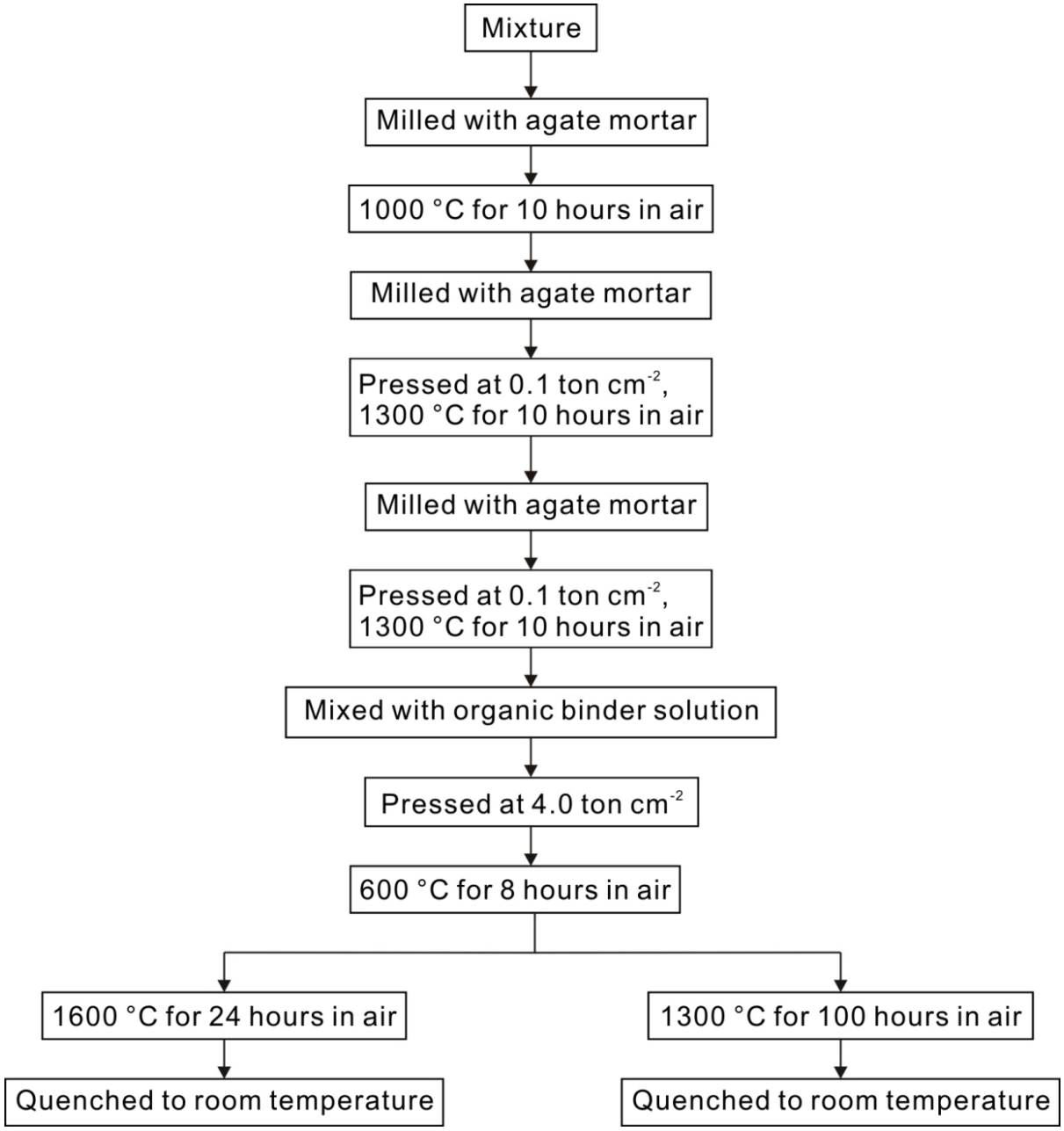

Figure 5.1 Synthesis procedures of samples.

Table 5.1 Nominal compositions of samples and phases identified by X-ray diffraction in samples heat-treatment at 1600 °C for 24 hours in air. ○: detected and ×: undetected.

Sample	Nominal composition			Identified phase by XRD			
	X_{BaO}	X_{ZrO2}	$X_{ScO1.5}$	$BaZrO_3$(ss)	ZrO_2 (cubic)	$ScO_{1.5}$	$Ba_3Sc_4O_9$(ss)
A	0.300	0.650	0.050	○	○	×	×
B	0.300	0.550	0.150	○	○	×	×
C	0.300	0.450	0.250	○	○	○	×
D	0.300	0.350	0.350	○	○	○	×
E	0.300	0.250	0.450	○	×	○	×
F	0.300	0.150	0.550	○	×	○	×
G	0.300	0.050	0.650	○	×	○	×
H	0.500	0.500	0	○	×	×	×
I	0.500	0.400	0.100	○	×	×	×
J	0.500	0.300	0.200	○	×	×	×
K	0.500	0.250	0.250	○	×	×	×
L	0.500	0.200	0.300	○	×	×	○

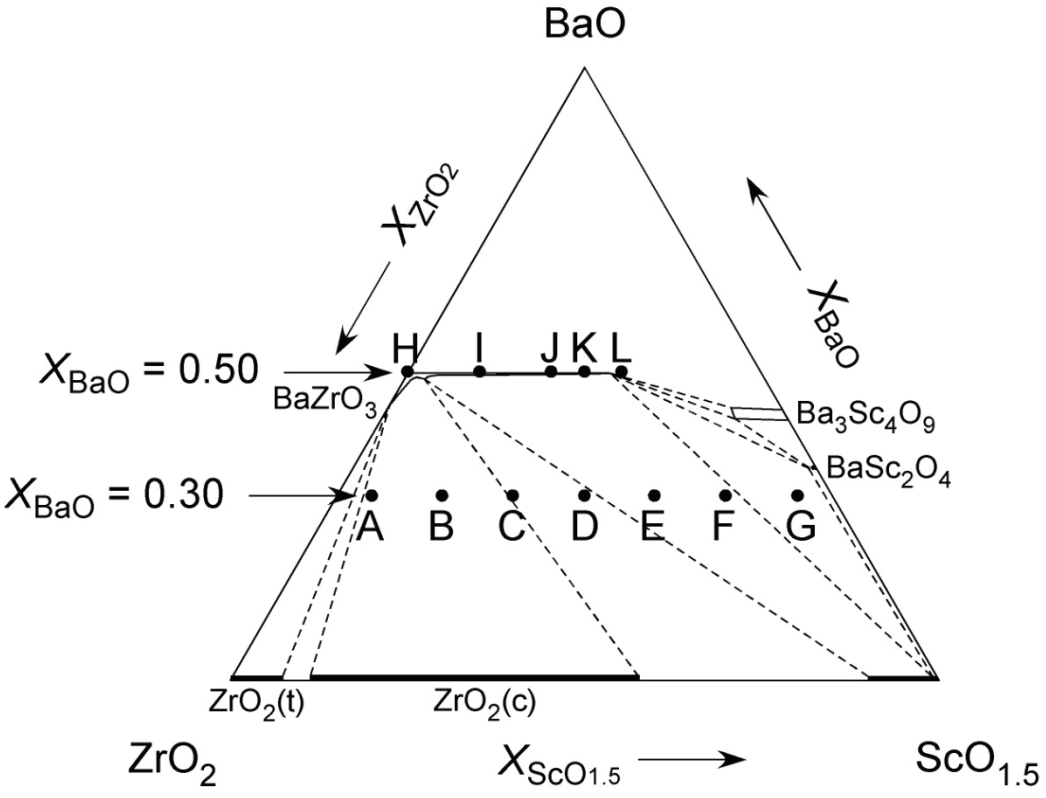

Figure 5.2 Nominal compositions of samples used in this study. Abbreviations of sample names are referred to Table 5.1.

5.3 Results and Discussion

We established the pseudoternary phase diagram of the BaO-ZrO_2-$ScO_{1.5}$ system at 1600 °C as shown in Fig. 5.3. To establish this phase diagram, we combined information of pseudobinary phase diagrams of a BaO-ZrO_2 system[97Pas] and a BaO-$ScO_{1.5}$ system[81Kov], and the solubility of scandia into tetragonal and cubic zirconia phase.[96Yas] There is only one reported phase diagram for the BaO-ZrO_2 system and BaO-$ScO_{1.5}$ system. On the other hand, there are many proposed phase diagrams for a ZrO_2-$ScO_{1.5}$ system.[70Spi,70Tho,87She1,87She2,89Mag, 96Yas,97Ruh] Among these phase diagram, the phase relationship at 1600 °C coincides well and the solubility of scandia into tetragonal and cubic zirconia phase at 1600 °C is almost the same.[70Tho,87She1,87She2,96Yas,97Ruh] We adopted the values from the newest phase diagram of the ZrO_2-$ScO_{1.5}$ system reported by Yashima *et al*.[96Yas]

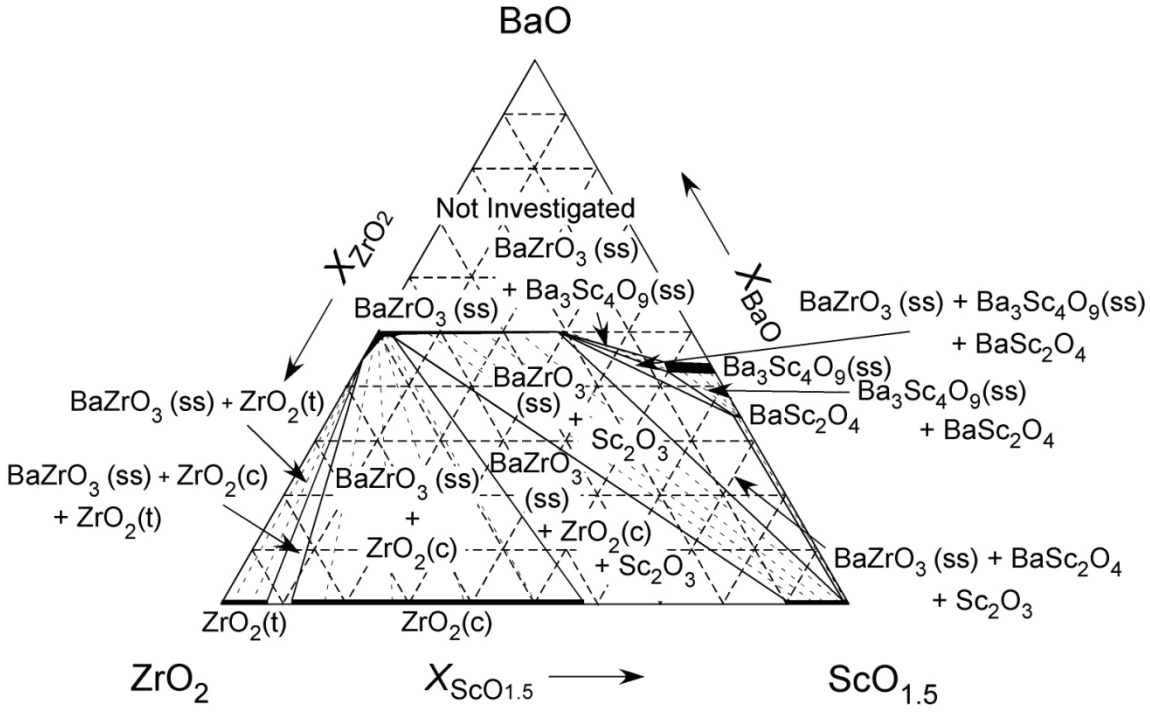

Figure 5.3 Established pseudoternary phase diagram of the BaO-ZrO_2-$ScO_{1.5}$ system at 1600 °C. ZrO_2(t) and ZrO_2(c) denote tetragonal zirconia and cubic zirconia, respectively.

5.3.1 Analysis of X-ray Diffraction of Samples of X_{BaO} = 0.30

Samples on the composition line of X_{BaO} = 0.30 were heat-treated at 1600 °C for 24 hours. XRD patterns of the samples are shown in Fig. 5.4 and the identified phases are summarized in Table 5.1. When the mole fraction of scandia was 0.05 ($X_{ScO1.5}$ = 0.05 (sample A)) and 0.15 ($X_{ScO1.5}$ = 0.15 (sample B)), barium zirconate phase and cubic zirconia phase were identified. When $X_{ScO1.5}$ = 0.25 (sample C) and 0.35 (sample D), barium zirconate phase, scandia phase and cubic zirconia phase were identified. As seen in Fig. 5.4, the peak positions of the cubic zirconia phase in sample B ($X_{ScO1.5}$ = 0.15), sample C ($X_{ScO1.5}$ = 0.25) and sample D ($X_{ScO1.5}$ = 0.35) shifted to higher angles than those of the cubic zirconia phase in JCPDS card [No. 00-027-0997, lattice parameter, a = 0.50900 nm], which is probably due to dissolution of scandia into the cubic zirconia phase. When $X_{ScO1.5}$ = 0.45 (sample E), 0.55 (sample F) and 0.65 (sample G), barium zirconate phase and scandia phase were identified. The intensities of the peaks of the scandia phase increased with increasing mole fraction of scandia.

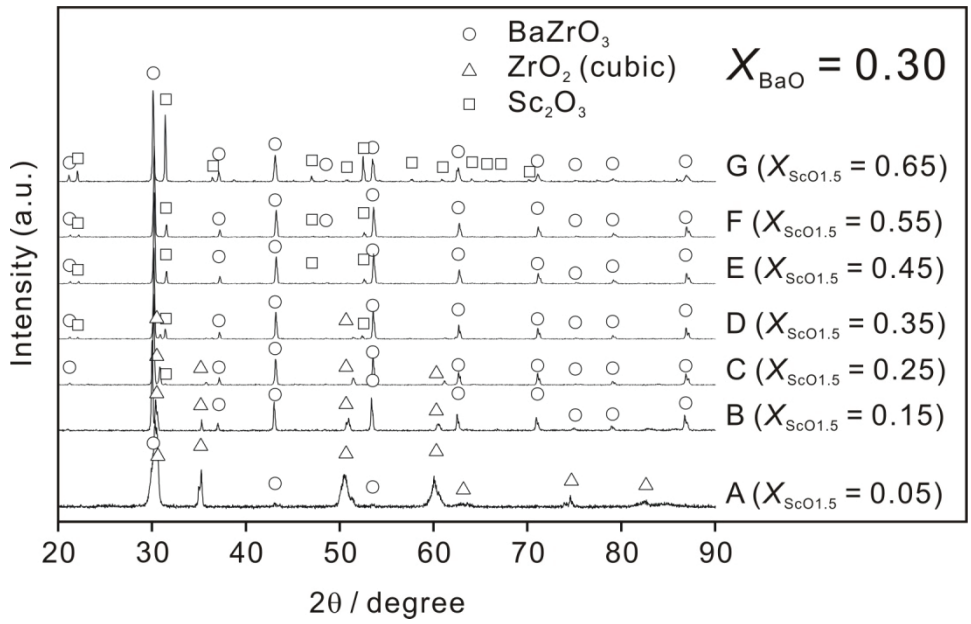

Figure 5.4 XRD patterns of samples of $X_{ScO1.5}$ = 0.05, 0.15, 0.25, 0.35, 0.45, 0.55 and 0.65 at X_{BaO} = 0.30 after heat-treating at 1600 °C for 24 hours.

Table 5.2 Compositions of each phase in samples on the composition line of $X_{BaO} = 0.30$.

	$X_{ScO1.5}$	$BaZrO_3$(ss)			ZrO_2			Sc_2O_3			$BaSc_2O_4$		
		X_{BaO}	X_{ZrO2}	$X_{ScO1.5}$	X_{BaO}	X_{ZrO2}	$X_{ScO1.5}$	X_{BaO}	X_{ZrO2}	$X_{ScO1.5}$	X_{BaO}	X_{ZrO2}	$X_{ScO1.5}$
A	0.05	0.45	0.54	0.00	0.00	0.86	0.14	(	n.d.	)	(	n.d.	)
B	0.15	0.48	0.51	0.01	0.00	0.59	0.41	(	n.d.	)	(	n.d.	)
C	0.25	0.50	0.49	0.01	0.00	0.41	0.59	0.00	0.10	0.89	(	n.d.	)
D	0.35	0.49	0.48	0.03	0.00	0.48	0.51	0.00	0.10	0.90	(	n.d.	)
E	0.45	0.50	0.40	0.11	(	n.d.	)	0.01	0.01	0.98	(	n.d.	)
F	0.55	0.50	0.28	0.22	(	n.d.	)	0.00	0.01	0.99	(	n.d.	)
G	0.65	0.50	0.20	0.29	(	n.d.	)	0.01	0.00	0.99	0.35	0.01	0.63

5.3.2 Results of EDX Analysis of Samples of $X_{BaO} = 0.30$

Table 5.2 shows the compositions of each grain in the samples on the composition line of $X_{BaO} = 0.30$. Four types of grains were observed in this study. At $X_{ScO1.5} = 0.65$ (sample G), $BaSc_2O_4$ phase was observed by EDX analysis, although no diffraction pattern corresponding to $BaSc_2O_4$ phase was detected by XRD analysis. To investigate the reason, we synthesized a single phase of $BaSc_2O_4$ and heat-treated at 1300 °C for 100 hours or 1600 °C for 24 hours, and then quenched to room temperature. Figure 5.5 shows XRD patterns of $BaSc_2O_4$ at 1300 °C and 1600 °C. The XRD pattern of $BaSc_2O_4$ phase at 1600 °C is completely different from that at 1300 °C and the XRD pattern of $BaSc_2O_4$ phase at 1600 °C does not coincide with that in JCPDS card [No.00-044-0259, lattice parameter, a = 0.98341 nm, b = 0.58159 nm, c = 2.0578 nm]. In contrast, the XRD pattern of $BaSc_2O_4$ phase at 1600 °C is quite similar to that of scandia phase [JCPDS No. 00-005-0629, C-type rare earth structure]. We are assuming that the high temperature structure of $BaSc_2O_4$ is an isostructure with C-type rare earth structure, and there is a phase transition of $BaSc_2O_4$ between 1300 and 1600 °C.

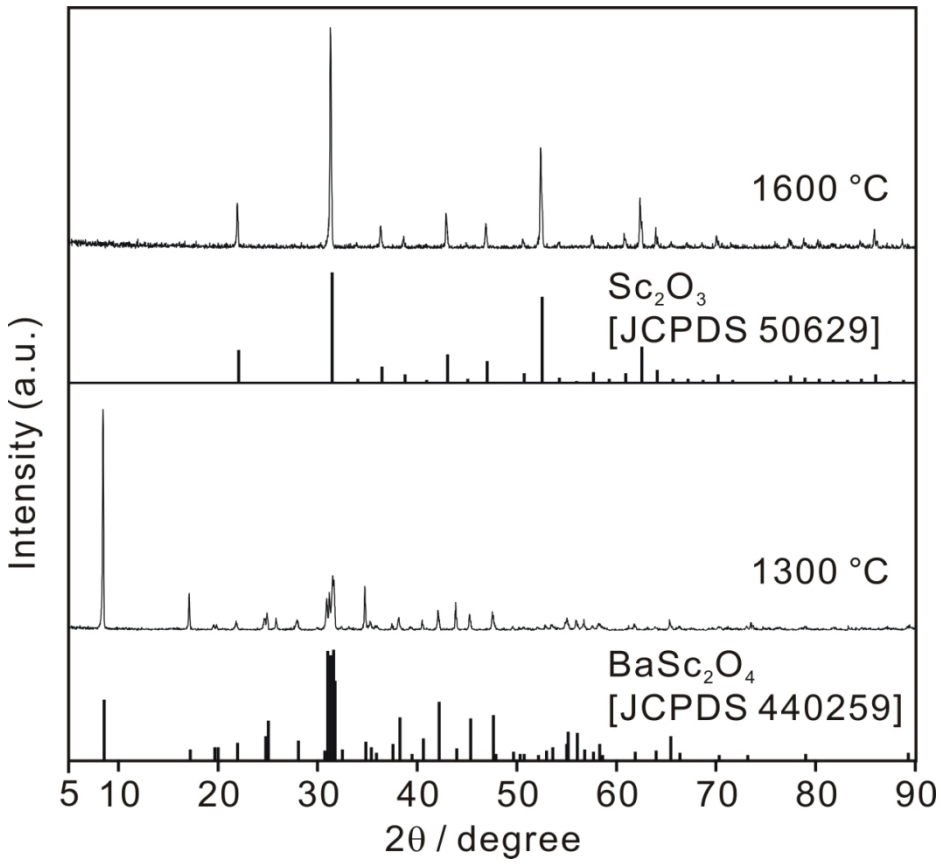

Figure 5.5 XRD patterns of $BaSc_2O_4$ at 1300 °C and 1600 °C.

5.3.3 Analysis of X-ray Diffraction and Results of EDX Analysis of Samples of X_{BaO} = 0.50

Figure 5.6 (a) shows XRD patterns of samples at X_{BaO} = 0.50 which were heat-treated at 1600 °C for 24 hours, and the identified phases are summarized in Table 5.1. When the mole fraction of scandia was from $X_{ScO1.5}$ = 0 to 0.25 (sample H to K), only the barium zirconate phase was only detected. Fig. 5.6 (b) shows lattice parameters of barium zirconate phase in sample H to L as a function of the mole fraction of scandia, $X_{ScO1.5}$. The lattice parameters of the barium zirconate phase increased by doping scandium until between $X_{YO1.5}$ = 0.25 and 0.30 because the ionic radius of scandium ion (Sc^{3+}: 0.0745 nm[76Sha]) is larger than that of zirconium ion (Zr^{4+}: 0.072 nm[76Sha]) and scandium ions are doped into zirconium sites. The lattice parameter of sample L ($X_{YO1.5}$ = 0.30) was smaller than any other samples.

This might be because other barium zirconate phase exists at temperatures lower than 1600 °C like yttrium-doped barium zirconate described in Chapter 4 and it precipitated during cooling. Also, by EDX analysis, it was confirmed that all grains of the barium zirconate phase in the samples from $X_{ScO1.5}$ = 0 to 0.25 (sample H to K) had the same compositions as the average compositions of each sample. At $X_{ScO1.5}$ = 0.30 (sample L), peak patterns of barium zirconate phase and $Ba_3Sc_4O_9$ phase were identified by XRD analysis. The mole fraction of scandia in the barium zirconate phase of the sample at $X_{ScO1.5}$ = 0.30 (sample L) was 0.29 by EDX analysis. Thus, the solubility of scandia into barium zirconate at X_{BaO} = 0.50 is determined to be $X_{ScO1.5}$ = 0.29 at 1600 °C. At $X_{ScO1.5}$ = 0.30 (sample L), the peak positions of the $Ba_3Sc_4O_9$ phase shifted to higher angles than those of the $Ba_3Sc_4O_9$ phase in the JCPDS card [No. 00-031-0161, lattice parameter, a = 0.57989 nm, c =2.3671 nm] (see Fig. 5.7 (b)). Thus, it is assumed that $Ba_3Sc_4O_9$ has some solubility of zirconia.

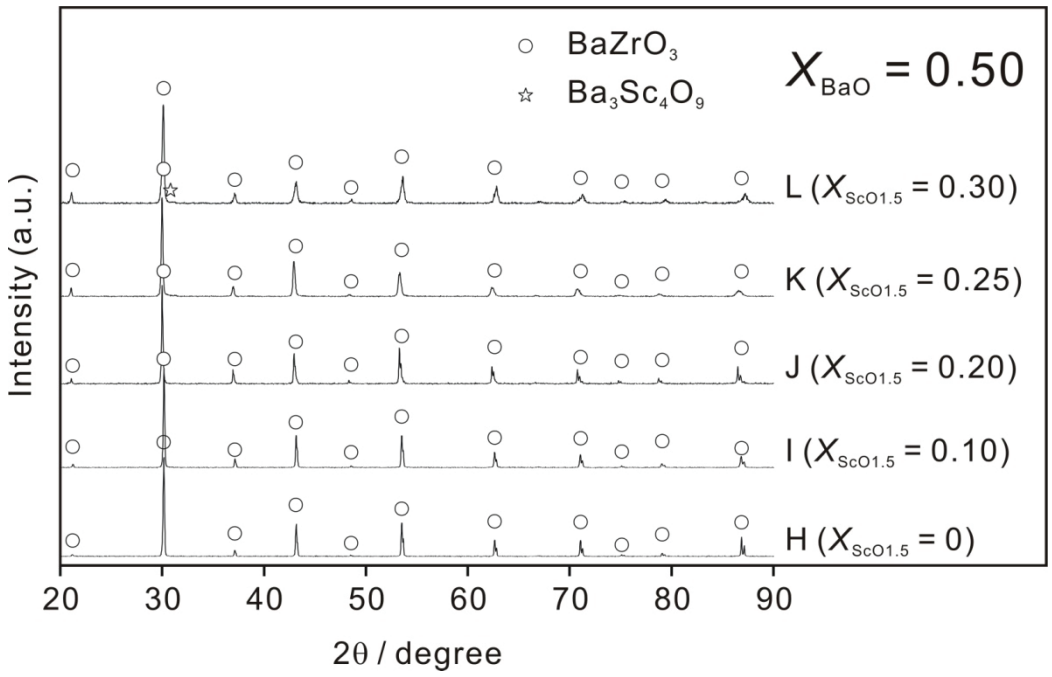

Figure 5.6 (a) XRD patterns of $X_{ScO1.5}$ = 0, 0.10, 0.20, 0.25 and 0.30 at X_{BaO} = 0.50 after heat-treating at 1600 °C for 24 hours.

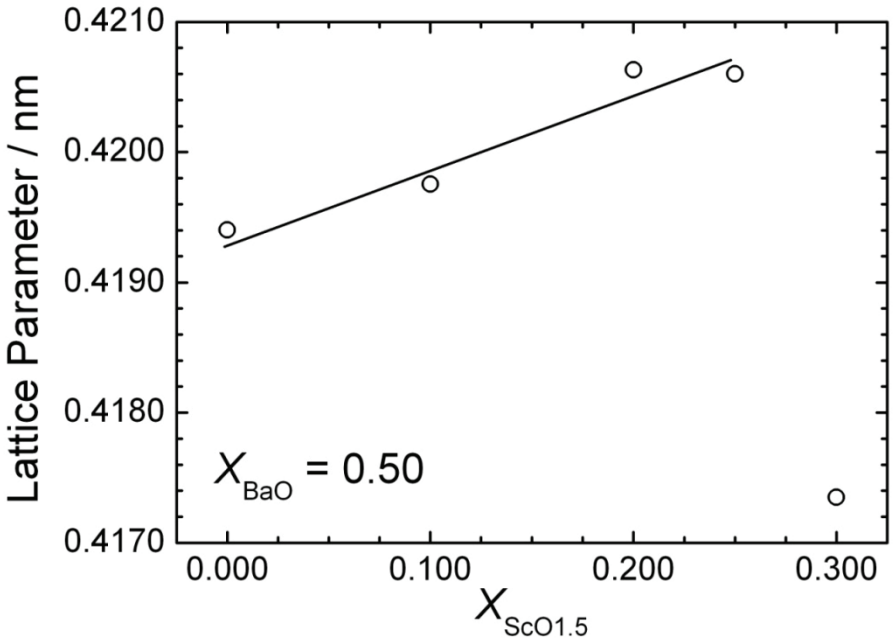

Figure 5.6 (b) Lattice parameters of barium zirconate phase as a function of the mole fraction of scandia, $X_{ScO1.5}$.

5.3.4 Solubility of Scandia into Barium Zirconate at 1300 °C

We examined the solubility of scandia into barium zirconate at temperatures lower than 1600 °C. Samples were heat-treated at 1300 °C for 100 hours in air. Figure 5.7 (a) shows XRD patterns of samples at X_{BaO} = 0.50 which were heat-treated at 1300 °C for 100 hours, and the identified phases are summarized in Table 5.3.

Barium zirconate phase was only detected at $X_{ScO1.5}$ = 0. Barium zirconate phase and scandia phase were identified when $X_{ScO1.5}$ = 0.10. When heat-treated at 1300 °C, samples were not covered with a powder bed of scandium-doped barium zirconate and barium carbonate. Thus, we assumed that a small part of the barium oxide vaporized from the surface of the sample and that the composition of the sample moved to a two phase region of barium zirconate phase and scandia phase. In fact, the negative deviation from the average composition of barium oxide at $X_{ScO1.5}$ = 0.10 was confirmed by ICP-AES (X_{BaO} = 0.488, X_{ZrO2} = 0.423 and $X_{ScO1.5}$ = 0.090). Thus, we assume that the solubility of scandia is more than $X_{ScO1.5}$ = 0.10. When $X_{ScO1.5}$ = 0.20 and 0.30, barium zirconate phase and $Ba_3Sc_4O_9$ phase were

identified. When $X_{ScO1.5}$ = 0.25, barium zirconate phase, scandia phase and $Ba_3Sc_4O_9$ phase were identified. This might be due to the same reason as when $X_{ScO1.5}$ = 0.10 and the composition at $X_{ScO1.5}$ = 0.25 was X_{BaO} = 0.474, X_{ZrO2} = 0.273 and $X_{ScO1.5}$ = 0.253 by ICP-AES. $Ba_3Sc_4O_9$ phase was not detected at $X_{ScO1.5}$ = 0.10. Therefore, the solubility of scandia into barium zirconate at X_{BaO} = 0.50 at 1300 °C is estimated to be between $X_{ScO1.5}$ = 0.10 and 0.20. In addition, the peak positions of the $Ba_3Sc_4O_9$ phase did not shift at all. Thus, we can assume that $Ba_3Sc_4O_9$ has very small solubility of zirconia at 1300 °C.

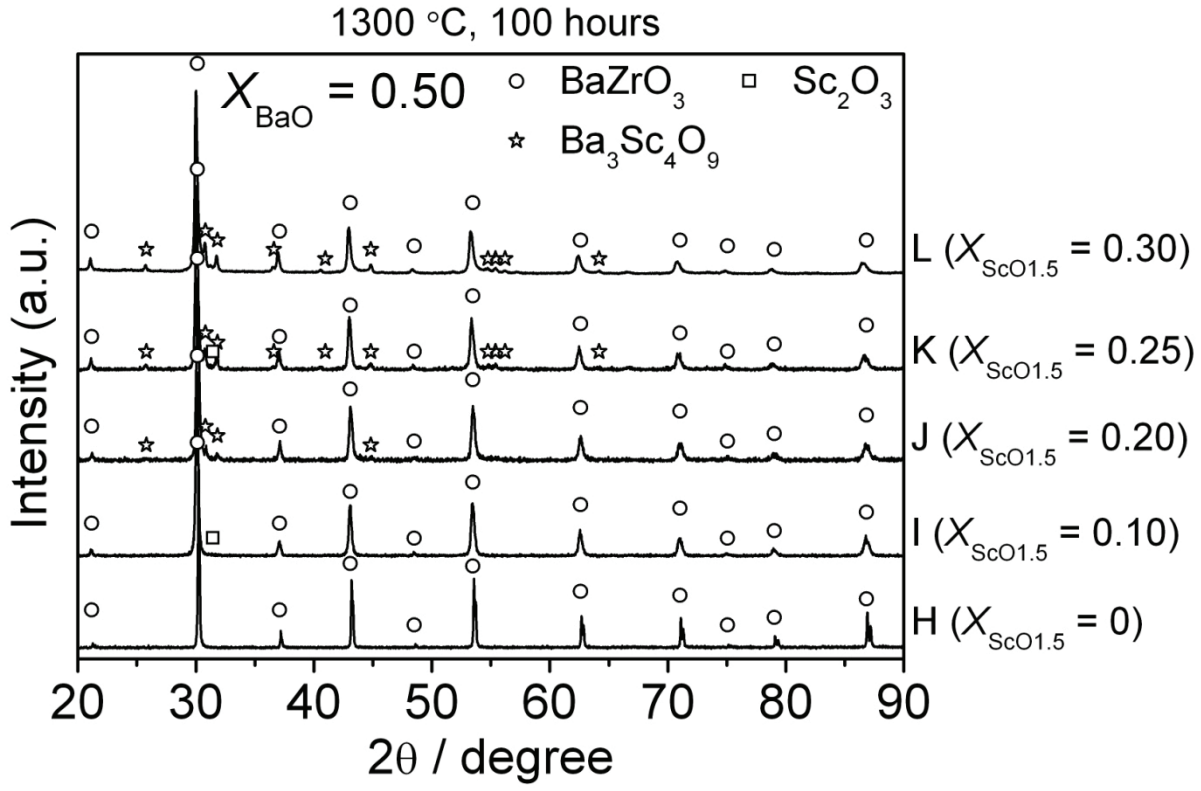

Figure 5.7(a) XRD patterns of $X_{ScO1.5}$ = 0, 0.10, 0.20, 0.25 and 0.30 at X_{BaO} = 0.50 after heat-treating at 1300 °C for 100 hours.

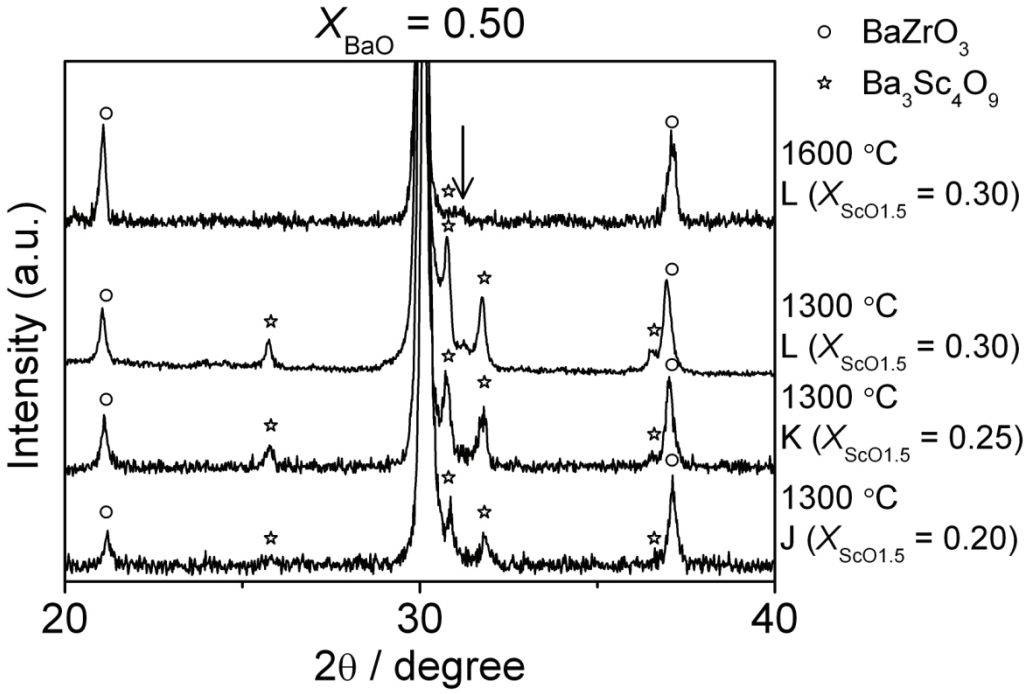

Figure 5.7 (b) XRD patterns of $X_{ScO1.5}$ = 0.20, 0.25 and 0.30 at X_{BaO} = 0.50 after heat-treating at 1300 °C for 100 hours with sample of $X_{ScO1.5}$ = 0.25 at X_{BaO} = 0.50 after heat-treating at 1600 °C for 24 hours.

Table 5.3 Phases identified by XRD in the samples on the composition line of X_{BaO} = 0.50 after heat-treatment at 1300 °C and 1600 °C.

Nominal composition			Heat-treated Condition		
X_{BaO}	X_{ZrO2}	$X_{ScO1.5}$	1300 °C × 100 h	1600 °C × 24 h	As synthesized at 1300 °C
0.500	0.500	0	$BaZrO_3$	$BaZrO_3$	$BaZrO_3$
0.500	0.400	0.100	$BaZrO_3$(ss) + Sc_2O_3	$BaZrO_3$(ss)	$BaZrO_3$(ss)
0.500	0.300	0.200	$BaZrO_3$(ss) + $Ba_3Sc_4O_9$(ss)	$BaZrO_3$(ss)	$BaZrO_3$(ss) + $Ba_3Sc_4O_9$(ss)
0.500	0.250	0.250	$BaZrO_3$(ss) + $Ba_3Sc_4O_9$(ss) + Sc_2O_3	$BaZrO_3$(ss)	$BaZrO_3$(ss) + $Ba_3Sc_4O_9$(ss)
0.500	0.200	0.300	$BaZrO_3$(ss) + $Ba_3Sc_4O_9$(ss)	$BaZrO_3$(ss) + $Ba_3Sc_4O_9$(ss)	$BaZrO_3$(ss) + $Ba_3Sc_4O_9$(ss)

5.4. Conclusions

The results obtained in this work can be summarized as follows:

1) A part of the pseudoternary phase diagram in the BaO-ZrO_2-$ScO_{1.5}$ system at 1600 °C was established. According to the phase diagram, the solubility of scandia into barium zirconate is $X_{ScO1.5}$ = 0.29 on the composition line where the mole fraction of barium oxide is 0.50 (X_{BaO} = 0.50). However, at 1300 °C, the solubility of scandia into barium zirconate is between $X_{ScO1.5}$ = 0.10 and 0.20.
2) Zirconia can dissolve into $Ba_3Sc_4O_9$. However, $Ba_3Sc_4O_9$ does not have such solubility of zirconia at 1300 °C.
3) $BaSc_2O_4$ has a phase transition between 1300 °C and 1600 °C.

References

[70Spi] F. M. Spiridonov, L.N. Popova and R.Y.A. Popil'skii, *Journal of Solid State Chemistry*, **2**, 430-438 (1970).

[70Tho] M. R. Thornber, D . J. M. Bevan and E. Summerville, *Journal of Solid State Chemistry*, **1**, 545-553 (1970).

[81Kov] L. M. Kovba, L. N. Lykova, M. V. Paromova and T. A Kalinina, *Doklady Akademii Nauk SSSR*, **260** [4], 924-927 (1981) in Russian.

[87Pas] J.O.A. Paschoal, H. Kleykamp and F. Thümmler, *Journal of Nuclear Materials*, **151**, 10-21 (1987).

[87Sch1] A. V. Shevchenko, I. M. Maister and L. M. Lopato, *Inorganic Materials*, **23**, 1169-1173 (1987).

[87She2] T-S. Sheu, J. Xu and T-Y. Tien, *Journal of the American Ceramic Society*, **76** [8], 2027-2032 (1987).

[89Mag] R.L. Magunov, G.L. Shklyar and V. F. Katridi, *Inorganic Materials*, **25**, 1035-1037 (1989).

[96Yas] M. Yashima, M. Kakihana, and M. Yoshimura, *Solid State Ionics*, **86-88**, 1131-1149 (1996).

[97Ruh] R. Ruh, H. J. Garret, R. F. Domagala and V. A. Patel, *Journal of the American Ceramic Society*, **60** [9-10], 399-403 (1997).

Chapter 6

Sintering Mechanism of Trivalent Cation Doped Barium Zirconate at 1600 °C

6.1 Introduction

As described in previous chapters, there is a big difference of microstructure between "Y-type" dopant doped barium zirconates and "Sc-type" dopant doped barium zirconates which were synthesized by solid state reaction and sintered at 1600 °C for 24 hours. "Y-type" dopant doped barium zirconates have a bimodal microstructure, and "Sc-type" dopant doped barium zirconates have well-grown grains. Also, phase relationship of 15 % yttrium-doped barium zirconate ($BaZr_{0.85}Y_{0.15}O_{3-\delta}$) is different at between the sintering temperature (1600 °C) and synthesizing temperature (1300 °C). On the other hand, phase relationship of 15 % scandium-doped barium zirconate ($BaZr_{0.85}Sc_{0.15}O_{3-\delta}$) does not change at between the sintering temperature and synthesizing temperature. We assumed that these differences of phase relationship between the sintering temperature and synthesizing temperature have an influence on the microstructures of doped barium zirconate, and it is speculated that the bimodal microstructure of "Y-type" dopant doped barium zirconate comes from kinetic reason of cation diffusion. In order to confirm the speculation, we investigated microstructures of $BaZr_{0.85}Y_{0.15}O_{3-\delta}$ and $BaZr_{0.85}Sc_{0.15}O_{3-\delta}$ by changing sintering time.

6.2 Experimental

Crystalline powders of 15 % scandium-doped barium zirconate ($BaZr_{0.85}Sc_{0.15}O_{3-\delta}$) and 15 % yttrium-doped barium zirconate ($BaZr_{0.85}Y_{0.15}O_{3-\delta}$) were synthesized by conventional solid state reaction from barium carbonate ($BaCO_3$: 99.9%, Wako), zirconia (ZrO_2: 97.97% including 2% of hafnium, Tosoh), scandia (Sc_2O_3: 99.99 %, Daiichi kigenso) and yttria (Y_2O_3: 99.9 %, Shin-Etsu Chemical) and the detail is described in Chapter 2.

The density of the sintered pellets was measured by the Archimedes method in ionic liquid. The lattice parameter of the sintered pellets was determined by XRD. Microstructures of the sintered pellets were observed by SEM. Compositional analysis of grains in the sintered pellets was carried out using EDX.

6.3 Results and Discussion

6.3.1 Microstructure of $BaZr_{0.85}Y_{0.15}O_{3-\delta}$ Sintered for 24 Hours

Figure 6.1 shows the cross-sectional microstructure of 15 % yttrium-doped barium zirconate ($BaZr_{0.85}Y_{0.15}O_{3-\delta}$) after sintering at 1600°C for 24 hours in oxygen. Fig. 6.1 (a) shows a cross sectional image of the sintered pellet at low magnification; the right edge corresponds to the surface of the pellet. Well-grown grains were observed only near the surface of the pellet (see Fig. 6.1 (b)) and phase separation of yttrium-doped barium zirconate was not observed by EDX analysis. On the other hand, grains did not grow well inside the pellet, and two different grains which had different composition were observed as described in Chapter 3 (see Fig. 6.1 (c)). The bed powder (90 mass % of $BaZr_{0.85}Y_{0.15}O_{3-\delta}$ and 10 mass % of $BaCO_3$) has a BaO-rich composition, and a liquid phase exists in the BaO-rich region at 1600 °C as reported by Paschoal *et al.*[87Pas] and Kojima *et al*.[06Koj] Therefore, grains near the surface of the pellet grow easily by formation of the liquid phase, and achieve equilibrium at 1600 °C in short time.

From the discussion above, it is expected to obtain well-grown grains of yttrium-doped barium zirconate by increasing the nominal composition of barium oxide from the stoichiometric composition because of formation of a liquid phase. Thus, we sintered a pellet whose nominal composition was $X_{BaO} = 0.504$, $X_{ZrO2} = 0.421$, $X_{YO1.5} = 0.074$. Fig. 6.2 (a) shows the cross-sectional microstructure of the pellet after sintering at 1600 °C for 24 hours. Well-grown grains were observed inside the pellet. According to EDX analysis of the pellet, a

trace of BaO-rich liquid phase was detected inside the pellet. Unfortunately, the pellet was pulverized after being held in a wet argon atmosphere at 600 °C for several hours (see Fig. 6.2 (b)). This phenomenon might be related to the formation of barium hydroxide from the solidified phase of the BaO-rich liquid phase. Thus, it is difficult for BaO-rich yttrium-doped barium zirconate to be used as a practical electrolyte for fuel cells. On the other hand, pellets of $BaZr_{0.85}Y_{0.15}O_{3-\delta}$ and $BaZr_{0.85}Sc_{0.15}O_{3-\delta}$ sintered for 24 hours without any extra BaO were not pulverized after being held in a wet argon atmosphere at 600 °C for 15 hours or wet hydrogen atmosphere at 600 °C for several hours.

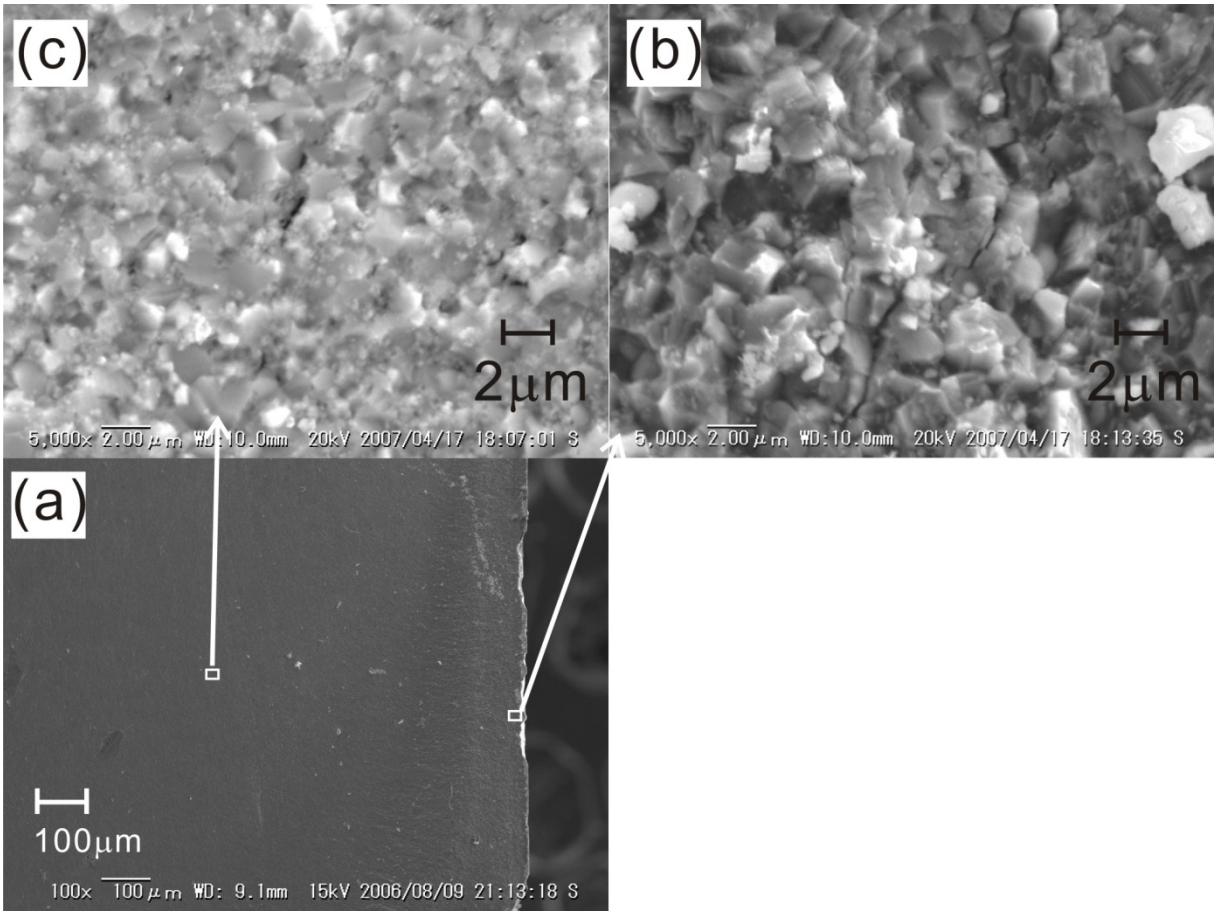

Figure 6.1 Cross-sectional SEM image of $BaZr_{0.85}Y_{0.15}O_{3-\delta}$ sintered for 24 hours at 1600 °C. (a) low magnification, (b) surface, (c) inside.

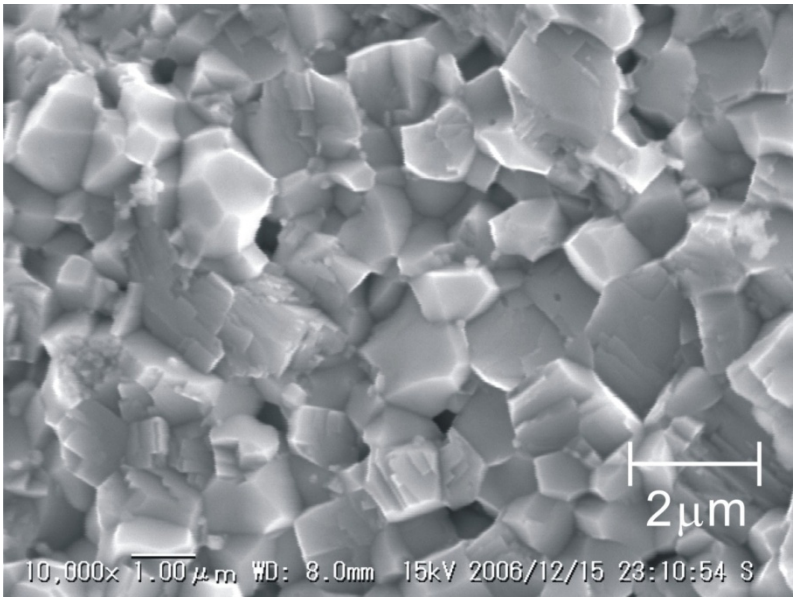

Figure 6.2 (a) Cross-sectional SEM image of BaO-rich yttrium-doped barium zirconate sintered for 24 hours at 1600 °C.

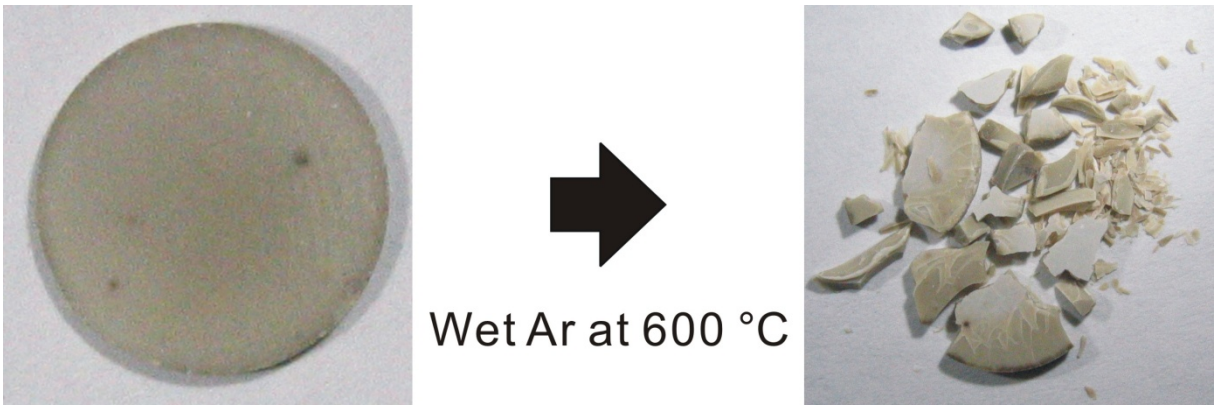

Figure 6.2 (b) Pictures of pellet of BaO-rich yttrium-doped barium zirconate before and after in an argon atmosphere at 600 °C.

6.3.2 Microstructures of $BaZr_{0.85}Y_{0.15}O_{3-\delta}$ and $BaZr_{0.85}Sc_{0.15}O_{3-\delta}$ in Different Sintering Time

Figure 6.3 shows the variations of the relative density of 15 % scandium-doped barium zirconate ($BaZr_{0.85}Sc_{0.15}O_{3-\delta}$) and $BaZr_{0.85}Y_{0.15}O_{3-\delta}$ with sintering time. Relative density was calculated against theoretical density, which was calculated with lattice parameters determined by XRD analysis. The relative density at time zero is that of pellets

before sintering at 1600 °C. As seen in the figure, the relative density of $BaZr_{0.85}Sc_{0.15}O_{3-\delta}$ becomes larger than 98 % after sintering for 24 hours. The relative density of $BaZr_{0.85}Y_{0.15}O_{3-\delta}$ also reached 98 % after sintering for 8 hours. Considering the difference of relative density at time zero, there is not a big difference in the compacting process between yttrium-doped barium zirconate and scandium-doped barium zirconate.

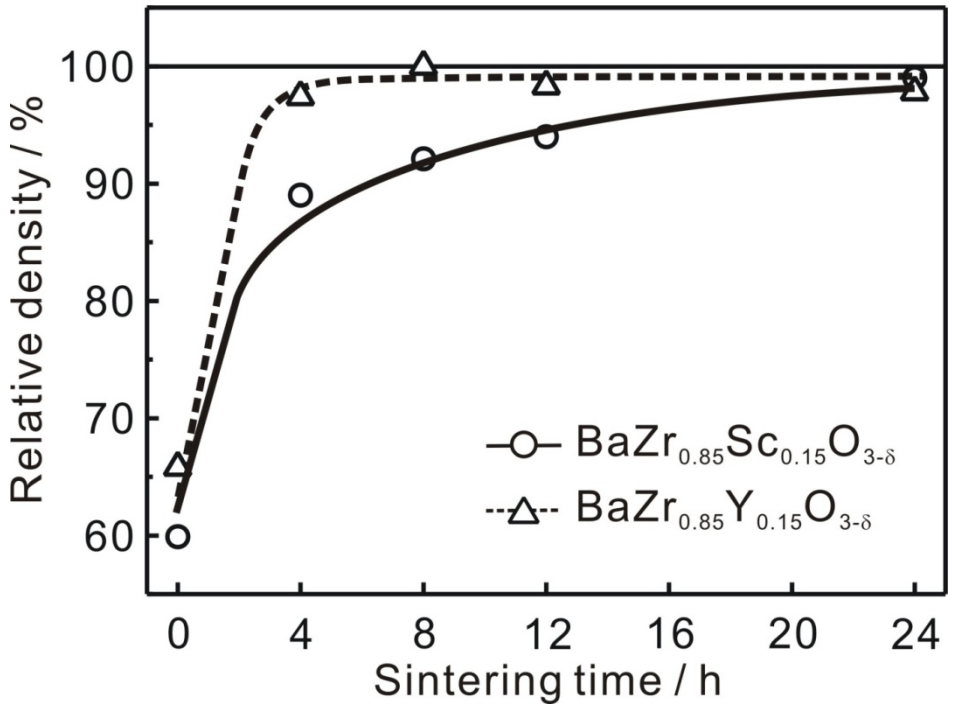

Figure 6.3 Relative density of $BaZr_{0.85}Sc_{0.15}O_{3-\delta}$ and $BaZr_{0.85}Sc_{0.15}O_{3-\delta}$ as a function of sintering time.

Figure 6.4 shows cross-sectional microstructures of $BaZr_{0.85}Sc_{0.15}O_{3-\delta}$ and $BaZr_{0.85}Y_{0.15}O_{3-\delta}$ sintered at 1600 °C for 0, 4, 8, 24 and 100 hours. The grains of $BaZr_{0.85}Sc_{0.15}O_{3-\delta}$ did not grow obviously for 4 and 8 hours, but the grains of $BaZr_{0.85}Sc_{0.15}O_{3-\delta}$ grew well when the sintering time was longer than 24 hours. The average grain sizes of $BaZr_{0.85}Sc_{0.15}O_{3-\delta}$ sintered for 24 and 100 hours were about 0.68 μm and 0.77 μm, respectively; therefore, 24 hours is sufficient sintering time for $BaZr_{0.85}Sc_{0.15}O_{3-\delta}$ to have

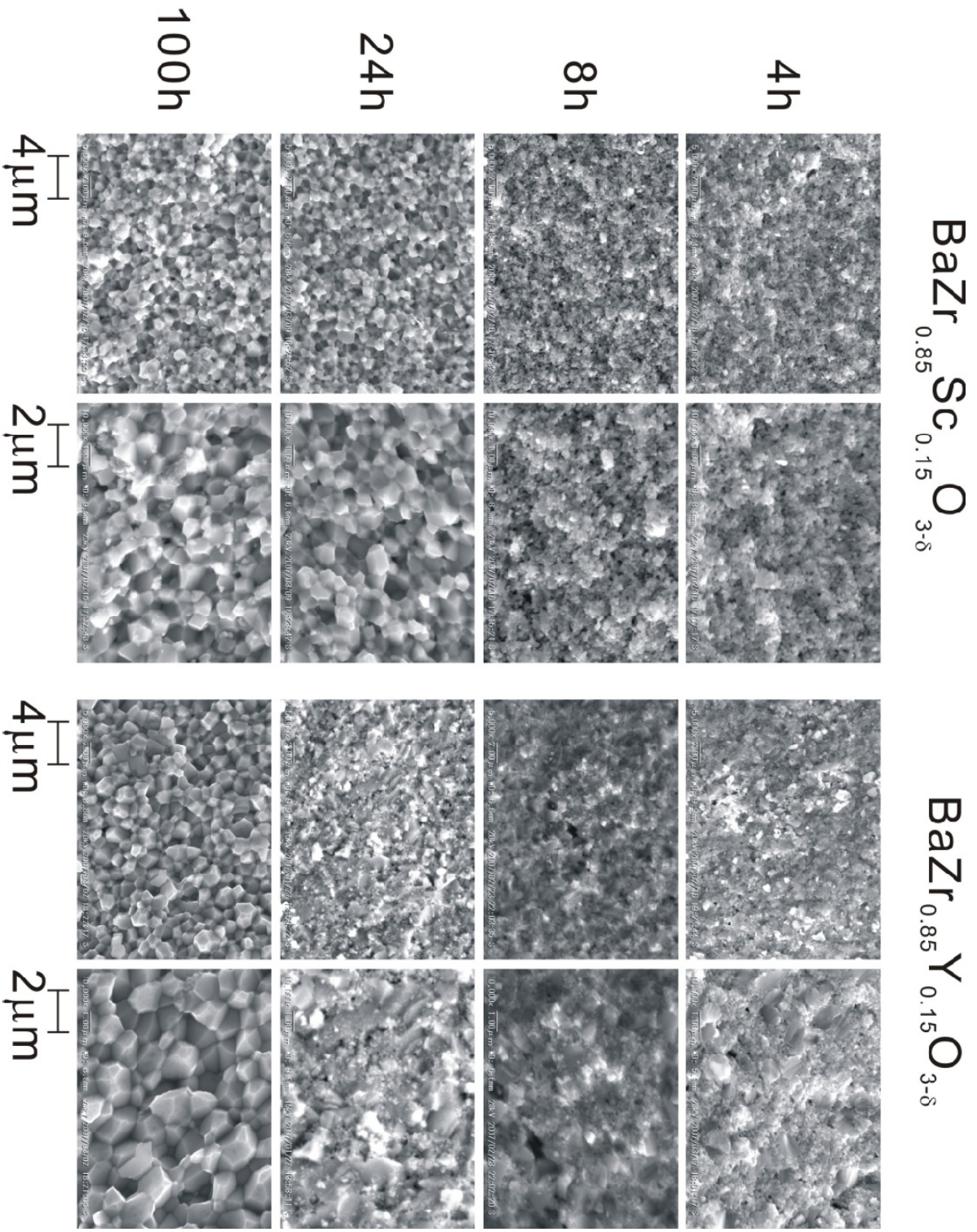

Figure 6.4 Cross-sectional SEM image of $BaZr_{0.85}Sc_{0.15}O_{3-\delta}$ and $BaZr_{0.85}Y_{0.15}O_{3-\delta}$ sintered for 0, 4, 8, 24 and 100 hours at 1600 °C.

large relative density and well-grown grains for the powders synthesized by solid state reaction. Also, if $BaZr_{0.85}Sc_{0.15}O_{3-\delta}$ is single phase, it is empirically know that the relationship between the average grain size, r, and sintering time, t, can be described as $r^2 - r_0^2 = kt$[84Nis], where k and r_0 are constant. Fig. 6.5 shows average square grain sizes of as $BaZr_{0.85}Sc_{0.15}O_{3-\delta}$ sintered in air a function of sintering time. The average square grain size is leaner against sintering time, which means that $BaZr_{0.85}Sc_{0.15}O_{3-\delta}$ is single phase. On the other hand, it took 100 hours to obtain well-grown grains of $BaZr_{0.85}Y_{0.15}O_{3-\delta}$. For $BaZr_{0.85}Y_{0.15}O_{3-\delta}$ sintered for 100 hours, obvious phase separation of yttrium-doped barium zirconate was not observed by EDX analysis. This result implies that it takes long time for $BaZr_{0.85}Y_{0.15}O_{3-\delta}$ synthesized by solid state reaction to obtain equilibrium phase at 1600 °C. However, the yttria phase was additionally identified in the pellet after sintering for 100 hours as shown in Figure 6.6. Barium oxide has significantly high vapor pressure at 1600 °C (*ca*, 8×10^{-5} atm[22]); thus, barium oxide is expected to vaporize from the pellet, and then yttria to precipitate over 100 hours.

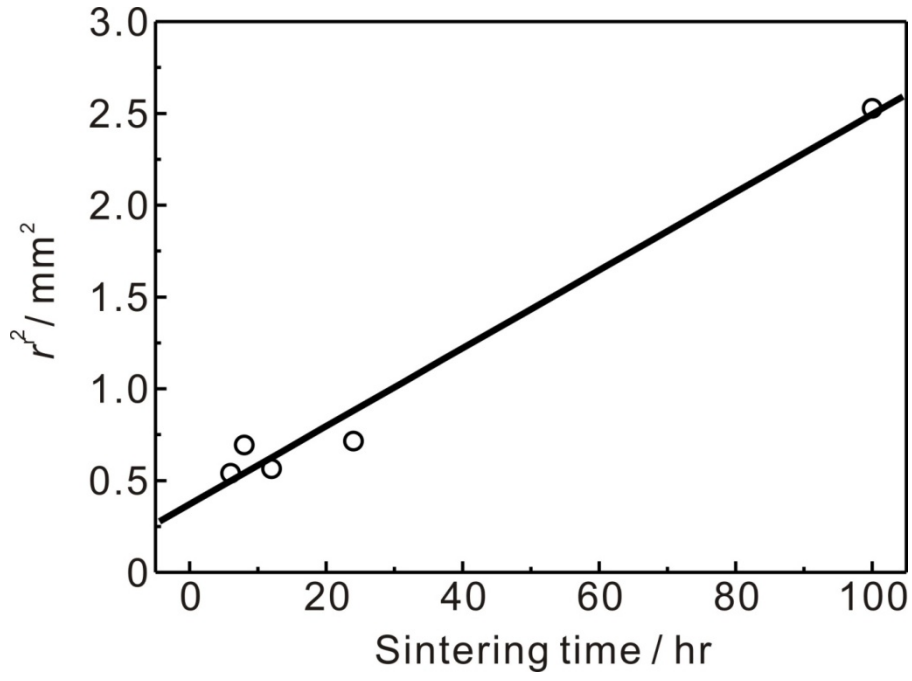

Figure 6.5 Average square grain sizes of as $BaZr_{0.85}Sc_{0.15}O_{3-\delta}$ sintered in air a function of sintering time.

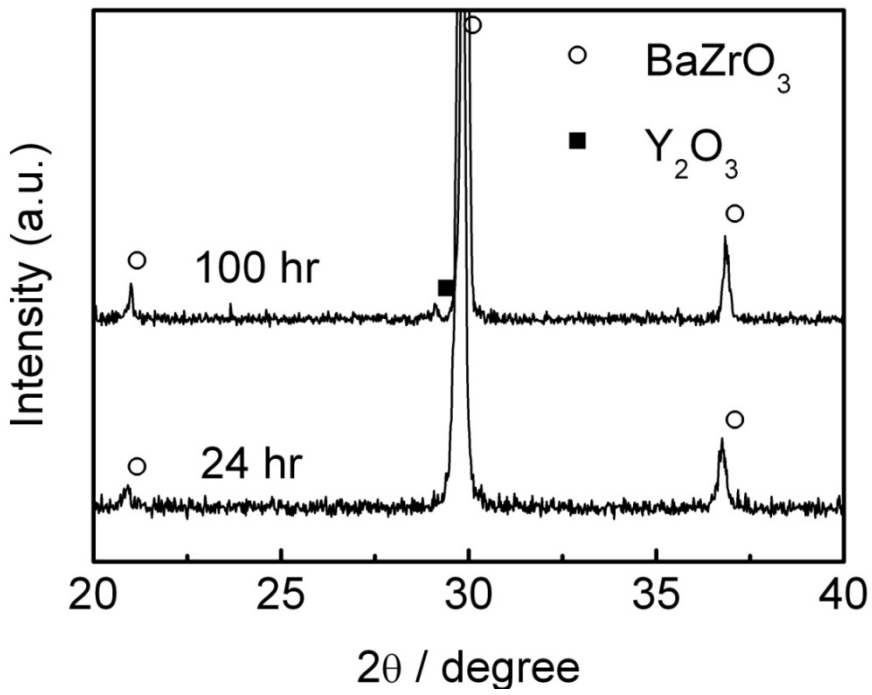

Figure 6.6 XRD patterns of $BaZr_{0.85}Y_{0.15}O_{3-\delta}$ sintered for 24 and 100 hours at 1600 °C. Each symbol indicates diffraction patterns of ○ ($BaZrO_3$, JCPDS No. 00-006-0399) and ■ (Y_2O_3, JCPDS No. 00-043-1036).

In order to confirm that kinetic reason of cation diffusion causes the bimodal structure of $BaZr_{0.85}Y_{0.15}O_{3-\delta}$ sintered for 24 hours from powders synthesized by solid state reaction, $BaZr_{0.85}Y_{0.15}O_{3-\delta}$ pellet was sintered for 24 hours from powders synthesized by nitrate freeze drying method. Grain size of powders synthesized by nitrate freeze drying method is much smaller than that by solid state reaction, which means that the diffusion distance of cation in $BaZr_{0.85}Y_{0.15}O_{3-\delta}$ pellet sintered from powder synthesized by nitrate freeze drying method is much shorter that that by solid state reaction. Fig. 6.7 (a) and (b) show the cross-sectional microstructure of the pellet after etching by hydrogen fluoride (HF) with a pH of 2 and the compositions of grains in the pellet on pseudoternary phase diagrams of $BaO\text{-}ZrO_2\text{-}YO_{1.5}$ system, respectively. Large and homogeneous grains of $BaZr_{0.85}Y_{0.15}O_{3-\delta}$ were obtained by sintering for 24 hours at 1600 °C using powder synthesized by nitrate freeze drying method.

From the results above, it is confirmed that the bimodal microstructure of $BaZr_{0.85}Y_{0.15}O_{3-\delta}$ sintered for 24 hours from powders synthesized by solid state reaction comes from kinetic reason of cation diffusion.

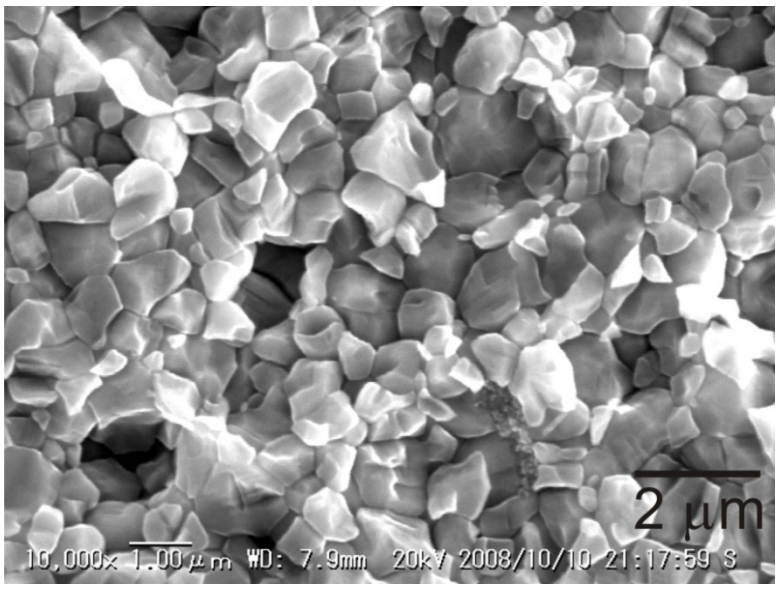

Figure 6.7 (a) Cross-sectional microstructure of $BaZr_{0.85}Y_{0.15}O_{3-\delta}$ pellet sintered for 24 hours from powders synthesized by nitrate freeze drying method after etching by hydrogen fluoride

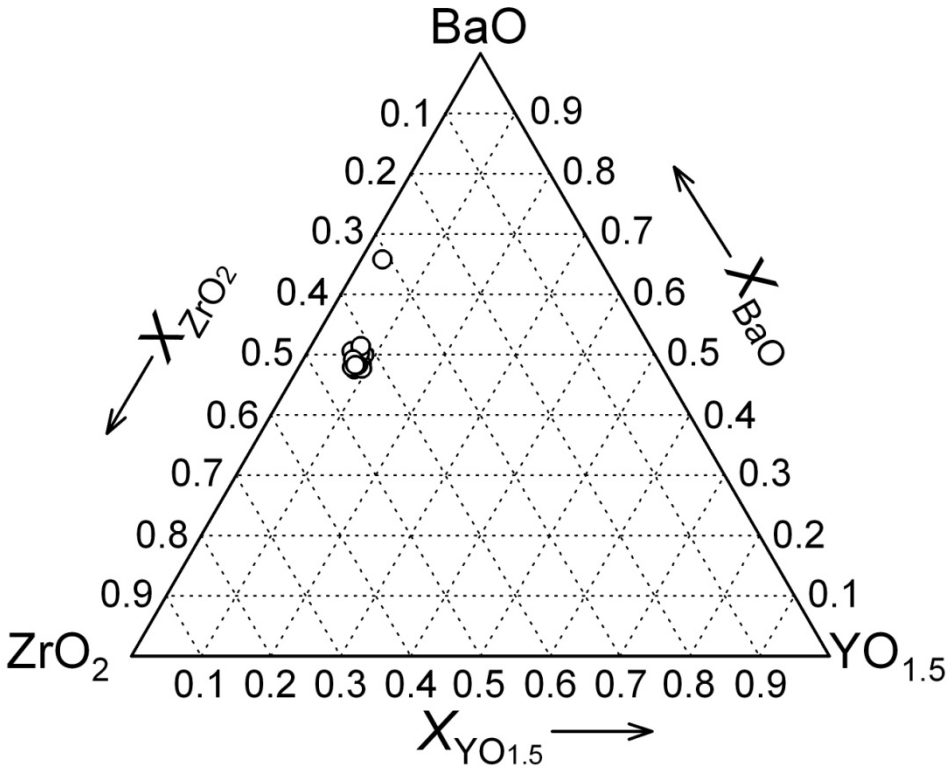

Figure 6.7 (b) The compositions of grains in the pellet on pseudoternary phase diagrams of $BaO\text{-}ZrO_2\text{-}YO_{1.5}$ system.

6.4 Conclusions

We can say that differences of phase relationship between the sintering temperature (1600 °C) and synthesizing temperature (1300 °C) have an influence on the microstructures of doped barium zirconate, especially in case of the sintering at 1600 °C for 24 hours using powders synthesized by solid state reaction. When phase relationship of doped barium zirconates between the sintering temperature and synthesizing temperature is different, the microstructure of the doped barium zirconates is bimodal because of kinetic reason of cation diffusion during sintering ("Y-type" dopant). On the other hand, when doped barium zirconates have the same phase relationship at between the sintering temperature and synthesizing temperature, grains of the doped barium zirconates is large and homogeneous because long-distance diffusion of cations is not needed for grain growth during sintering ("Sc-type" dopant). Even in case of $BaZr_{0.85}Y_{0.15}O_{3-\delta}$, large and homogeneous grains can be obtained by the sintering at 1600 °C for 24 hours using powders synthesized by nitrate freeze drying method. This is because the diffusion distance of cation in the $BaZr_{0.85}Y_{0.15}O_{3-\delta}$ pellet is much shorter.

References

[84Nis] T. Nishizawa, *Tetsu to Hagane,* **70,** 194-202 (1982).

[87Pas] J.O.A. Paschoal, H. Kleykamp and F. Thümmler, *Journal of Nuclear Materials*, **151**, 10-21 (1987).

[06Koj] A. Kojima, K. Tanaka, Y. Oyama, S. Yamaguchi, and T. Higuchi, p 157-158 in *Abstracts of spring meeting for the Mining and Materials Processing Institute of Japan,* Tokyo, Mar. 27-29, (2006).

Chapter 7

Improvement of Grain-boundary Conductivity of Trivalent Cation-doped Barium Zirconate Sintered at 1600 °C by Co-doping Scandium and Yttrium

7.1 Introduction

As described in Chapter 1, it is necessary to have larger grains of yttrium-doped barium zirconate to improve the high grain-boundary resistance. However, it is difficult to obtain well-grown and homogeneous grains of 15 % yttrium-doped barium zirconate because of the difference of phase relationship between the sintering temperature (1600 °C) and a synthesizing temperature (1300 °C) as expressed in Chapter 6. On the other hand, we can obtain large and uniform grains of 15 % scandium-doped barium zirconate easily.

When yttrium and scandium are co-doped into barium zirconate, the phase relationship at 1300 °C might change. In such a case, two scenarios may be envisaged; one is that there is no phase separation at 1300 °C, and the other is that there is still phase separation at 1300 °C. In the former scenario, cations do not need to diffuse for a long distance. Even in the latter scenario, the grain growth rate might be improved because the concentration gap of dopant between two phases of co-doped barium zirconate is expected to be smaller than that of only yttrium-doped barium zirconate. With these backgrounds and ideas, we performed the following experiments in this study:

(1) Observation of microstructures of co-doped barium zirconate.

(2) Measurement of bulk and grain-boundary conductivities of the co-doped barium zirconate.

7.2 Experimental

Crystalline powders of scandium and yttrium co-doped barium zirconate were synthesized by a solid state reaction from barium carbonate ($BaCO_3$: 99.9%, Wako), zirconia

(ZrO_2: 99.97% including 2% of hafnium, 24 nm of grain size, Tosoh), scandia (Sc_2O_3: 99.99%, Daiichi kigenso) and yttria (Y_2O_3: 99.9 %, Shin-Etsu Chemical) and the detail is described in Chapter 2.

Microstructures of the sintered pellets were observed by SEM and TEM, and compositional analysis was carried out using EDX. Density of the sintered pellets was measured by the Archimedes method in ionic liquid. The lattice parameters of the sintered pellets were determined by XRD analysis and the theoretical density was calculated using these lattice parameters.

Conductivity of the sintered pellets was measured by AC 2-terminal method as described in Chapter 2 and 3. The pellets were held at 600 °C for more than 10 hours, and then cooled to 500 °C.

7.3 Results and Discussion

7.3.1 Observation in Microstructures of Co-doped Barium Zirconate

7.3.1.1 SEM and EDX Analysis

The compositions of sintered pellets were $BaZr_{0.85}Sc_{0.15}O_{3-\delta}$ (BZS15), $BaZr_{0.85}Sc_{0.10}Y_{0.05}O_{3-\delta}$ (BZS10Y5), $BaZr_{0.85}Sc_{0.075}Y_{0.075}O_{3-\delta}$ (BZS7.5Y7.5), $BaZr_{0.85}Sc_{0.05}Y_{0.10}O_{3-\delta}$ (BZS5Y10), and $BaZr_{0.85}Y_{0.15}O_{3-\delta}$ (BZY15). All of the pellets had relative densities of more than 97.8 % as seen in Table 7.1, and it was confirmed by XRD analysis that all of the pellets contained only barium zirconate phase. Fig. 7.1 shows cross-sectional SEM images of scandium and yttrium co-doped barium zirconate. The grains of BZS10Y5, BZS7.5Y7.5, and BZS10Y5 were bimodal in size, although the grains of BZS15 were uniform.

According to EDX analysis, BZS15 was confirmed to be completely uniform single phase, and BZY15 had two phases of low yttrium-doped barium zirconate (X_{BaO} = 0.51, X_{ZrO2}

Table 7.1 Compositions, abbreviation, densities, theoretical densities, and relative densities of prepared scandium and yttrium co-doped barium zirconate.

Samples Composition	Abbreviation	Density (g cm^{-3})	Theoretical density (g cm^{-3})	Relative density (%)
$BaZr_{0.85}Sc_{0.15}O_{3-\delta}$	BZS15	6.01	6.07	99.0
$BaZr_{0.85}Sc_{0.10}Y_{0.05}O_{3-\delta}$	BZS10Y5	6.03	6.07	99.3
$BaZr_{0.85}Sc_{0.075}Y_{0.075}O_{3-\delta}$	BZS7.5Y7.5	5.99	6.07	98.6
$BaZr_{0.85}Sc_{0.05}Y_{0.10}O_{3-\delta}$	BZS5Y10	6.06	6.06	98.2
$BaZr_{0.85}Y_{0.15}O_{3-\delta}$	BZY15	5.94	6.08	97.8

= 0.46 and $X_{YO1.5}$ = 0.03) and high yttrium-doped barium zirconate (X_{BaO} = 0.45, X_{ZrO2} = 0.34 and $X_{YO1.5}$ = 0.21) as described in Chapter 6. In co-doped samples (BZS10Y5, BZS7.5Y7.5, BZS5Y10), we did not recognize the apparently phase separation by EDX analysis. Considering the area fraction of fine grains, the average grain size of co-doped barium zirconate seems to be larger than that of BZY15.

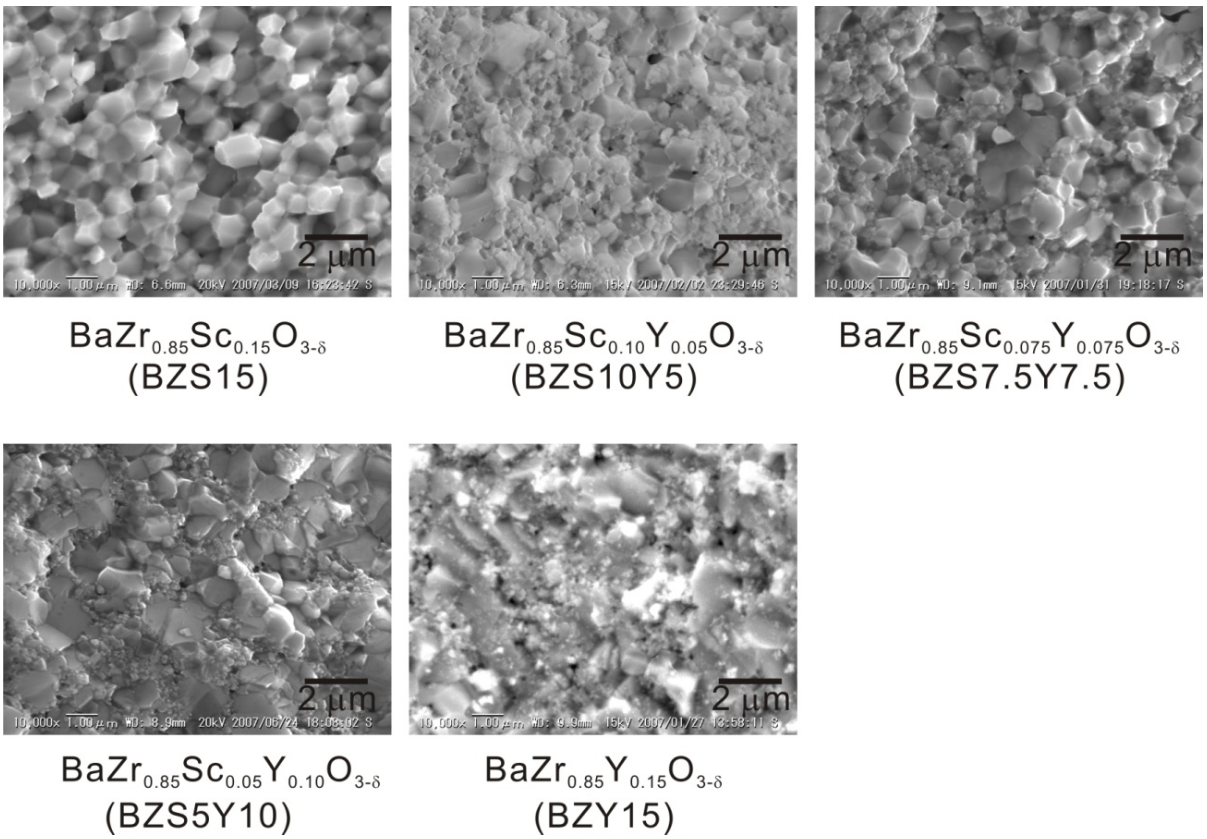

Figure 7.1 Cross-sectional SEM image of scandium and yttrium co-doped barium zirconate.

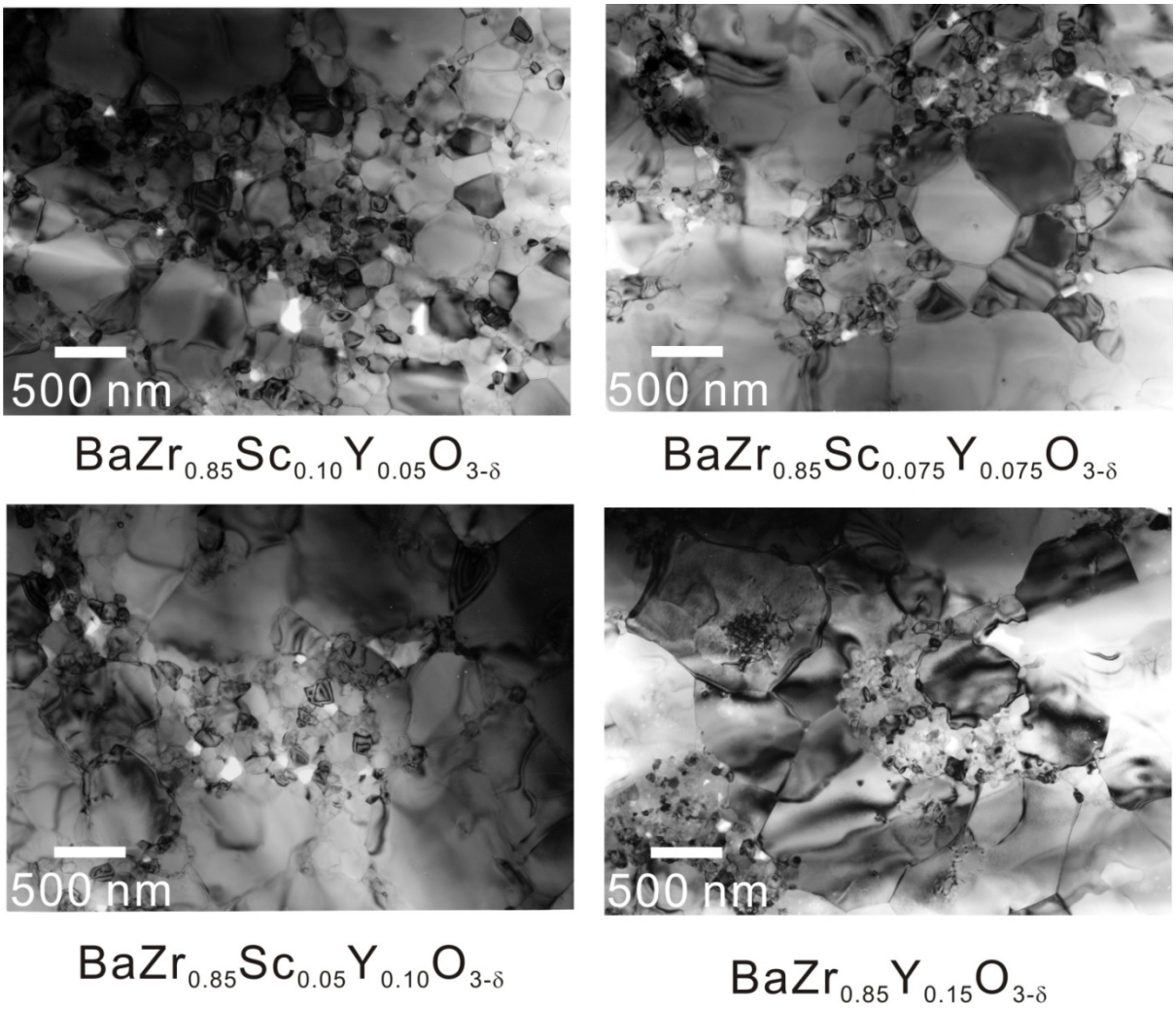

Figure 7.2 Bright-field TEM images of scandium and yttrium co-doped barium zirconate.

7.3.1.2 TEM Observation

TEM observation was carried out to estimate the grain-boundary concentration in co-doped and yttrium-doped barium zirconates. The bright-field TEM images of BZS10Y5, BZS7.5Y7.5, BZS5Y10, and BZY15 are shown in Fig. 7.2. Bimodal microstructure was observed in all of the co-doped and yttrium-doped samples. Fig. 7.3 shows the average size of small grains, r, and the value of three-second power of area fraction of small grains, f, divided by the cube of the average size of small grains as a function of the ratio of mole fraction of scandium to yttrium. The value of $\frac{f^{\frac{3}{2}}}{r^3}$ should be proportional to the grain-boundary concentration because the contribution to the grain-boundary concentration from large grains

can be neglected. The area fraction of small grains was calculated from SEM images (Fig. 7.1). The average size of small grain was calculated from TEM images. But it is noted that the calculated area fraction must be semi-quantitative because it was difficult to estimate the area fraction accurately from the SEM images. Even though large errors are associated, Fig. 7.3 indicates that the concentration of grain-boundary in all co-doped barium zirconates was obviously smaller than that in BZY15.

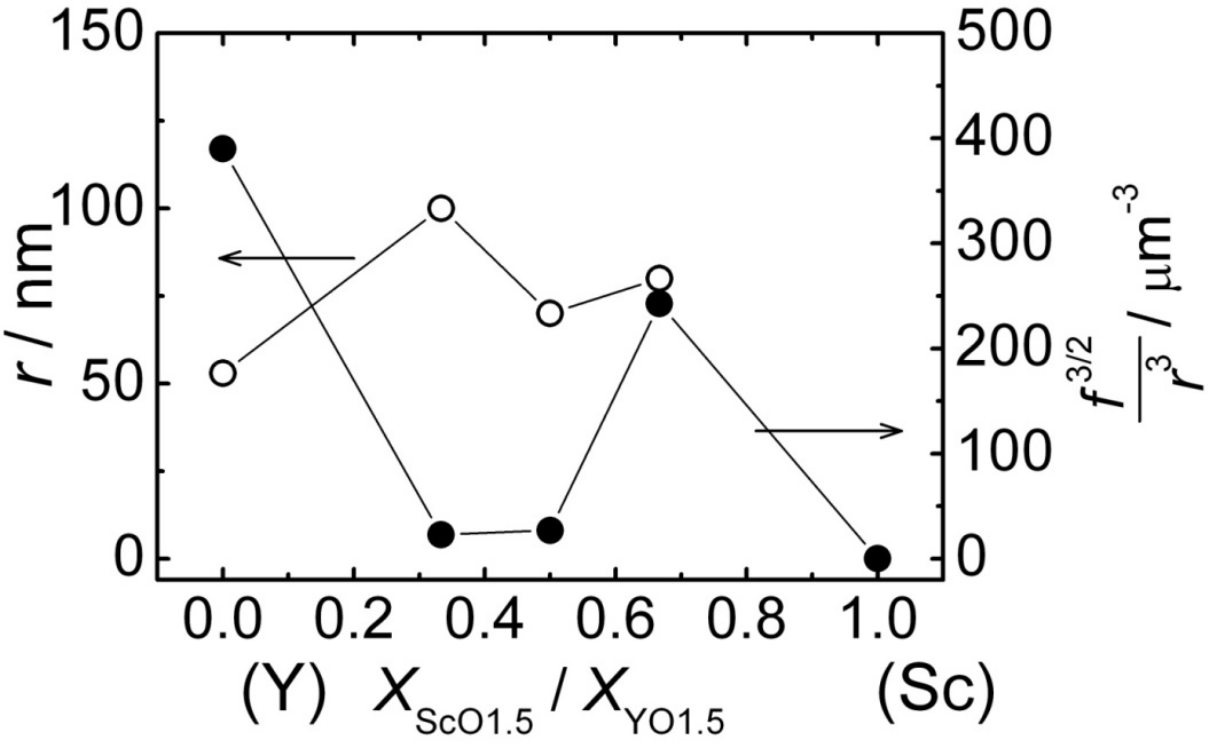

Figure 7.3 The average size of small grains, *r*, and the value of three-second power of area fraction of small grains, *f*, divided by the cube of average size of small grains as a function of the ratio of mole fraction of scandium to yttrium.

7.3.2 Conductivity Measurement of Co-doped Barium Zirconate

7.3.2.1 Bulk Conductivity

Figure 7.4 (a) shows the bulk conductivity of scandium and yttrium co-doped barium zirconate in Arrhenius form, and the bulk conductivity at 150 °C is plotted as a function of the ratio of the mole fraction of scandia to yttria in Fig. 7.4 (b). The bulk conductivity increased

with the ratio of yttria in all temperature ranges. Assuming that the concentration of protons in the oxide is the same value in all the samples, the increase of the bulk conductivity comes from the increase of the mobility of protons. When a proton jumps from the vicinity of one oxygen site to another, the proton has to pass between cations. The repulsion force from scandium ion might be stronger than that from yttrium ion because of weaker screening effects by the smaller numbers of electrons surrounding the atomic nucleus. Therefore, the activation energy of yttrium-doped barium zirconate might be lower than that of scandium-doped barium zirconate, which in turn means that the mobility of protons in yttrium-doped barium zirconate might be higher than that in scandium-doped barium zirconate. This can be recognized from experimental data of activation energies of co-doped barium zirconate listed in Table 7.2. Of course, this is one of the physicochemical expectations. More investigation based on quantum chemistry is needed to explain the origin of this big difference.

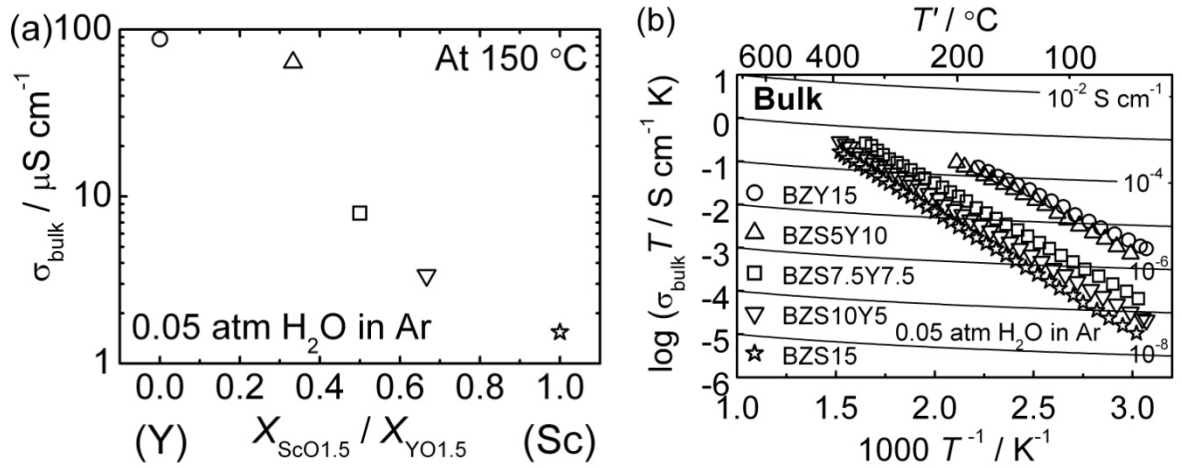

Figure 7.4 (a) The bulk conductivity of scandium and yttrium co-doped barium zirconate in humidified argon, the pressure of which was 0.05 atm, as a function of temperature plotted in Arrhenius form. (b) Bulk conductivity as a function of the ratio of the mole fraction of scandium to yttrium at 150 °C.

7.3.2.2 Inverse of Grain-boundary Resistance

The inverse of grain-boundary resistances of scandium and yttrium co-doped barium zirconate is plotted as a function of temperature in Arrhenius form in Fig. 7.5 (a). Fig. 7.5 (b) shows the inverse of grain-boundary resistances as a function of the ratio of the mole fraction of scandium to yttrium at 150 °C. *S* and *L* in the figures represent the surface area and thickness of pellets used for conductivity measurement, respectively. In the same manner as for bulk conductivity, the inverse of grain-boundary resistances of BZS15, BZS10Y5 and BZS7.5Y7.5 were lower than that of BZY15. However, the inverse of grain-boundary resistance of BZS5Y10 was higher than that of BZY15. The differences of the inverse of grain-boundary resistances among them were not as large as those of the bulk conductivities. At temperatures higher than 110 °C, the inverse of grain-boundary resistance of BZS5Y10 was the highest among scandium and yttrium co-doped barium zirconates in this study.

Based on the brick layer model, the specific grain-boundary conductivity ($\sigma_{sp.g.b}$) was calculated according to E.q (7-1).[98Hai]

$$\sigma_{\text{sp.g.b.}} = \frac{g}{G}\frac{L}{S}\frac{1}{R_{\text{g.b.}}} \tag{7-1}$$

where *g* is grain-boundary thickness, *G* is the average grain size and $R_{\text{g.b.}}$ is a grain-boundary resistance, respectively. In general, it is not easy to estimate the grain-boundary thickness. In addition, very fine grains of about 50 nm were contained in BZY15, which made it difficult to estimate the average grain sizes. This causes the difficulty in calculating the specific grain-boundary conductivity of BZY15. However, we know the average grain size, *G*, increased with the composition ratio from experiments. If the grain-boundary thickness is constant regardless of the mixing ratio of scandium and yttrium, it is reasonably concluded that the specific grain-boundary conductivity decreases with increasing composition ratio of scandium. Therefore, there should be a trade-off relationship between the grain size and the specific

grain-boundary conductivity with the mixing ratio of scandia to yttria. Thus, there is an optimum mixing ratio of scandium and yttrium. BZS5Y10 seems to be close to the best composition, showing the highest grain-boundary conductivity in the employed sintering-procedure at 1600 °C.

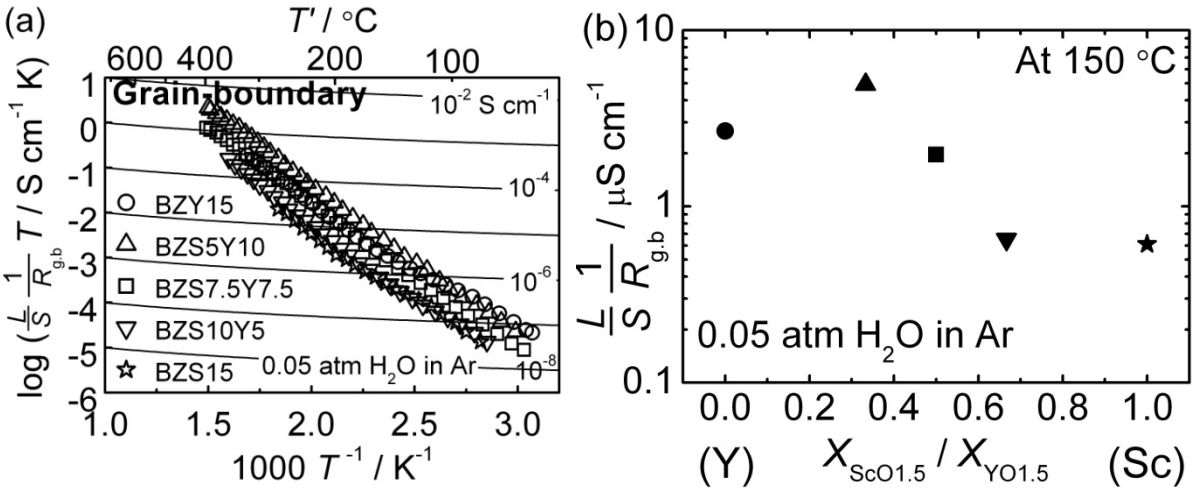

Figure 7.5 (a) The grain-boundary conductivity of scandium and yttrium co-doped barium zirconate in humidified argon, the pressure of which was 0.05 atm, as a function of temperature plotted in Arrhenius form.
(b) The grain-boundary conductivity as a function of the ratio of the mole fraction of scandia to yttria at 150 °C.

7.3.2.3 Reproducibility of Conductivities in BZS5Y10

As described in Chapter 1, there are big differences among the reported conductivities of trivalent cation doped barium zirconate, and the poor reproducibility of conductivity in trivalent cation doped barium zirconate was often mentioned[03Kre]. We thus investigated the reproducibility of conductivities in BZS5Y10, which showed the highest inverse of grain-boundary resistance in our experiment. Three batches of BZS5Y10 (batch-1, 2 and 3) powder were synthesized by the solid state reaction method and sintered after the same procedure for making pellets. Batch-2 was synthesized using a zirconia from a different supplier (99.97 % including 2% of hafnia (HfO_2), Daiichi kigenso). The difference of zirconia was in grain size;

Table 7.2 Activation energies (E_σ) and pre-exponential (A) terms in bulk and grain-boundary conductivity of scandium and yttrium co-doped barium zirconates.

	σ_{bulk}		$\sigma_{g.b.}$	
Sample	E_σ (eV)	A (S cm^{-1} K)	E_σ (eV)	A (S cm^{-1} K)
$BaZr_{0.85}Sc_{0.15}O_{3-\delta}$	0.556	2.79×10^3	0.577	2.18×10^3
$BaZr_{0.85}Sc_{0.10}Y_{0.05}O_{3-\delta}$	0.530	3.11×10^3	0.652	2.14×10^4
$BaZr_{0.85}Sc_{0.075}Y_{0.075}O_{3-\delta}$	0.515	4.75×10^3	0.653	6.33×10^4
$BaZr_{0.85}Sc_{0.05}Y_{0.10}O_{3-\delta}$	0.479	1.29×10^4	0.678	2.91×10^5
$BaZr_{0.85}Y_{0.15}O_{3-\delta}$	0.447	7.72×10^3	0.563	8.22×10^3

* $\sigma T = A \exp(-\frac{E_\sigma}{kT})$ is employed.

480 nm from Daiichi kigenso and 24 nm from Tosoh. Fig. 7.6 shows the bulk conductivities and inverse of grain-boundary resistances of three BZS5Y10 pellets in Arrhenius form. Fig. 7.6 indicates a good experimental reproducibility of conductivities of BZS5Y10 because there are no differences in the bulk conductivities and inverse of grain-boundary resistances among three pellets of BZS5Y10. The total conductivity of BZS5Y10 at higher temperatures is estimated using the activation energy and pre-exponential term in Table 7.2 which was obtained from Fig. 7.4 (a) and 7.5 (a). The estimated total conductivity of BZS5Y10 at 600 °C is 1.6×10^{-2} S cm^{-1} on the assumption of no dehydration at 600 °C. This value satisfies the requirement for SOFC using electrolyte-supported type cells, which implies that this electrolyte is a strong candidate for a new type of fuel cell as mentioned by many researches. In the literature, the highest total conductivity of 1×10^{-2} S/cm at 600 °C was obtained in a pellet sintered at 1800 °C for 20 hours[07Igu]. The co-doping technique of scandium and yttrium allows us to have the same class of total conductivity even at the normal sintering temperature of 1600 °C.

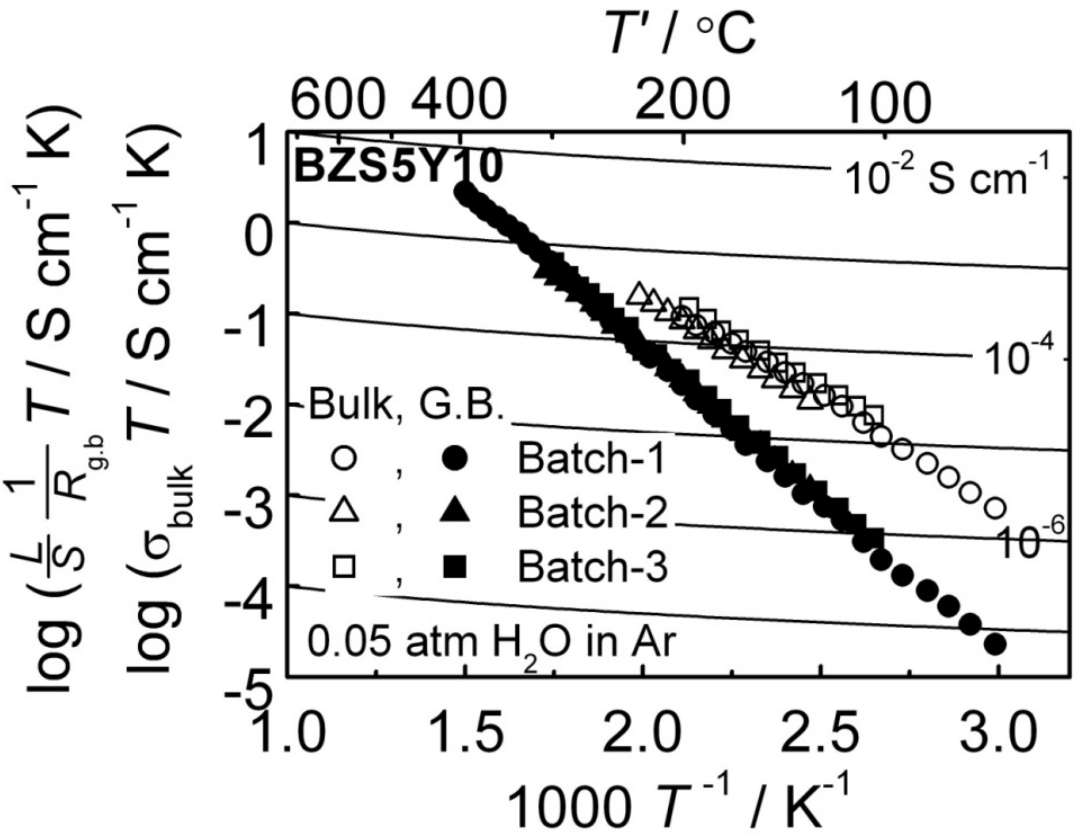

Figure 7.6 The bulk and grain-boundary conductivity of three batches of BZS5Y10 in humidified argon, the pressure of which was 0.05 atm, as a function of temperature plotted in Arrhenius form.

7.4 Conclusion

The results obtained in this work can be summarized as follows:

(1) By co-doping scandium into yttrium-doped barium zirconate, the grain-boundary concentration of barium zirconate was reduced and we would obtain single phase barium zirconate.

(2) The bulk conductivities of scandium and yttrium co-doped barium zirconate increased with the ratio of yttria. This might be because the mobility of protons in yttrium-doped barium zirconate is larger than that in scandium-doped barium zirconate. On the other hand, $BaZr_{0.85}Sc_{0.05}Y_{0.10}O_{3-\delta}$ has the highest inverse of grain-boundary resistance among $BaZr_{0.85}Sc_xY_{0.15-x}O_{3-\delta}$ (x=0, 0.05, 0.075, 0.10, 0.15). This is related to the fact that there is

a trade-off between the grain size and specific grain-boundary conductivity with the ratio of scandium to yttrium.

(3) We confirmed good experimental reproducibility of conductivities in $BaZr_{0.85}Sc_{0.05}Y_{0.10}O_{3-\delta}$. The total conductivity of $BaZr_{0.85}Sc_{0.05}Y_{0.10}O_{3-\delta}$ at 600 °C was estimated to be 1.6×10^{-2} S cm^{-1} by using the activation energy and pre-exponential terms of bulk and grain-boundary obtained in this study.

References

[98Hai] S.M. Haile, D. L. West and J. Campbell, *Journal of Materials Research*, **13** [6], 1576-1595 (1998).

[03Kre] K.D. Kreuer, *Annual Review of Materials Research,* **33**, 333-359 (2003).

[07Igu] F. Iguchi, N. Sata, T. Tsurui, and H. Yugami, *Solid State Ionics,* **178**, 691-695 (2007).

Chapter 8

Effect of Cation Substitution on Conductivity and Microstructure of Sintered Barium Zirconate

8.1 Introduction

In this chapter, we attempted to substitute A site ion or B site ion in yttrium-doped barium zirconate for isovalent cation in order to improve the conductivity of barium zirconate. Then, we investigated microstructure and proton conductivity. In addition, we investigated the microstructure and conductivity of yttrium and scandium doped barium hafnate.

8.2 Experimental

We made pellets having various compositions. The pellets we made in this study are listed in Table 8.1. Crystalline powders of various samples were synthesized by conventional solid state reaction and the detail is described in Chapter 2 and 3. The purity and source of raw materials are tabulated in Table 8.2.

The lattice parameters of the sintered pellets were determined by XRD. Also, microstructures of the sintered pellets were observed by SEM.

Conductivity of the sintered pellets was measured by AC 2-terminal method as described in Chapter 2 and 3.

8.3. Yttrium or scandium doped barium hafnate

8.3.1 Yttrium-doped barium hafnate

Only perovskite-type barium hafnate phase was detected in all the pellets by XRD. The apparent lattice parameters of barium hafnate phase as cubic perovskite are shown as a function of the mole fraction of dopant cation oxide in Fig 8.1. It is reasonable that the

Table 8.1 Compositions and abbreviations of samples.

Samples Composition	Abbreviation
$BaHf_{0.90}Y_{0.10}O_{3-\delta}$	BHY10
$BaHf_{0.85}Y_{0.15}O_{3-\delta}$	BHY15
$BaHf_{0.80}Y_{0.20}O_{3-\delta}$	BHY20
$BaHf_{0.70}Y_{0.30}O_{3-\delta}$	BHY30
$BaHf_{0.90}Sc_{0.10}O_{3-\delta}$	BHS10
$BaHf_{0.85}Sc_{0.15}O_{3-\delta}$	BHS15
$BaHf_{0.80}Sc_{0.20}O_{3-\delta}$	BHS20
$BaHf_{0.70}Sc_{0.30}O_{3-\delta}$	BHS30
$BaZr_{0.80}Ti_{0.05}Y_{0.15}O_{3-\delta}$	BZ80T5Y15
$BaZr_{0.75}Ti_{0.10}Y_{0.15}O_{3-\delta}$	BZ75T10Y15
$BaZr_{0.70}Ti_{0.15}Y_{0.15}O_{3-\delta}$	BZ70T15Y15
$Ba_{0.75}Sr_{0.25}Zr_{0.85}Y_{0.15}O_{3-\delta}$	B75S25ZY15
$Ba_{0.50}Sr_{0.50}Zr_{0.85}Y_{0.15}O_{3-\delta}$	B50S50ZY15
$Ba_{0.25}Sr_{0.75}Zr_{0.85}Y_{0.15}O_{3-\delta}$	B25S75ZY15
$SrZr_{0.85}Y_{0.15}O_{3-\delta}$	SZY15

Table 8.2 Purity and source of raw materials

Raw material	Chemical formula	Purity (mass %)	Source
Barium carbonate	$BaCO_3$	99.9	Wako
Strontium carbonate	$SrCO_3$	99.99	Wako
Zirconium oxide	ZrO_2	99.97 (including 2% of hafnium oxide)	Tosoh
Hafnium oxide	HfO_2	99.9 (including 2% of zirconium oxide)	Mitsuwa Kagaku
Titanium oxide	TiO_2	99.9	Wako
Yttrium oxide	Y_2O_3	99.99	Daiichi kigenso
Scandium oxide	Sc_2O_3	99.9	Shin-Etsu Chemical

apparent lattice parameters of barium hafnate phase increase by doping yttrium because the ionic radius of yttrium ion (Y^{3+}: 0.0900 nm[76Sha]) is larger than that of hafnium ion (Hf^{4+}: 0.071 nm[76Sha]). But, the apparent lattice parameters were almost constant over $X_{YO1.5} = 0.05$ (BHY10). Thus, there is a possibility that Y-doped barium hafnates sintered with powders made at 1300 °C by solid state reaction method are metastable state of dual phases of low Y-doped barium hafnate and high Y-doped barium hafnate as expressed for Y-doped barium zirconate in Chapter 6.

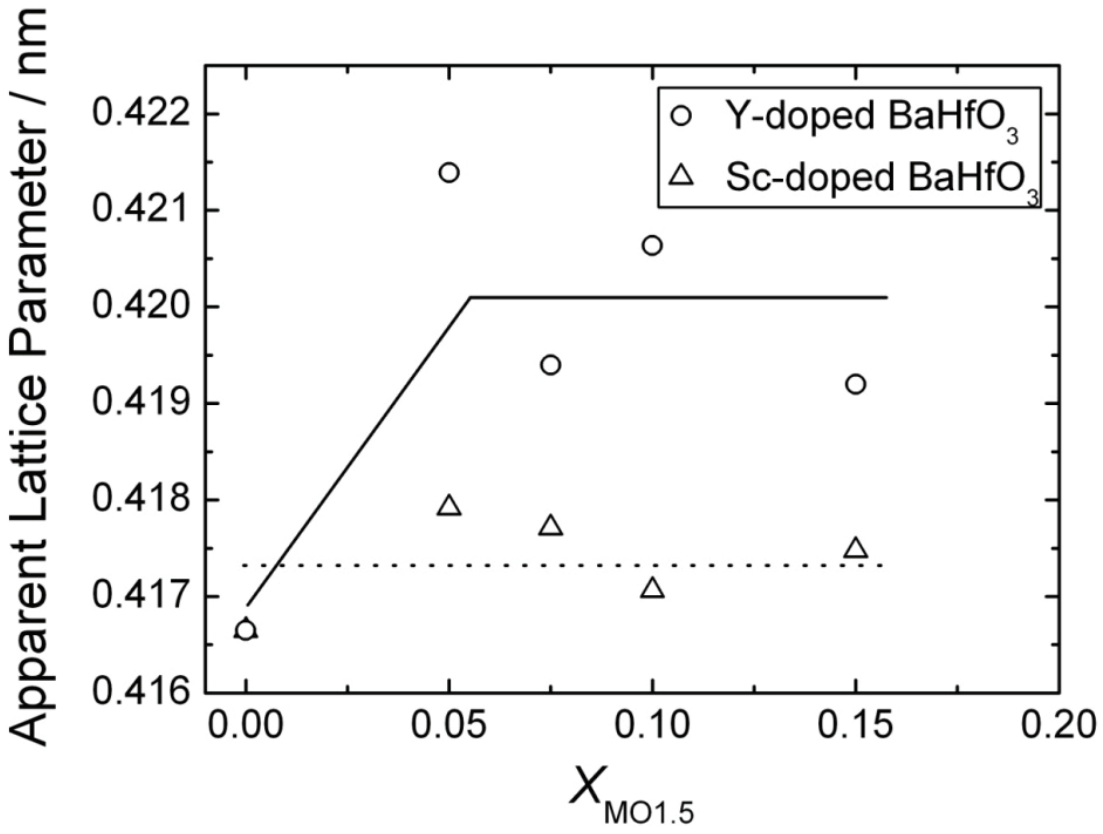

Figure 8.1 Apparent lattice parameters of barium hafnate phase as a function of the mole fraction of dopant cation oxide.

Figure 8.2 shows SEM images of Y-doped barium hafnates. The microstructure of all the pellets was bimodal like Y-doped barium zirconate (Chapter 6) and the amount of the smaller grains decreased with increasing mole fraction of yttrium.

Figure 8.3 shows the bulk conductivities and the inverse of grain-boundary resistances of Y-doped barium hafnates with those of 15% Y-doped barium zirconate (BZY15) in the Arrhenius form. Bulk conductivities and inverse of grain-boundary resistances of all the pellets were lower than those of BZY15. There was no large difference among bulk conductivities of Y-doped barium hafnates except for BHY20 whose bulk conductivity was lower than that of other Y-doped barium hafnates. This trend of bulk conductivity in Y-doped

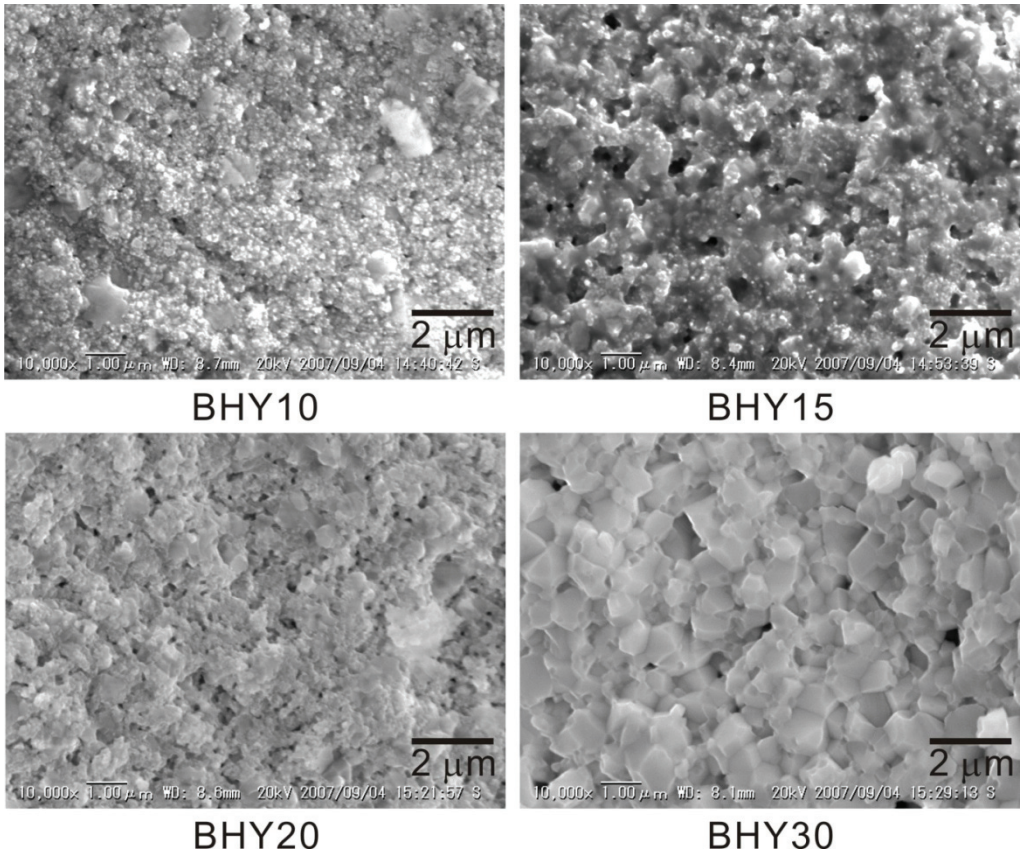

Figure 8.2 Cross-sectional SEM images of Y-doped barium hafnates

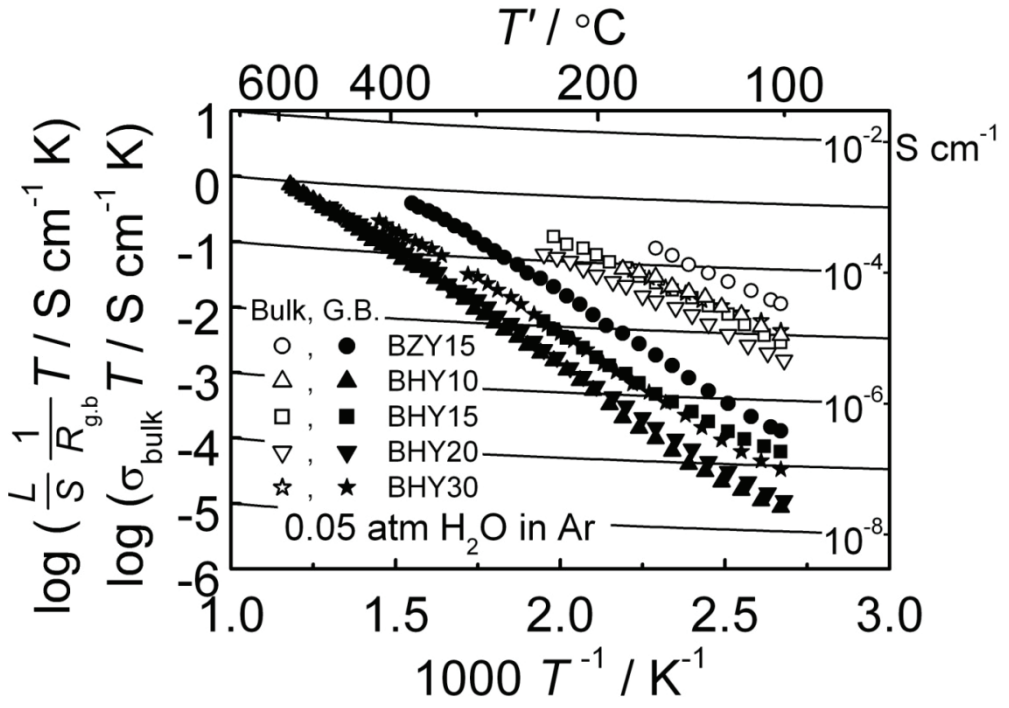

Figure 8.3 Bulk conductivities, σ_{bulk}, and inverse of grain-boundary resistances, $\frac{L}{S}\frac{1}{R_{g.b.}}$, of (a) Y-doped barium hafnates in Ar-0.05 % H_2O as a function of temperature with those of Y doped barium zirconates.

barium hafnate is a little different from that in Y-doped barium zirconate whose bulk conductivity increases with increasing mole fraction of yttrium until $X_{YO1.5}$ = 0.10 (BZY20) as described in Chapter 2. We need to repeat the measurement carefully, although we expect that the fact of lower conductivity of Y-doped barium hafnate than that of Y-doped barium zirconate does not change.

8.3.2 Scandium-doped barium hafnate

Scandium-doped barium hafnates were prepared just for comparison with yttrium-doped barium hafnates. No second phase was observed in all the pellets by XRD. Thus, we can say that the solubility of scandium into barium hafnate is more than $X_{ScO1.5}$ = 0.15 (BHS30). Also, the lattice parameters of the barium hafnate phase did not change by doping scandium as shown in Fig 8.1. This is because the ionic radius of scandium ion (Sc^{3+}: 0.0745 nm[76Sha]) is almost the same as that of hafnium ion (Hf^{4+}: 0.071 nm[76Sha]).

Figure 8.4 shows SEM images of Sc-doped barium hafnates. Well-grown and homogeneous grains were observed in all the pellets like Sc-doped barium zirconate (Chapter 6). The Sc-doped barium hafnates in this study might be in the single phase region at sintering temperature (1600 °C) and also at synthesizing temperature (1300 °C), as with Sc-doped barium zirconate described in Chapter 6.

Figure 8.5 shows the bulk conductivities and inverse of grain-boundary resistances of Sc-doped barium hafnates with those of 15% Sc-doped barium zirconate (BZS15) in the Arrhenius form. Bulk conductivity of Sc-doped barium hafnates increased with the increase of the mole fraction of scandium until $X_{ScO1.5}$ = 0.10 (BHS20) and bulk conductivity of BHS30 was almost the same as that of BHS20. Bulk conductivity of all the Sc-doped barium hafnates was lower than that of BZS15. The inverse of grain-boundary resistance of Sc-doped barium hafnates showed the same tendency as bulk conductivity except for BHS30.

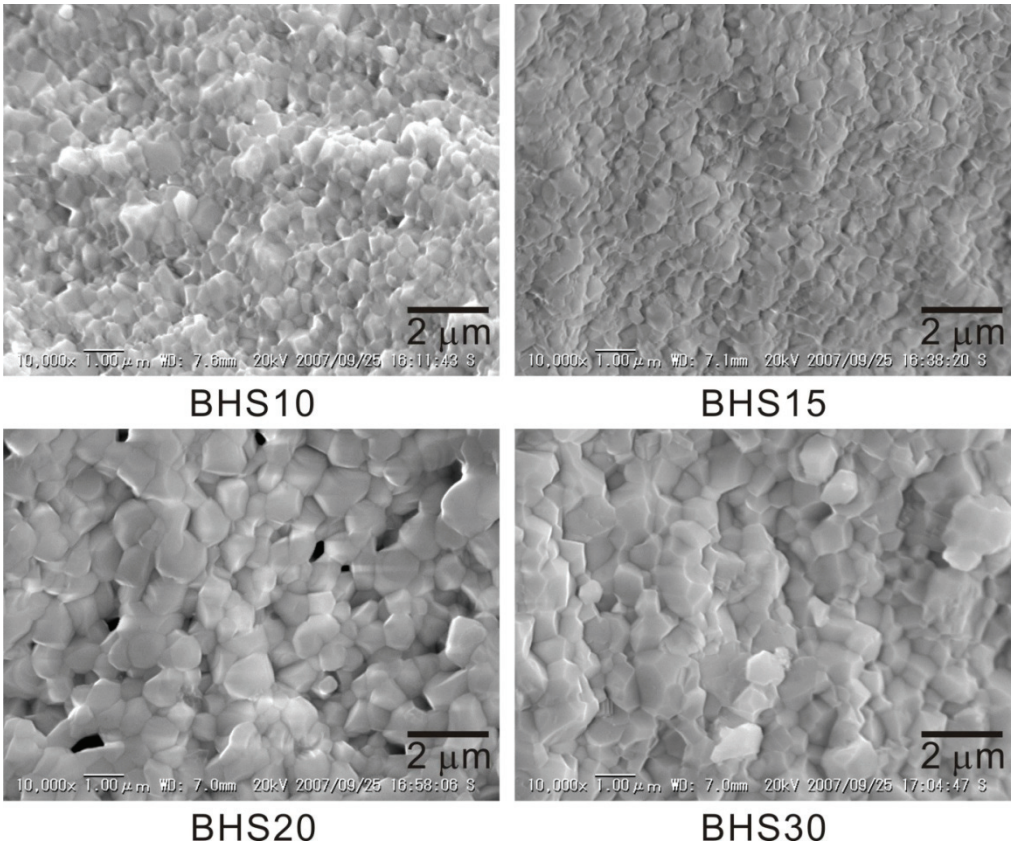

Figure 8.4 Cross-sectional SEM images of Sc-doped barium hafnates.

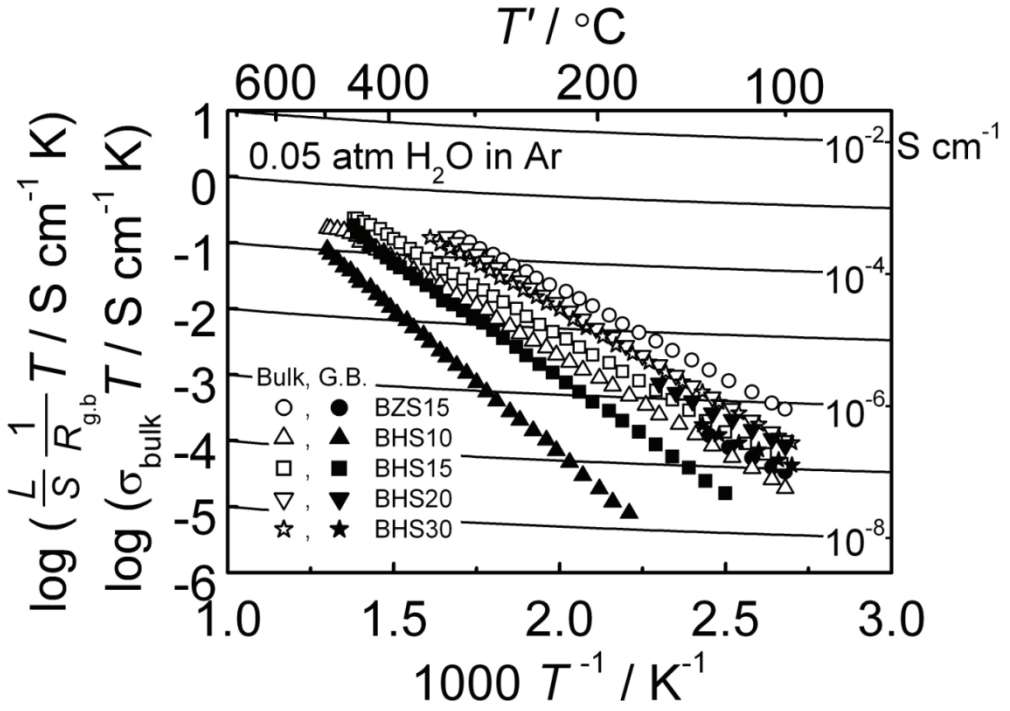

Figure 8.5 Bulk conductivities, σ_{bulk}, and inverse of grain-boundary resistances, $\frac{L}{S}\frac{1}{R_{g.b.}}$, of Sc-doped barium hafnates in Ar-0.05 % H_2O as a function of temperature with those of Sc doped barium zirconates.

8.4 Partial substitution of titanium for zirconium site in barium zirconate

Figure 8.6 (a) shows XRD patterns of BZ80T5Y15, BZ75T10Y15 and BZ70T15Y15 sintered at 1600 °C for 24 hours. There was no diffraction peak of second phase in any of the pellets. Fig 8.6 (b) shows the lattice parameters of barium zirconate phase as a function of the mole fraction of titanium oxide. The lattice parameters decreased linearly with increasing the mole fraction of titanium oxide. Because the ionic radius of titanium ion (Ti^{4+}: 0.0605 nm[76Sha]) is smaller than that of zirconium ion (Zr^{4+}: 0.072 nm[76Sha]), this means that titanium ions were substituted for zirconium site in barium zirconate.

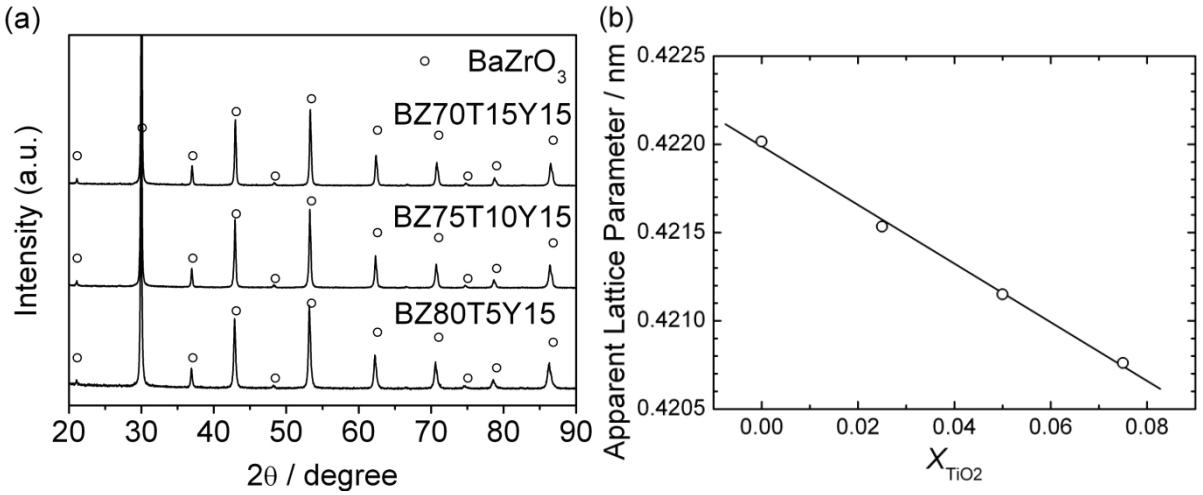

Figure 8.6 (a) XRD patterns of pellets of BZ80T5Y15, BZ75T10Y15 and BZ70T15Y15 after heat- treatment at 1600 °C for 24 hours. ○ indicates diffraction patterns of barium zirconate ($BaZrO_3$, JCPDS No. 00-006-0399). (b) Apparent lattice parameters of barium zirconate phase as a function of the mole fraction of titanium oxide, X_{TiO2}.

Figure 8.7 shows SEM images of BZ80T5Y15, BZ75T10Y15 and BZ70T15Y15. BZ80T5Y15 had bimodal microstructures which consist of two sizes of grains; large grain is about 500 nm and the other is about less than 50 nm, and good grain growth was observed in BZ70T15Y15. BZ75T10Y15 had an intermediate microstructure between BZ70T15Y15 and BZ80T5Y15. As described in Chapter 6, the slightly higher BaO-composition than stoichiometric yttrium-doped barium zirconate has phase relationship of barium zirconate and

liquid, and a small extra barium oxide promotes grain growth in yttrium-doped barium zirconate. Thus, there is a possibility that a part of the dopant cation dissolve into A site and that liquid phase which is formed by extra barium oxide and promotes grain growth as in the case of 15% Gd-doped barium zirconate (Chapter 3).

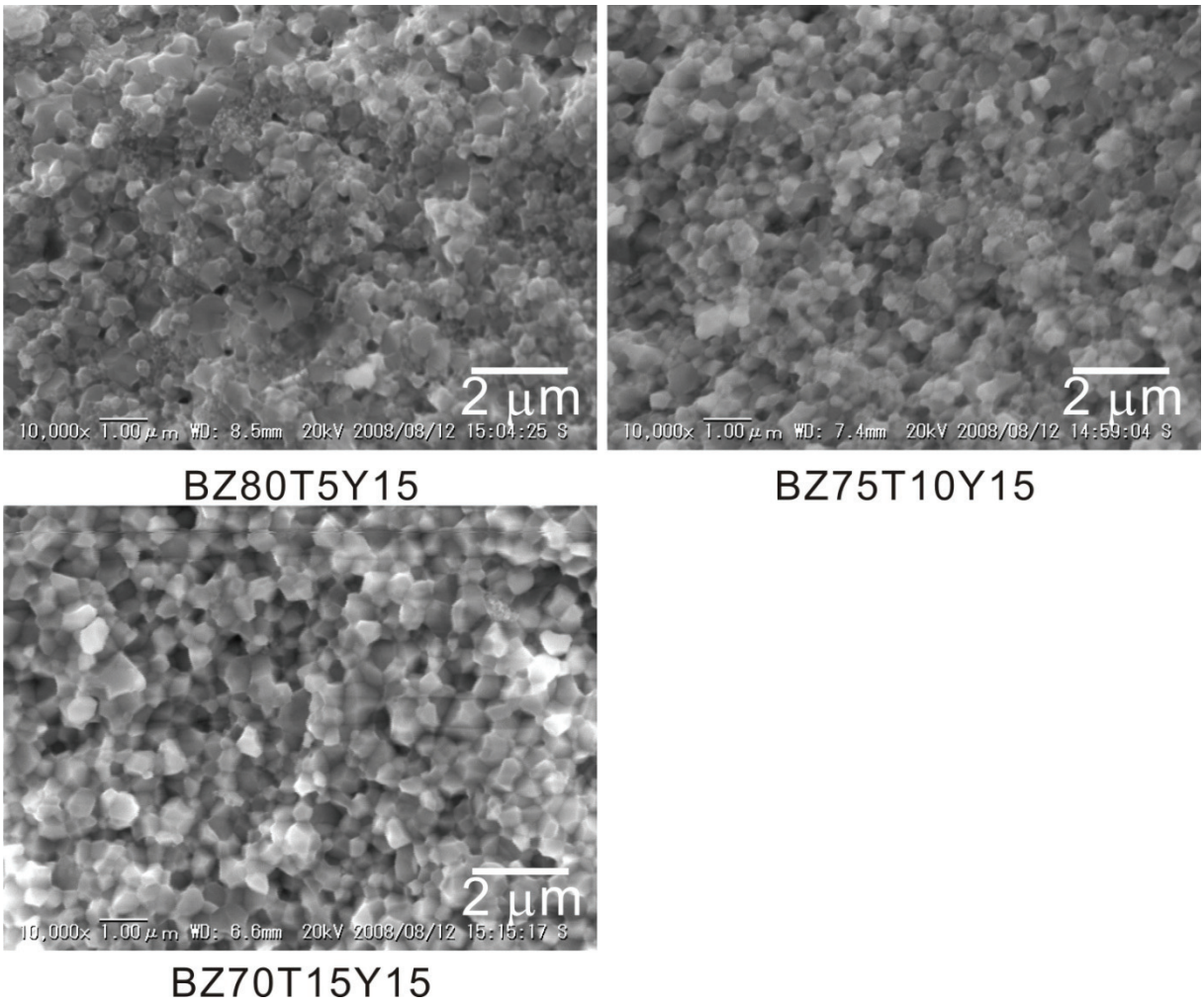

Figure 8.7 Cross-sectional SEM images of BZ80T5Y15, BZ75T10Y15 and BZ70T15Y15.

Schematic chemical potential curve of yttrium ion in A site ($\mu_{Y^{3+}}^{A-site}$) and B site ($\mu_{Y^{3+}}^{B-site}$) can be written as a function of average site sizes in Fig. 8.8 (a). In the figure, the chemical potential of yttrium ion of B site in BZY15 locates at the left side of minimum point in the chemical potential curve of B site because the ionic radius of yttrium ion is larger than that of zirconium ion. In the same way, the chemical potential of yttrium ion of A site in

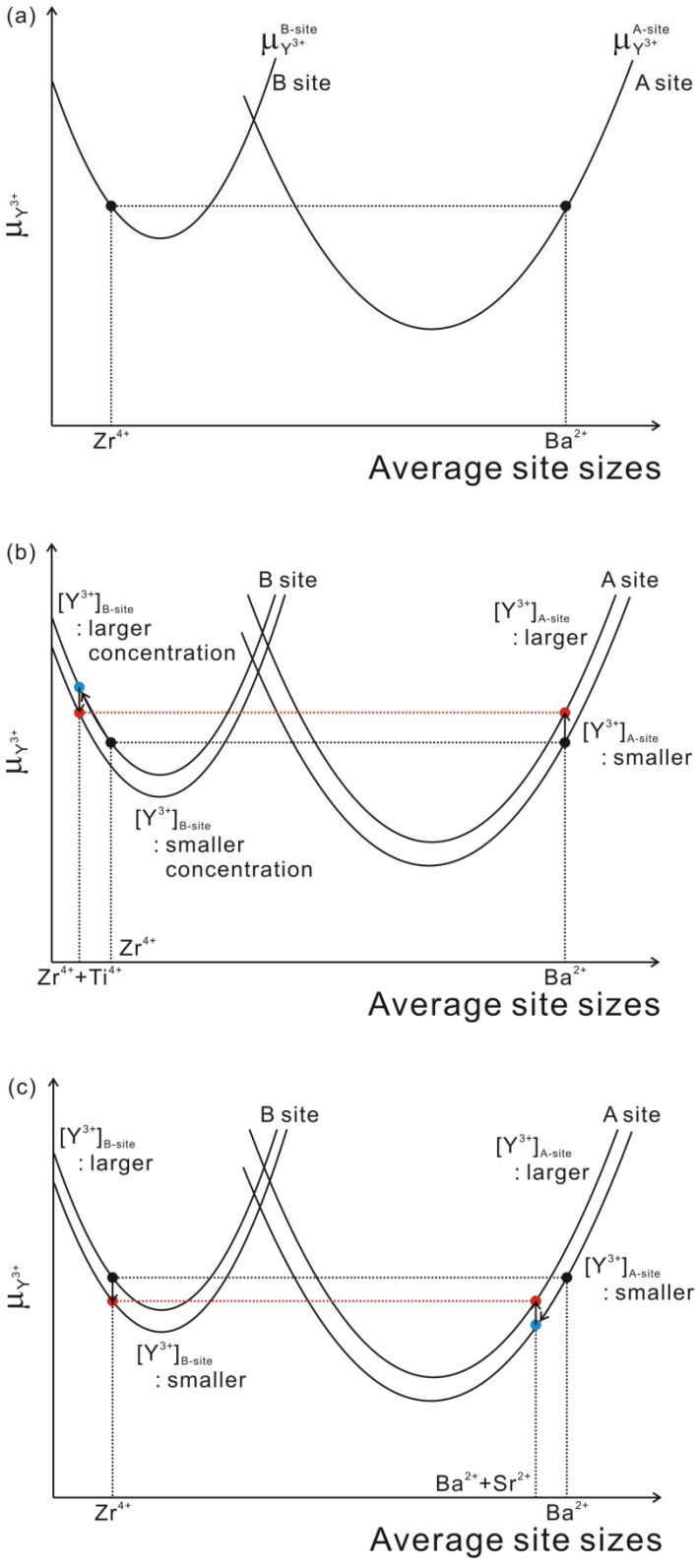

Figure 8.8 Schematic chemical potential curve of yttrium ion in A site and B site in case of BZY15, (b) increasing of the amount of titanium ion in B site and (c) increasing of the amount of strontium ion in A site.

BZY15 locates at the right side of minimum point in the chemical potential curve of A site because the ionic radius of yttrium ion is smaller than that of barium ion[76Sha]. At first, by increasing of the amount of titanium ion in B site, the average site sizes of B site shrinks because the ionic radius of titanium ion is smaller than that of zirconium ion[76Sha], and then the chemical potential of yttrium ion of B site increases. As the result, some yttrium ions of B site move to A site in order to equalize both chemical potentials of yttrium (Fig. 8.8 (b)). Therefore, the concentration of yttrium in A site increases. The amount of the liquid phase should increase with the increase of mole fraction of titanium oxide. But, this is just a hypothesis which is necessary to be confirmed by experiments in future.

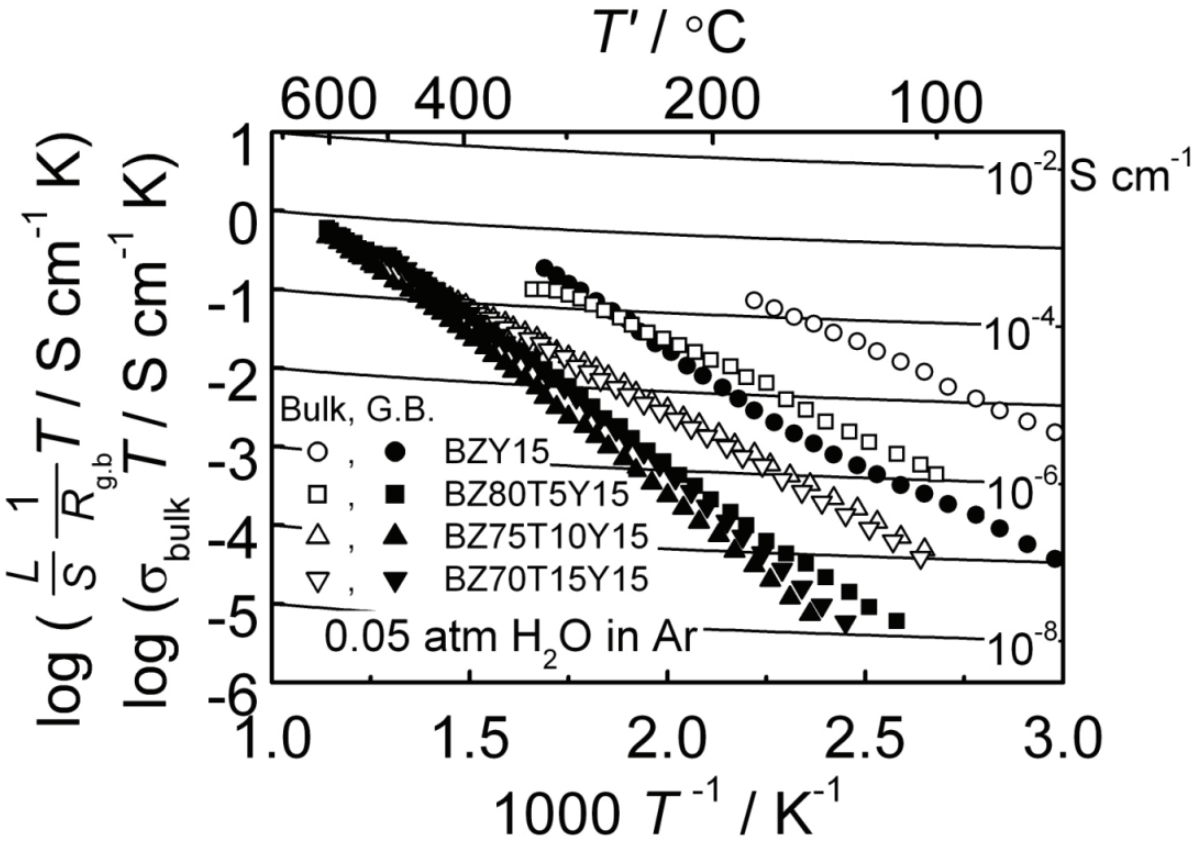

Figure 8.9 Bulk conductivities, σ_{bulk}, and inverse of grain-boundary resistances, $\frac{L}{S}\frac{1}{R_{g.b.}}$, of BZ80T5Y15, BZ75T10Y15 and BZ70T15Y15 in Ar-0.05 % H_2O as a function of temperature with that of Y doped barium zirconate.

Figure 8.9 shows the bulk conductivities and inverse of grain-boundary resistances of BZ80T5Y15, BZ75T10Y15, BZ70T15Y15 and BZY15 in the Arrhenius form. Bulk conductivity decreased with increasing mole fraction of titanium oxide. One can imagine that the lower bulk conductivities than BZY15 are a result of partial substitution of yttrium for A site, as like 15% Gd-doped barium zirconate (Chapter 3).

8.5 Substitution of divalent cation for A site ($Ba_xSr_{1-x}Zr_{0.85}Y_{0.15}O_{3-\delta}$)

Figure 8.10 (a) shows XRD patterns of pellets sintered at 1600 °C for 24 hours. Cubic perovskite phase was confirmed in BZY15, B75S25ZY15, B50S50ZY15 and B25S75ZY15, and orthorhombic perovskite phase was confirmed in SZY15. Diffraction peaks of phases whose structures do not belong to perovskite structure were not identified in BZY15, B75S25ZY15, B50S50ZY15 and B25S75ZY15. Weak diffraction peaks of phases whose structures do not belong to perovskite structure were identified only in SZY15. Assuming cubic perovskite structure, the apparent lattice parameters of barium strontium zirconate phases except for SZY15 are evaluated as a function of the mole fraction of strontium oxide in Fig 8.10 (b). Until X_{SrO} = 0.25 (B50S50ZY15), the apparent lattice parameters decreased with increasing mole fraction of strontium oxide. It is reasonable because the ionic radius of strontium ion (Sr^{2+}: 0.144 nm[76Sha]) is smaller than that of barium ion (Ba^{2+}: 0.161 nm[76Sha]).

Figure 8.11 shows SEM images of BZY15, B75S25ZY15, B50S50ZY15, B25S75ZY15 and SZY15. The microstructures of BZY15 and B75S25ZY15 were bimodal, and the amount of smaller grains in B75S25ZY15 was much smaller than in BZY15. Good grain growth was observed in B50S50ZY15, B25S75ZY15 and SZY15. From Fig 8.10, we can see that the average grain size increases by substituting strontium ions for barium ions. This might be related to the partial substitution of yttrium into A site like titanium substituted

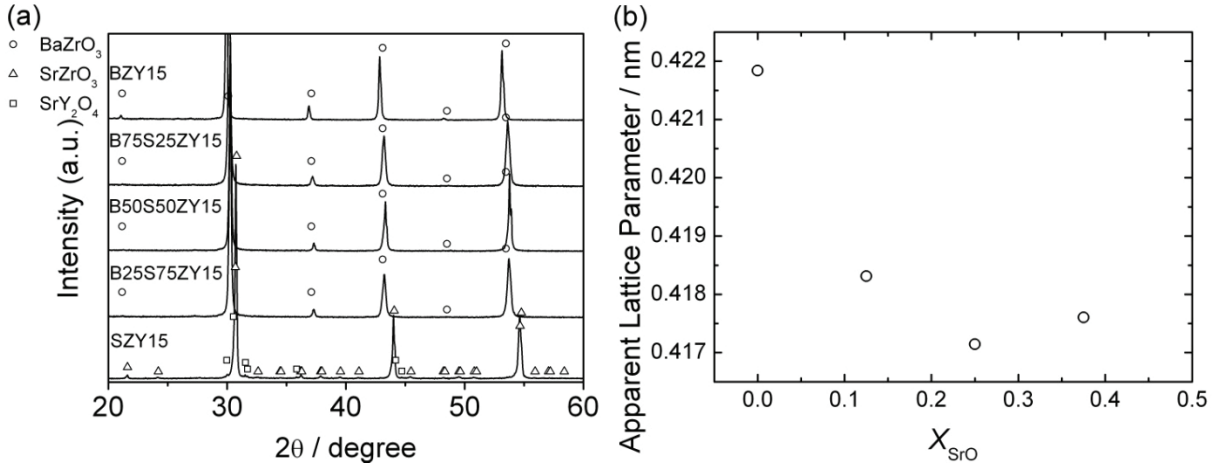

Figure 8.10 (a) XRD patterns of pellets of BZY15, B75S25ZY15, B50S50ZY15, B25S75ZY15 and SZY15 after heat- treatment at 1600 °C for 24 hours. Each symbol indicates diffraction patterns of ○ ($BaZrO_3$, JCPDS No. 60399), △ ($SrZrO_3$, JCPDS No. 00-044-0161) and □ (SrY_2O_4, JCPDS No. 00-032-1272). (b) Apparent lattice parameters of barium zirconate phase as a function of the mole fraction of strontium oxide, X_{SrO}.

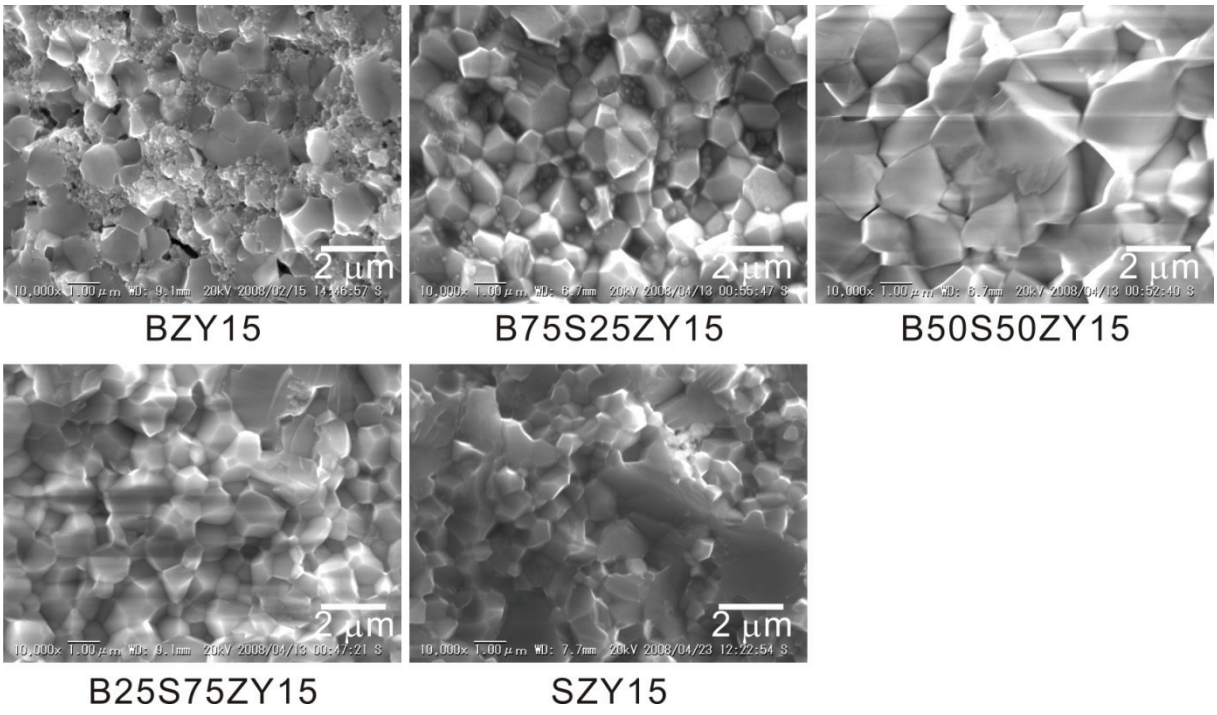

Figure 8.11 Cross-sectional SEM images of BZY15, B75S25ZY15, B50S50ZY15, B25S75ZY15 and SZY15.

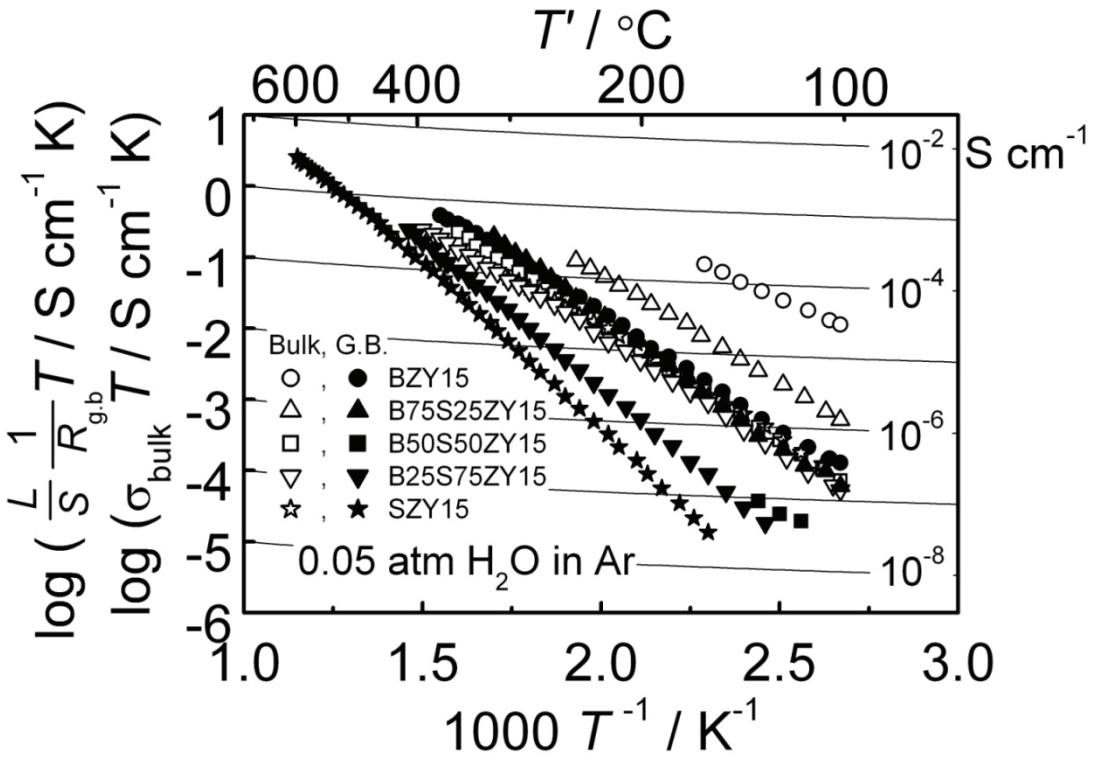

Figure 8.12 Bulk conductivities, σ_{bulk}, and inverse of grain-boundary resistances, $\frac{L}{S}\frac{1}{R_{g.b.}}$, of BZY15, B75S25ZY15, B50S50ZY15, B25S75ZY15 and SZY15 in Ar-0.05 % H_2O as a function of temperature.

samples, because the ionic radius of A site decreases by substituting strontium ions for barium ions.

Bulk conductivities and inverse of grain-boundary resistances of BZY15, B75S25ZY15, B50S50ZY15, B25S75ZY15 and SZY15 were measured and the results are shown in Fig 8.12. Compared with BZY15, the bulk conductivities decreased. We consider that the reason for the decrease of bulk conductivity is the same as titanium substituted samples.

8.6 Conclusion

Yttrium and scandium doped barium hafnates show the similar behavior as yttrium and scandium doped barium zirconate in terms of bulk conductivity and microstructure, but

we could not obtain yttrium or scandium barium hafnates whose total conductivity was larger than that of yttrium doped barium zirconate.

There is a relationship among bulk conductivity, microstructure and ionic radius of host ions and dopant cations. Substitution of titanium ion for zirconium ion reduces bulk conductivity and promotes grain growth. This might be caused by the dissolution of a part of yttrium ion into A site (Ba site) and shrink of lattice. Well grown grains should be an indirect evidence of the dissolution of the dopant cation into A site as we previously confirmed that extra barium oxide promotes the grain growth. Also, substitution of strontium ion for barium ion reduces the bulk conductivity and promotes grain growth. We consider that the reason is the same as titanium substituted samples, because the ionic radius of A site decreases by substituting strontium ions.

References

[76Sha] R. D. Shannon, *Acta Crystallographica Section A*, **32**, 751-767 (1976).

Chapter 9

Processing of Fine Powder, Sintering Behavior and Grain-boundary Resistance for Yttrium-doped Barium Zirconate

9.1 Introduction

As described in previous chapters, it is necessary to have larger grains of yttrium-doped barium zirconate in order to improve the high grain-boundary resistance. However, the microstructure of 15 % yttrium-doped barium zirconate ($BaZr_{0.85}Y_{0.15}O_{3-\delta}$), which was made by a solid state reaction method and sintered at 1600 °C for 24 hours, consists of two sizes of grains; large grain is about 1 μm and the other is about 50 nm by kinetic reason of cation diffusion because there is a difference of phase relationship between the sintering temperature (1600 °C) and a synthesizing temperature (1300 °C). Thus, if a particle size of synthesized powder is finer than that of synthesized powder by the solid state reaction method at 1300 °C, We expect to obtain large and homogeneous grains of yttrium-doped barium zirconate because the diffusion distance for cations becomes shorter during sintering at 1600 °C.

So far, we have employed a solid state reaction method combined with long time ball-milling (4 days) to obtain fine powder, but it was difficult to make fine powder. Then, we focused on the reported chemical synthesis method of trivalent-cation doped barium zirconate [01Grb,04Mag,07Bab,07Cer,08Epi,08Hig], and fine nondoped barium zirconate powder.[93Pot,95Pfa,98Mar,99Tag, 00Vei,02Sin,02Kol,02Aza,03Bos,07Mak] We summarized these reports in Table 1. There are mainly three methods by which fine barium zirconate powder less than 100 nm can be obtain; sol-gel method[01Gro,02Sin,07Cel,08Epi] and Pechini (modified Pechini) process[07Bab,08Hig] and spray pyrolysis method.[07buc] Sol-gel method have drawbacks such as high cost metal organics used as raw materials. The Sol-gel method has drawbacks such as the high cost of metal organics used as raw materials. The spray pyrolysis method is a very simple and low-cost process

Table 9.1 Synthesis method of doped or nondoped barium zirconate as reported in the literature.

Composition	Method	Raw materials	Particle size of synthesized powder	Synthesized temperature / °C	Ref.
$BaZr_{0.85}Me_{0.15}O_{2.925}$ (Me= Y, In, Ga)	Sol-gel	Ba, $Zr(nOPr)_4$, $Me(iOPr)_3$	7 nm	400	01Gro
$Ba_{0.99}Zr_{0.8}Y_{0.2}O_{3-\delta}$	Sol-gel	$BaCO_3$, Y_2O_3, $ZrO(NO_3)_2{\cdot}nH_2O$ Acrylamide monomer, *N,N*'-methylenebisacrylamide, α,α' azoisobutyronitril, aitric acid, ammonia	—	1250	04Mag
$BaZr_{0.85}Y_{0.15}O_{3-\delta}$	Modified Pechini process	$Ba(NO_3)_2$, $ZrO(NO_3)_2{\cdot}nH_2O$, $Y(NO_3)_3{\cdot}6H_2O$, glycine	—	1250	07Bab
$BaZr_{0.80}Y_{0.20}O_{3-\delta}$	Sol-gel	$Ba(OC_4H_9)_2$, $Zr(OC_4H_9)_2$, $Y(OC_4H_9)_2$, 2-MetOH	32.8 nm	130	07Cer
$BaZr_{0.80}Y_{0.20}O_{3-\delta}$	Sol-gel	$Ba(NO_3)_2$, $(C_3H_7O)_xZr(OH)_y$, $Y(NO_3)_3{\cdot}6H_2O$, citric acid, ethylene glycol	nanoparticle	1100	08Epi
$BaZr_{0.85}Y_{0.15}O_{3-\delta}$	Modified Pechini process	$Ba(NO_3)_2$, $ZrO(NO_3)_2$, $Y(NO_3)_3$, glycine	—	1000	08Hig
$BaZrO_3$	Molecular precursor route	$Ba(NO_3)_2$, $ZrO(NO_3)_2{\cdot}nH_2O$, $Na_2C_2O_4$	0.2 μm	800	93Pot
$BaZrO_3$	Wet chemical peroxide method	$BaCl{\cdot}2H_2O_2$, $ZrOCl_2$, NH_3	0.3 μm	900	95Pfa
$BaZrO_3$	Freeze-drying of chelated compounds	Zr-EDTA, Ba-EDTA	submicron	700	98Mar
$BaZrO_3$	Pechini process	BaO_2, $Zr(C_3H_7O)_4$, citric acid	2 μm	700	99Tag
$BaZrO_3$	Sol-Gel	$Ba(OBu^t)_2$, $Zr(OBu^t)_4$	30-40 nm	800	00Vei
$BaZrO_3$	Sol-Gel	$BaCO_3$, $ZrO(NO_3)_2{\cdot}5H_2O$, Acrylamide monomer, *N,N*'-methylenebisacrylamide, α,α' azoisobutyronitril	35 nm	1000	02Sin
$BaZrO_3$	Sol-Gel	$ZrO(OH)_2$, $Ba(OH)_2$	2 μm	240	02Kol
$BaZrO_3$	Solid state reaction	$Ba(NO_3)_2$, $ZrO(NO_3)_2{\cdot}nH_2O$	1 μm	800	02Aza
$BaZrO_3$	Sol-Gel	$BaCl_2$, $ZrOCl_2$, urea	50-120 nm	1200	03Bos
$BaZrO_3$	Spray prolysis	$Ba(NO_3)_2$, $ZrO(NO_3)_2{\cdot}nH_2O$	25-60 nm	800	07Buc
$BaZrO_3$	Microwave assisted hydrothermal synthesis	$Ba(OH)_2$, $ZrO(NO_3)_2$, NH_3, HCl	3.2 μm	150	07Mak

because aqueous nitrate solution is used. However, although this method is suitable for mass production, it is not suitable for producing small amounts and various powders because it is necessary to clean the apparatus each time. On the other hand, it was reported that very fine powder of barium titanate ($BaTiO_3$) (10-15 nm) which is finer than the powder obtained by the spray pyrolysis method (25-60 nm) was synthesized when an atomized aqueous solution was frozen in liquid nitrogen. The frozen aerosol was freeze-dried and heated at elevated temperatures[96McH] which was called a nitrate freeze-drying method. This method is suitable for the production of small amounts and various powders. Also, the modified Pechini process has a similar process character to the nitrate freeze-drying method in that it is suitable for production of small amounts and various powders, and the use of metal nitrates. In this study, we employed the nitrate freeze-drying method to obtain a fine powder of $BaZr_{0.85}Y_{0.15}O_{3-\delta}$ and investigated the sintering behavior and conductivity of $BaZr_{0.85}Y_{0.15}O_{3-\delta}$.

9.2 Experimental

Crystalline powder of 15 % yttrium-doped barium zirconate ($BaZr_{0.85}Y_{0.15}O_{3-\delta}$) was synthesized by nitrate freeze-drying method and the detail is described in Chapter 4. The freeze-dried powder was heated at various temperatures (400 ~ 1100 °C) in air or vacuum (~10^{-4} atm). Then, the powder was ball-milled for 10 hours. The powder was pressed into a pellet or bar at 392 MPa and then sintered at 1600 °C in sacrifice powders (90 mass % of synthesized barium zirconate and 10 mass % of $BaCO_3$).

Microstructures and compositional analysis of the synthesized powders and sintered samples were conducted by SEM. Density and lattice parameters of the sintered samples were also measured. The details of these analyses were described in Chapter 3. Thermal analysis was carried out on heating from room temperature to 1000 °C at a rate of 1 °C min^{-1} with

thermogravimetry and differential thermal analysis (TG-DTA) (Rigaku, TG 8120) in a stream of air at a flow rate of 100 ml min^{-1}.

Conductivity of the sintered samples was measured by AC 2-terminal method as described in Chapter 2 and 3.

9.3 Results and Discussion

9.3.1 Synthesis Condition

Thermal analyses of zirconyl nitrate dihydrate powder and mixed powder after freeze-drying at the ratio of 48.4 mass % barium nitrate ($Ba(NO_3)_2$), 39.3 mass % zirconyl nitrate dihydrate ($ZrO(NO_3)_2 \cdot 2H_2O$) and 12.3 mass % yttrium nitrate hydrate ($Y(NO_3)_3 \cdot 5.3H_2O$) were carried out to investigate the reaction temperature during synthesis of barium zirconate. Fig. 9.1 (a) and Fig. 9.1 (b) show TG-DTA profiles of these powders under air flow of 100 ml min^{-1}. Weight loss in zirconyl nitrate dihydrate continued gradually until 500 °C, and the total weight loss was 55 mass %. Also, the phase of zirconyl nitrate dihydrate powder after thermal analysis was confirmed to be zirconia (ZrO_2) by XRD analysis. Thus, this weight loss corresponds to decomposition to zirconia. As for the mixed powder after freeze-drying, gradual weight loss was observed until 530 °C and rapid weight loss was detected between 530 and 600 °C. We confirmed by XRD analysis that yttrium nitrate hydrate was decomposed to yttria (Y_2O_3) when yttrium nitrate hydrate was heated at 500 °C for 10 hours in air. The gradual weight loss of the mixed powder after freeze-drying until 530 °C was 38 mass % while the sum of weight loss by the decomposition to zirconia from zirconyl nitrate dihydrate and that to yttria from yttrium nitrate hydrate corresponded to 30 mass % at the mixed ratio. When all nitrates are decomposed to oxides, the total weight loss should be 50 mass %. Thus, we speculate that all zirconyl nitrate dihydrate and yttrium nitrate hydrate decomposed until 530 °C, and some barium nitrate remained at that temperature. The weight loss between 530

and 600 °C was 12 mass %, which means complete conversion of nitrate to oxides. Considering that the melting point of pure barium nitrate is 592 °C, the reaction between 530 and 600 °C should be written as

$$Ba(NO_3)_2\ (l) + 0.85\ ZrO_2\ (s) + 0.075\ Y_2O_3\ (s) \rightarrow BaZr_{0.85}Y_{0.15}O_{2.925}\ (s) + N_2\ (g) + 2.5\ O_2\ (g) \quad (9\text{-}1a)$$

and

$$BaO_2\ (s) + 0.85\ ZrO_2\ (s) + 0.075\ Y_2O_3\ (s) \rightarrow BaZr_{0.85}Y_{0.15}O_{2.925}\ (s) + 0.5\ O_2\ (g) \quad (9\text{-}1b).$$

The formation of the liquid phase should be a reason for the rapid weight loss between 530 and 600 °C. It was possible to obtain barium zirconate phase at temperatures higher than 530 °C.

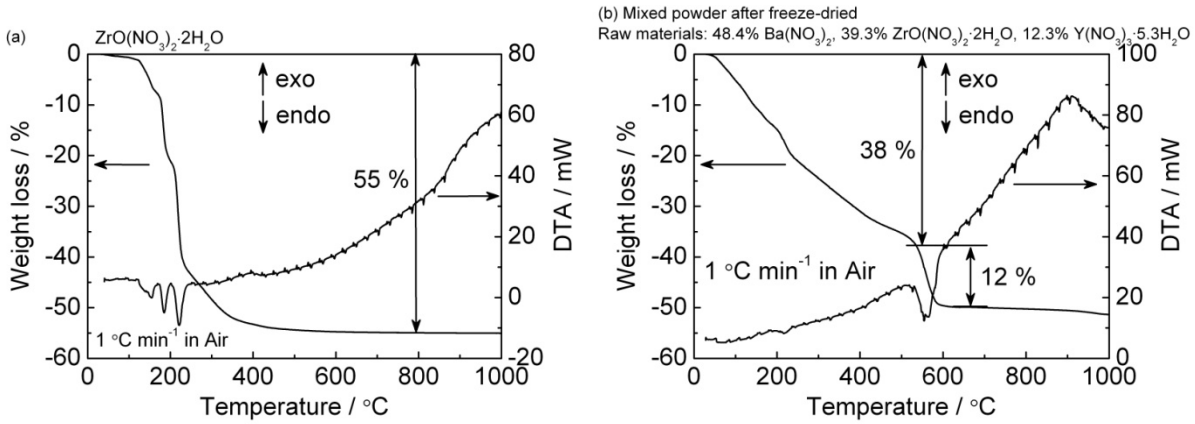

Figure 9.1 TG-DTA patterns of (a) zirconyl nitrate dihydrate powder, (b) freeze-dried precursor.

Figure 9.2 shows XRD patterns of synthesized powder heated at 400 to 1100 °C for 10 hours in air. At temperatures higher than 500 °C, barium zirconate phase was detected, but a small amount of barium carbonate or barium nitrate was identified. At temperatures higher than 1000 °C, complete reaction was confirmed. The temperature of 1000 °C is lower than that by a solid state reaction method, 1300 °C. However, the particle size of the yttrium-doped barium zirconate obtained by nitrate freeze-drying method and synthesizing at 1000 °C in air

was larger than that obtained by the solid state reaction method combined with long time ball-milling as shown in Fig. 9.3, and the relative density of the sintered pellet using the powder synthesized at 1000 °C in air was very low (79.6 %). The reason for the large particle size might be related to the formation of liquid phase of barium nitrate.

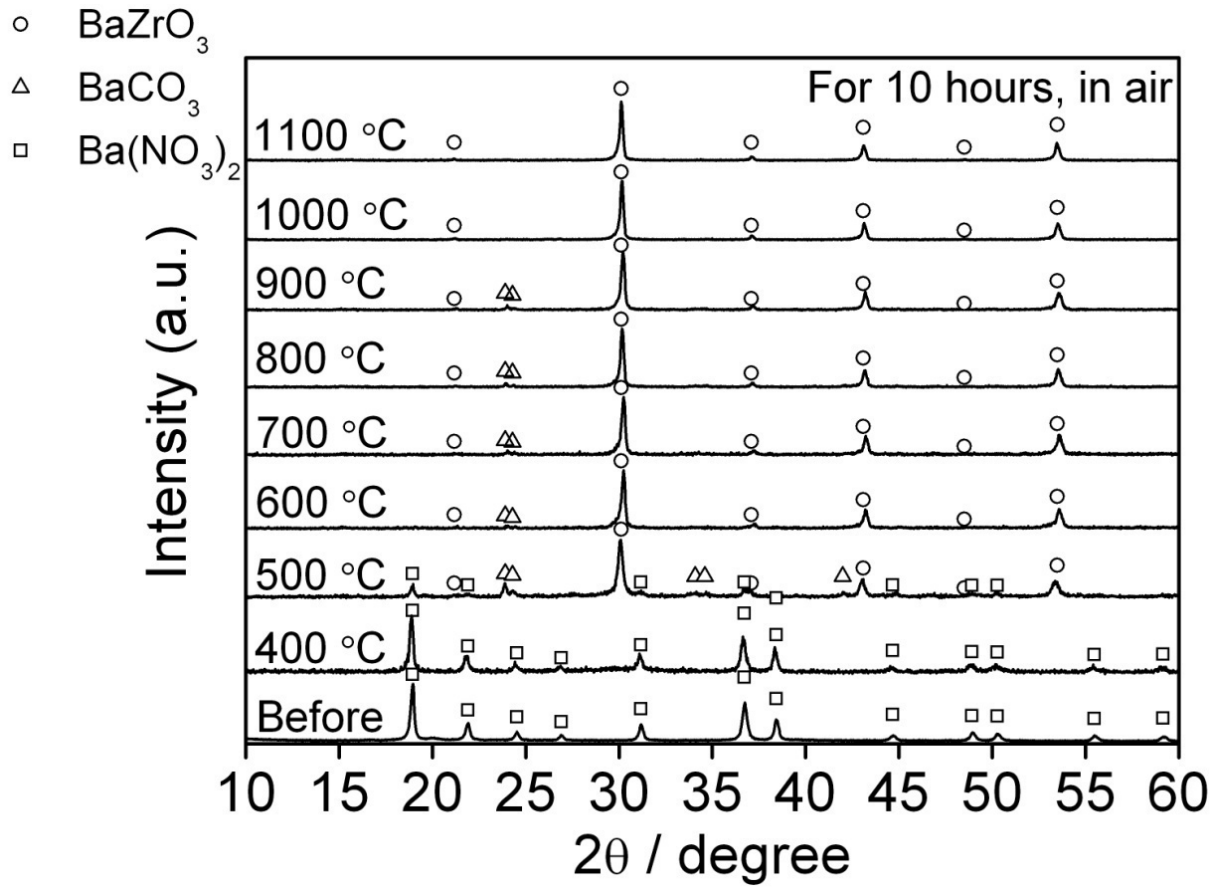

Figure 9.2 XRD patterns of synthesized powder obtained by nitrate freeze drying method and heated at 400 to 1100 °C for 10 hours in air.

To prevent barium nitrate from melting, the powder mixed by nitrate freeze-drying method was heated in a vacuum (~10^{-5} atm) in order to decompose barium nitrate to barium oxide (BaO) which has a higher melting point, 2013 °C, than barium nitrate. Fig. 9.4 shows XRD patterns of powders obtained by nitrate freeze-drying method and synthesizing at 400 to 600 °C for 10 hours in a vacuum with XRD patterns of yttrium-doped barium zirconate powder obtained by solid state reaction method at 1300 °C for 10 hours in air and ball-milling

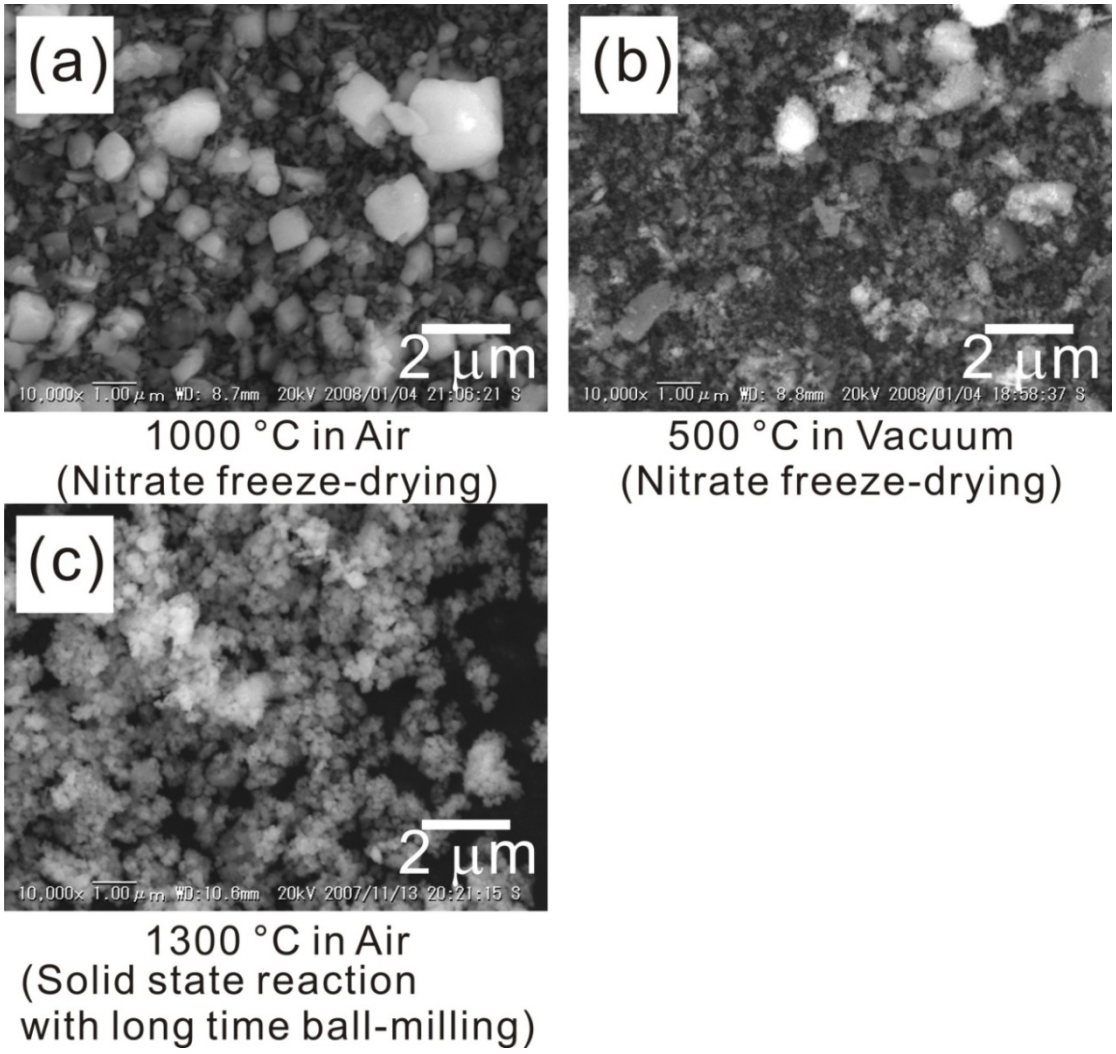

Figure 9.3 SEM image of yttrium-doped barium zirconate powders obtained by nitrate freeze-drying method and synthesis (a) at 1000 °C for 10 hours in air, (b) at 500 °C for 10 hours in vacuum with (c) yttrium-doped barium zirconate powder obtaineded by solid state reaction method at 1300 °C for 10 hours in air and ball-milling for 100 hours.

for 100 hours. At temperatures higher than 500 °C, only barium zirconate phase was identified and the particle size of the yttrium-doped barium zirconate powder obtained by nitrate freeze-drying method and synthesizing at 500 °C for 10 hours in vacuum was much finer than that at 1000 °C in air as shown in Fig. 9.3, and the particle size was about 30 nm as shown in the photograph of TEM in Fig. 9.5 (a). This implies that, in a vacuum at 500 °C, barium nitrate was decomposed to barium oxide and the formation of liquid phase was avoided.

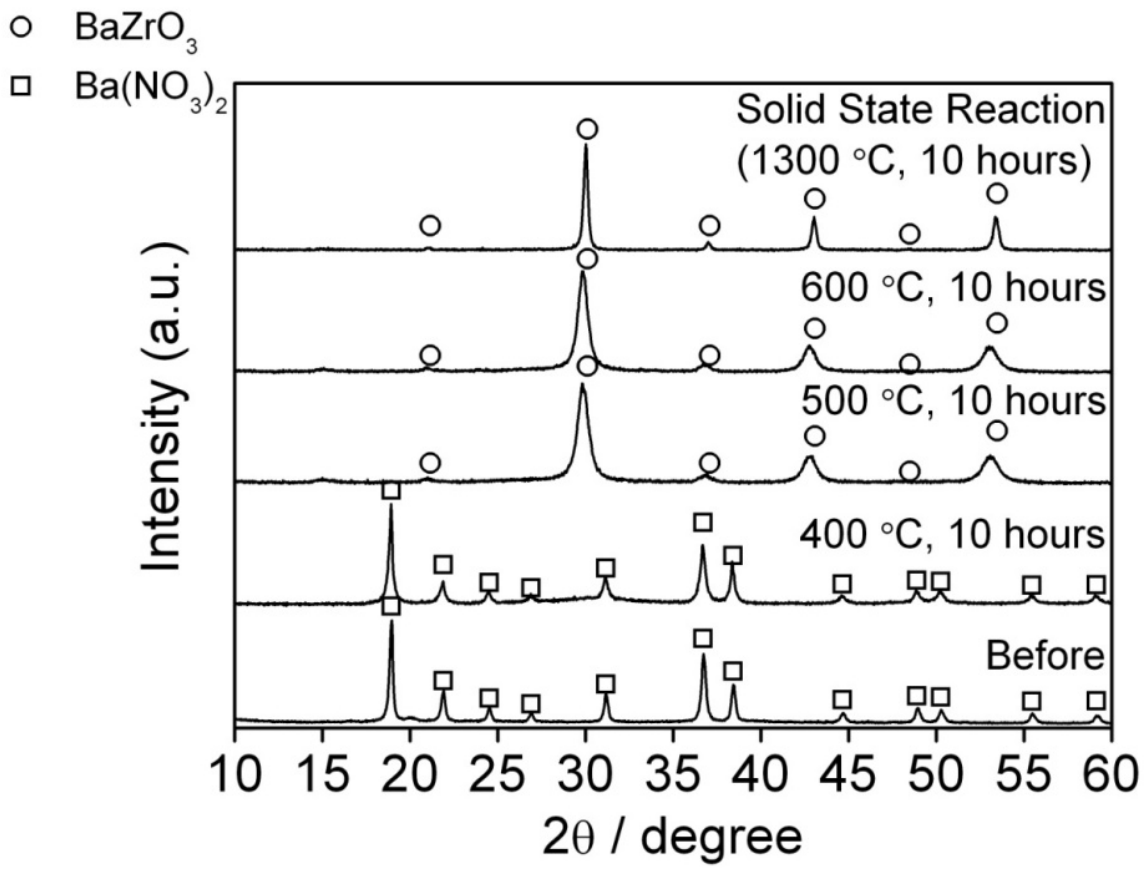

Figure 9.4 XRD patterns of powders obtained by nitrate freeze-drying method and synthesis at 400 to 600 °C for 10 hours in vacuum with XRD patterns of yttrium-doped barium zirconate powder obtained by solid state reaction method at 1300 °C for 10 hours in air and ball-milling for 100 hours.

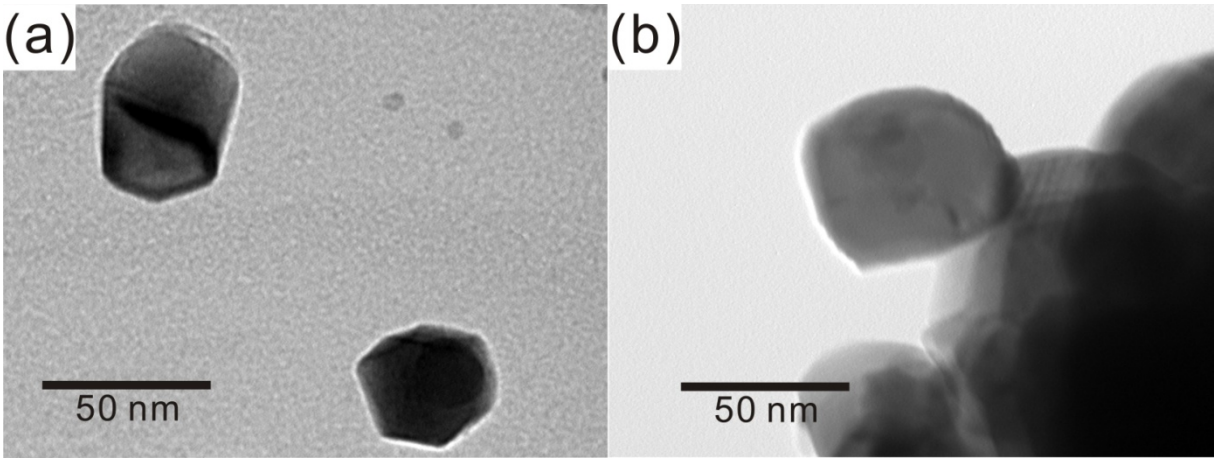

Figure 9.5 TEM image of $BaZr_{0.85}Y_{0.15}O_{3-\delta}$ powders (a) obtained by nitrate freeze-drying method and synthesis at 500 °C for 10 hours in vacuum and (b) obtained by solid state reaction method at 1300 °C for 10 hours in air and ball-milling for 100 hours.

The particle size of the yttrium-doped barium zirconate powder obtained by solid state reaction method at 1300 °C for 10 hours in air and ball-milling for 100 hours was about 40 nm as shown in the photograph of TEM in Fig. 9.5 (b). Thus, the particle size of the yttrium-doped barium zirconate powder obtained by nitrate freeze-drying method and synthesis at 500 °C for 10 hours in a vacuum was slightly finer than that from the solid state reaction method combined with 100 hours' ball-milling.

9.3.2 Sintering Behavior

Figure 9.6 shows cross-sectional SEM images of $BaZr_{0.85}Y_{0.15}O_{3-\delta}$ bars sintered for 4, 24 and 100 hours from powders synthesized at 500 °C for 10 hours in vacuum from the powder mixed by nitrate freeze-drying method with those by solid state reaction method, and the average grain size is summarized in Table 9.2. We obtained large and homogeneous grains in a shorter time by nitrate freeze-drying method. When we use powders by solid state reaction method at 1300 °C, 100 hours was needed to obtain large and homogeneous grains. In addition, precipitation of yttria was confirmed after sintering at 1600 °C for 100 hours. This is because of the high vapor pressure of barium oxide at 1600 °C as described in Chapter 6. The difference of particle size before the sintering between powder synthesized at 500 °C for 10 hours in vacuum from the powder mixed by nitrate freeze-drying method and powder obtained by solid state reaction method at 1300 °C for 10 hours in air and ball-milling for 100 hours was not so large. However, the sintering behavior was quite different. We consider that there is a phase separation of yttrium-doped barium zirconate in powders by solid state reaction method at 1300 °C but that there is no phase separation in powders synthesized at 500 °C in vacuum from the powder mixed by nitrate freeze-drying method, because the synthesis of yttrium-doped barium zirconate at low temperatures suppresses the phase separation kinetically. It is noted that no phase separation of barium zirconate was confirmed

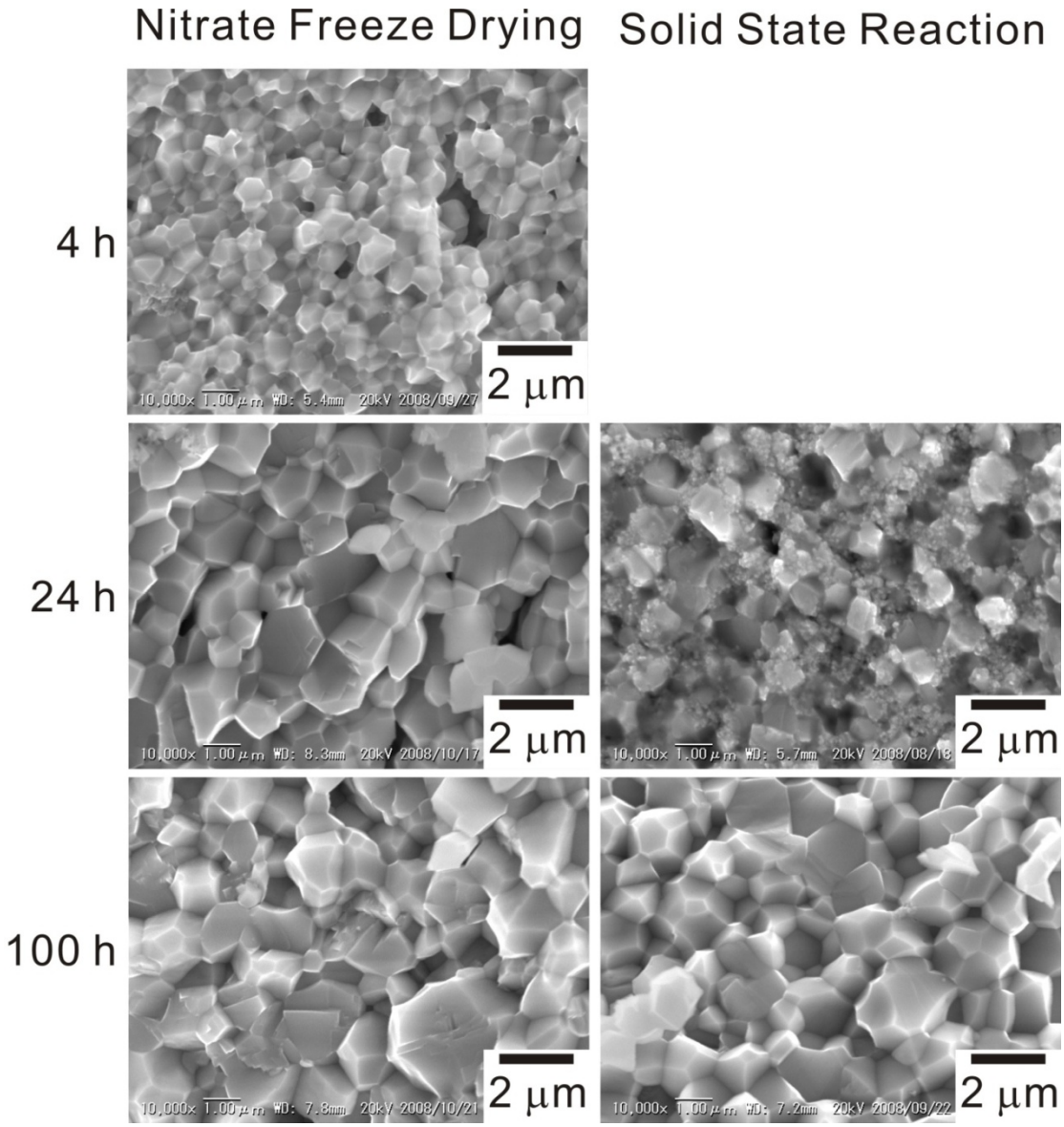

Figure 9.6 Cross-sectional SEM image of $BaZr_{0.85}Y_{0.15}O_{3-\delta}$ bars sintered for 4, 24 and 100 hours at 1600 °C from powders obtained by using nitrate freeze-drying method and synthesis at 500 °C for 10 hours in vacuum and by solid state reaction method at 1300 °C for 10 hours in air.

Table 9.2 Relative density, grain size, total conductivity at 600 °C and bulk conductivity at 80 °C of $BaZr_{0.85}Y_{0.15}O_{3-\delta}$.

Synthesizing method	Sintering hour (hours)	Relative density (%)	Grain size (μm)	σ_{bulk} at 80 °C (S cm^{-1})	σ_{total} at 600 °C (S cm^{-1})
Nitrate freeze-drying	4	85.0	0.51	2.0×10^{-5}	9.8×10^{-3}
Nitrate freeze-drying	24	97.4	0.92	1.9×10^{-5}	1.5×10^{-2}
Nitrate freeze-drying	100	99.0	1.06	2.3×10^{-5}	9.3×10^{-3}
Solid State Reaction	24	97.4	—	1.3×10^{-5}	9.4×10^{-3}
Solid State Reaction	100	100	1.00	2.0×10^{-5}	1.1×10^{-3}

in $BaZr_{0.85}Y_{0.15}O_{3-\delta}$ sintered for 24 hours by EDX analysis in all samples which had large and homogeneous grains.

9.3.3 Conductivity Measurement

It is easier to make a sample as a form of pellet than bar, but it was difficult to identify the arc due to grain-boundary at the left side of Arc 1 at 600 °C using a pellet by AC 2-terminal method as shown in Fig. 9.7. This is due to the similar capacitances of grain-boundary and electrode (Arc 1) and the high resistance of the electrode (Arc 1). Thus, conductivity measurement in bar form is still needed to determine the grain-boundary resistance at higher temperatures. Impedance spectra of $BaZr_{0.85}Y_{0.15}O_{3-\delta}$ for various sintering times and synthesizing methods at 80 °C for pellets and 600 °C for bars are shown in Fig. 9.8 (a) and (b), respectively. From the results in Chapter 2, the arc at the highest frequency region at 80 °C corresponds to bulk and that at 600 °C is due to grain-boundary, and the bulk conductivities at 80 °C and total conductivities at 600 °C are summarized in Table 9.2. From Fig. 9.8 (a), there is not a big difference among the diameters of arcs due to bulk except for the pellets sintered for 24 hours from powders synthesized by solid state reaction method, where the arc seems to overlap with two arcs. These two arcs might be arcs of two phases of low yttrium-doped barium zirconate and high yttrium-doped barium zirconate as discussed in Chapter 6. As for grain-boundary in Fig. 9.8 (b), the grain-boundary resistance of the bar sintered for 24 hours from powder synthesized at 500 °C for 10 hours in vacuum from the powder mixed by nitrate freeze-drying method was the lowest, while the resistance did not decrease drastically although grain size increased to 0.92 μm from 0.52 μm in the bar sintered for 4 hours. This might be because the inverse of grain-boundary resistance, $\frac{1}{R_{\text{g.b.}}}$, depends on

specific grain-boundary conductivity, $\sigma^{\circ}_{\text{g.b.}}$, and grain-boundary thickness, g, in addition to grain size, G, as shown in

$$\frac{L}{S}\frac{1}{R_{\text{g.b.}}} = \frac{G}{g}\sigma^{\circ}_{\text{g.b.}} \quad (9\text{-}3).$$

If grain-boundary thickness is assumed to be constant for any synthesis and sintering conditions, the specific grain-boundary conductivity has to change with samples because the value of $\frac{L}{S}\frac{1}{R_{\text{g.b.}}}$ did not change in spite of the change for the grain size. We hypothesized two reasons of reduction of specific grain-boundary conductivity as follows:

(1) Impurities such as sodium or silicon oxides precipitated at grain-boundaries. Sodium and silicon were confirmed by qualitative analysis by ICP-AES.

(2) Barium oxide preferentially vaporized at grain-boundaries during sintering because barium oxide has a significantly high vapor pressure at the sintering temperature, 1600 °C.

We investigated the reproducibility of grain-boundary resistances in the bar sintered for 24 hours from powders synthesized by the nitrate freeze-drying method, which showed the lowest grain-boundary resistance in this report. Three batches of $BaZr_{0.85}Y_{0.15}O_{3-\delta}$ (batch-1, 2 and 3) powder were synthesized at 500 °C for 10 hours in a vacuum from the powder mixed by the nitrate freeze-drying method and sintered for 24 hours in the form of bars. Fig. 9.8 (c) shows the impedance spectra at 600 °C and there is great variability in the grain-boundary resistance among batches. Considering this result, we think that both factors might contribute to the unclear behavior of specific grain-boundary conductivity. Thus, we first have to say that it is quite important to control the extent of impurities and reduce evaporation loss of barium oxide in samples in order to identify the reasons of reduction for the specific grain-boundary conductivity. Eventually, it leads to reduce high grain-boundary resistance.

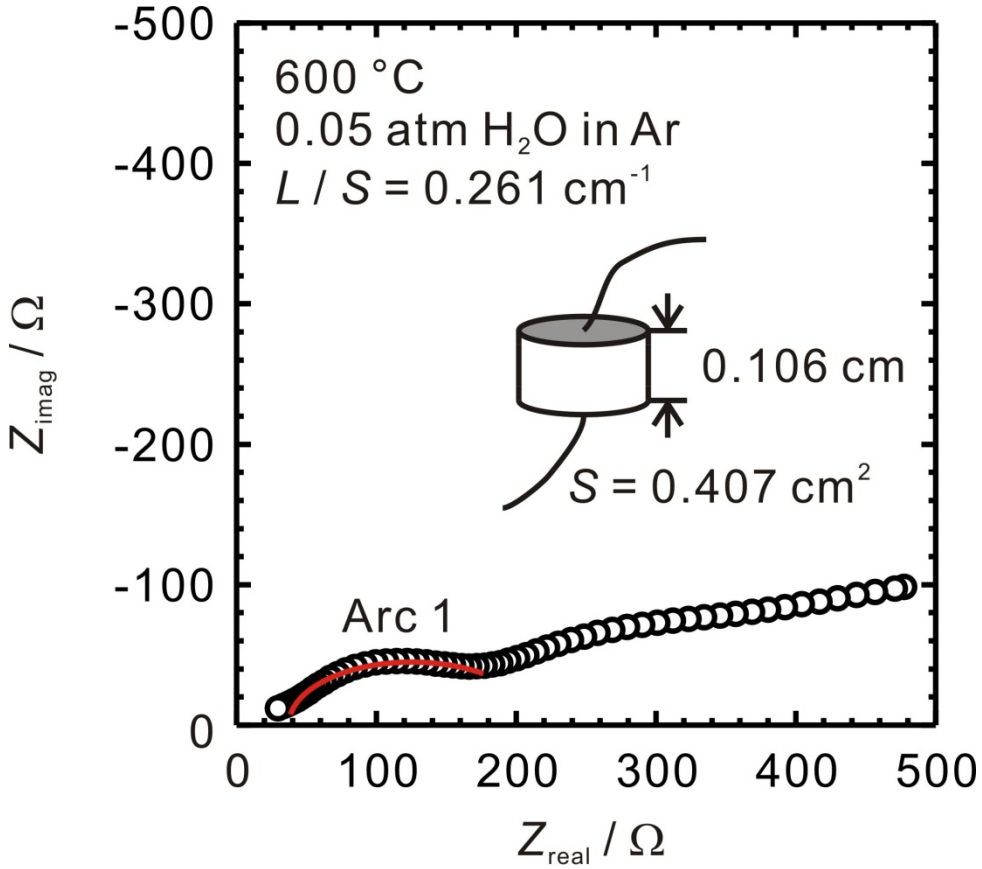

Figure 9.7 AC 2-terminal impedance spectrum at 600 °C in Ar-0.05 % H_2O using a pellet of $BaZr_{0.85}Y_{0.15}O_{3-\delta}$ sintered for 24 hours from powders obtained by using nitrate freeze-drying method and synthesis at 500 °C for 10 hours.

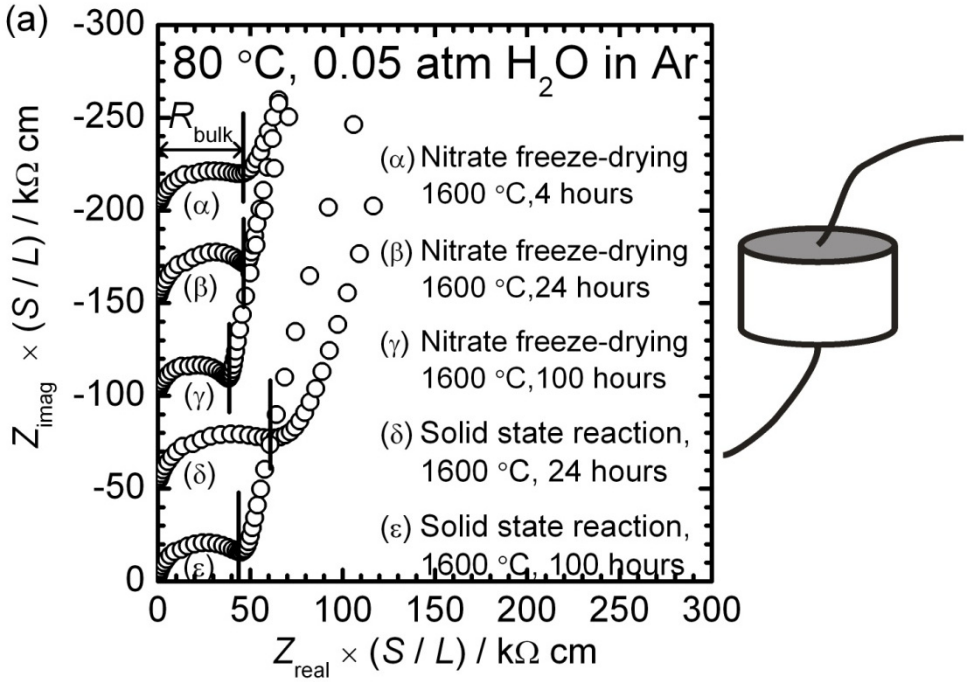

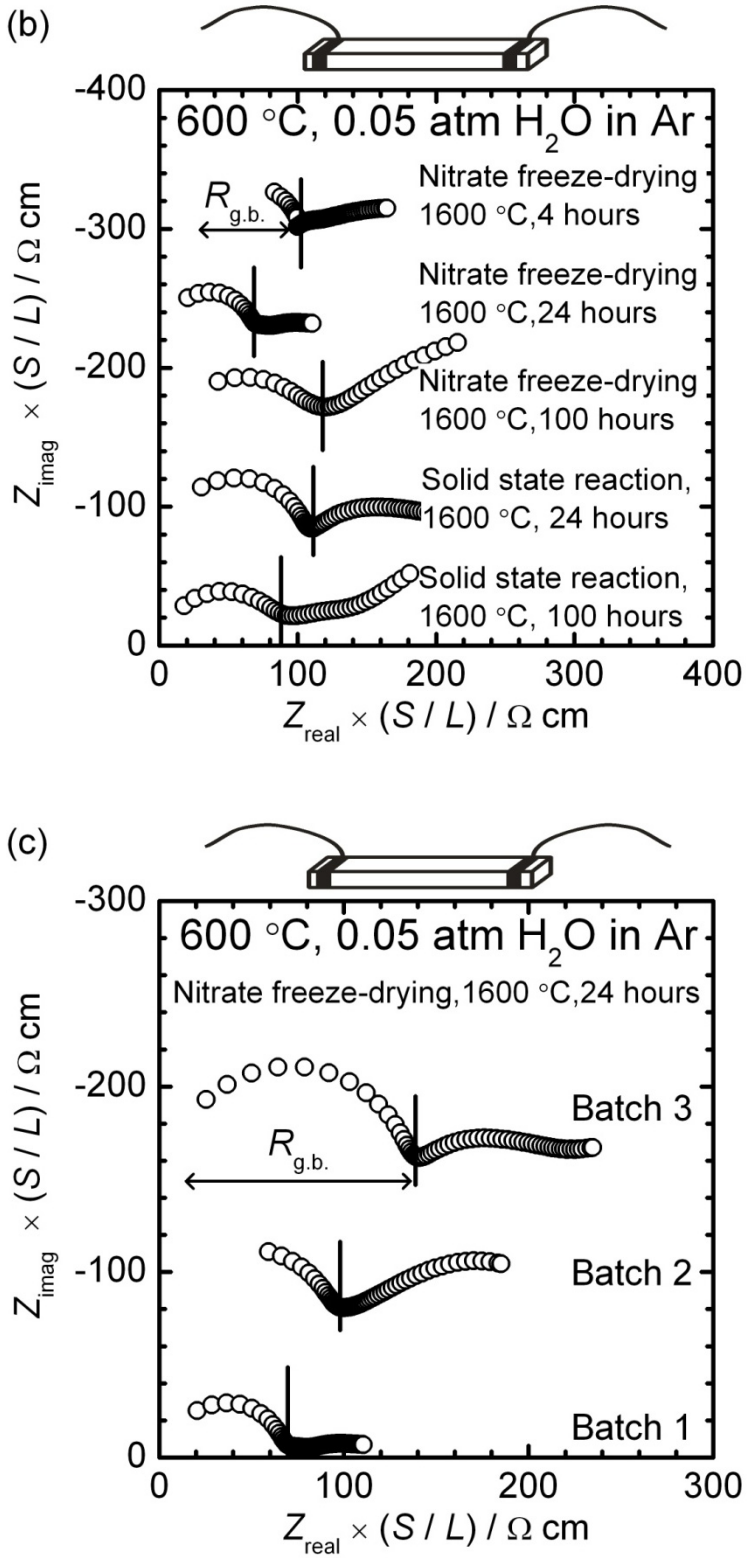

Figure 9.7 AC 2-terminal impedance spectra in Ar-0.05 % H_2O of $BaZr_{0.85}Y_{0.15}O_{3-\delta}$ at (a) 80 °C using pellets, (b) 600 °C using bars and (c) comparison of AC 2-terminal impedance spectra of three batches of $BaZr_{0.85}Y_{0.15}O_{3-\delta}$ sintered for 24 hours at 1600 °C from powders obtained by using nitrate freeze-drying method and synthesis at 500 °C for 10 hours. The sintering time and synthesis method are indicated in the figure.

9.4 Conclusions

The results obtained in this work can be summarized as follows:

(1) Very fine 15 % yttrium-doped barium zirconate powder was obtained by synthesizing at 500 °C in vacuum from powder mixed by nitrate freeze-drying method.

(2) Large and homogeneous grains of 15 % yttrium-doped barium zirconate are obtained using such very fine powders. Also, synthesis of yttrium-doped barium zirconate at low temperatures has a merit that it is possible to obtain a fine powder and suppress a phase separation of yttrium-doped barium zirconate.

(3) Grain-boundary resistance of the 15 % yttrium-doped barium zirconate was not improved although large and homogeneous grains were obtained. Specific grain-boundary conductivity might vary with samples. Also, there was not reproducibility of grain-boundary resistance in 15 % yttrium-doped barium zirconate sintered for 24 hours. Impurities and evaporation loss of barium oxide might affect the grain-boundary resistance in 15 % yttrium-doped barium zirconate and poor reproducibility of grain-boundary resistance.

References

[93Pot] H.S. Potdar, S.B. Deshpande, P.D. Godbole, and S.K. Date, *Journal of Materials Research*, **8** (5), 948-950 (1993).

[95Pfa] G. Pfaff, *Materials Letters*, **24**, 393-397 (1995).

[96Mch] J.M. McHale, P. C. McIntyre, K. E. Sickafus, and N. V. Coppa, *Journal of Materials Research*, **11** [5], 1199-1209 (1996).

[98Mar] L.I. Martynenko, O.A. Shlyakhtin, S.V. Milovanov, S.I. Gorel'skii, and D.O. Charkin, *Inorganic Materials*, **34** (5), 598-602 (1998).

[99Tag] G. Taglieri, M. Tersigni, P.L. Villa, and C. Mondelli, *International Journal of Inorganic Materials*, **1**, 103-110 (1999).

[00Vei] M. Veith, S. Mathur, N. Lecerf, V. Huch, and T. Decker, *Journal of Sol-Gel Science and Technology*, **15**, 145-158 (2000).

[01Gro] B. Grob, C. Beck, F. Meyer, T. krajewski, R. Hempelmann, and H. Altgeld, *Solid State Ionics*, **145**, 325-331 (2001).

[02Sin] A. Sin, B.El Montaser, and P. Odier, *Journal of the American Ceramic Society,* **85** [8], 1928-1932 (2002).

[02Kol] Yu.V. Kolen'ko, A.A. Burukhin, B.R. Churagulov, N.N. Oleinikov, and A.S. Vanetsev, *Inorganic Materials*, **38** (3), 252-255 (2002).

[02Aza] A-M. Azad, S. Subramaniam, T.W. Dung, *Journal of Alloys and Compounds*, **334**, 118-130 (2002).

[03Bos] F. Boschini, B. Robertz, A. Rulmont, and R. Cloots, *Journal of the European Ceramic Society*, **23**, 3035-3042 (2003).

[04Mag] A. Magrez, and T. Schober, *Solid State Ionics*, **175**, 585-588 (2004).

[07Bab] P. Babilo, T. Uda and S. M. Haile, *Journal of Materials Research*, **22,** 1322-1330 (2007).

[07Cer] R.B. Cervera, Y. Oyama, S. Yamaguchi, *Solid State Ionics*, **178**, 569-574 (2007).

[07Mak] V. D. Maksimov, P. E. Meskin, and B. R. Churagulov, *Inorganic Materials*, **43** (9), 988-993 (2007).

[08Epi] A. D'Epifanio, E. Fabbri, E.DiBartolomeo, S. Licoccia, and E. Traversa, *Fuel Cells*, **8**, 69-76 (2008).

[08Hig] S. Higgins, N.M. Sammes, A. Smirnova, J.A. Kikner, and G. Tompsett, *Journal of Fuel Cell Science and Technology*, **5**, 011003 (2008).

Chapter 10

Summary

Trivalent cation doped barium zirconates show good proton conductivity in wet atmosphere. Also, they are stable in the presence of atmospheric levels of carbon dioxide and water. They therefore have a great potential for proton conductive electrolytes in fuel cells or steam electrolyzers. Yttrium (Y)-doped barium zirconate is known to have the highest bulk conductivity among the trivalent cation doped barium zirconates so far, and many researchers are working on Y-doped barium zirconate. However, the total resistance of yttrium-doped barium zirconates are still high for application for electrolytes in fuel cells, and it is known that the grain-boundary resistance of yttrium-doped barium zirconate is higher than the bulk resistance and that the total resistance is governed by the small grain-boundary resistance. Therefore, it is necessary to improve the low grain-boundary resistance of yttrium-doped barium zirconate. The microstructure of yttrium-doped barium zirconate, which was made by a solid state reaction method and sintered at a typical sintering temperature of 1600 °C, consists of two sizes of grains; large grain is about 1 μm and the other is about 50 nm. The existence of such fine grains means that the grain-boundary concentration which is the number of grain-boundary per unit volume is very high. Therefore, the grain-boundary concentration has to be reduced to improve the grain-boundary resistance.

In this study, several fundamental aspects were investigated to understand the effect of dopant on proton conductivity of accepter doped barium zirconates, from the viewpoint of phase relationship at synthesizing and sintering temperature, sintering mechanism and reduction of high grain-boundary concentration of doped barium zirconates. These results obtained in this study are summarized as follow.

Chapter 2

Impedance spectra obtained in AC 2-terminal measurement were interpreted by combining with the results of DC 4-terminal measurement, and we established the way of deciding a bulk and grain-boundary resistance of 15 % yttrium-doped barium zirconate by AC 2-terminal measurement. There were three arcs obtained by AC 2-terminal measurement. An arc which appears at the highest frequency region is due to bulk and an arc due to grain-boundary appears next to the arc due to bulk. An arc due to electrode appears at the lowest frequency region. We also examined the dependence of oxygen partial pressure on total conductivity of $BaZr_{0.85}Y_{0.15}O_{3-\delta}$ at 600 °C under wet atmosphere. In the region of $p_{O2} < 3 \times 10^{-5}$ atm, proton conduction was dominant. When $p_{O2} > 10^{-2}$ atm, hole conduction appeared in addition to proton conduction. Also, we found that grain-boundary resistance is higher than bulk resistance and that total resistance is governed by grain-boundary resistance.

Chapter 3

The effects of various cations (Mg^{2+}, Sc^{3+}, In^{3+}, Yb^{3+}, Tm^{3+}, Er^{3+}, Y^{3+}, Ho^{3+}, Gd^{3+}, Nd^{3+}, La^{3+}, Bi^{3+} and Ga^{3+}) were examined as dopants into the B site of perovskite barium zirconate. The solubility of In, Yb, Tm, Er and Ho, whose ionic radii are close to that of zirconium ion, into B site is more than 0.075 ($X_{MO1.5} = 0.075$) at 1600 °C. In contrast, when there is a large difference of ionic radii between trivalent cations (Nd^{3+}, La^{3+}, Bi^{3+} and Ga^{3+}) and zirconium ion, the solubility of trivalent cations into barium zirconate is less than $X_{MO1.5} = 0.075$. The microstructure of sintered pellets and their conductivity in wet atmosphere were investigated. We could divide dopants into two classes based on the extent of proton conductivity and microstructure; “Y-type” and “Sc-type” dopants. Yb, Ho, Er and Tm belong to “Y-type” dopants, which have microstructure of mixture of coarse and fine grains and

higher proton conductivity. In belongs to “Sc-type” dopants, which have well-grown grains and lower proton conductivity.

Chapter 4

Phase relationship of the BaO-ZrO_2-$YO_{1.5}$ system at 1500 and 1600 °C was examined in order to explain the sintering behavior of “Y-type” dopant doped barium zirconates. During establishing the phase diagram of a part of the pseudoternary phase diagram in the BaO-ZrO_2-$YO_{1.5}$ system at 1600 °C, we found a new compound (BZY424 phase). The composition of BZY424 phase seems to change from ~ 0.31 to ~ 0.40 in X_{BAO}, from ~ 0.16 to ~ 0.25 in X_{ZrO2} and from ~ 0.42 to ~ 0.53 in $X_{YO1.5}$. Diffraction patterns of BZY424 phase is similar to cubic barium zirconate phase ($BaZrO_3$(ss)). Also, the solubility of yttria into cubic barium zirconate is $X_{YO1.5}$ = 0.25 on the composition line where the mole fraction of barium oxide is 0.50 (X_{BaO} = 0.50) at 1600 °C.

Chapter 5

Phase relationship of the BaO-ZrO_2-$ScO_{1.5}$ system at 1300 and 1600 °C was examined in order to explain the sintering behavior of “Sc-type” dopant doped barium zirconates. According to the phase diagram of a part of the pseudoternary phase diagram in the BaO-ZrO_2-$ScO_{1.5}$ system at 1600 °C, the solubility of scandia into barium zirconate at 1600 °C is 0.29 in a mole fraction of scandia ($X_{ScO1.5}$) on the composition line where the mole fraction of barium oxide is 0.50. However, the solubility of scandia into barium zirconate is reduced with decreasing temperature and lies in between $X_{ScO1.5}$ = 0.10 and 0.20 at 1300 °C.

Chapter 6

There is a big difference of microstructure between “Y-type” dopant doped barium zirconates and “Sc-type” dopant doped barium zirconates which were synthesized by solid state reaction and sintered at 1600 °C for 24 hours. In order to explain the difference of sintering mechanism “Y-type” dopant doped barium zirconate and “Sc-type” dopant doped barium zirconate, we investigated microstructures of 15 % yttrium-doped barium zirconate and 15 % scandium-doped barium zirconate by changing sintering time. The conclusion is that differences of phase relationship between the sintering temperature (1600 °C) and synthesizing temperature (1300 °C) have an influence on the microstructures of doped barium zirconate. When phase relationship of doped barium zirconates between the sintering temperature and synthesizing temperature is different, the microstructure of the doped barium zirconates is bimodal because of kinetic reason of cation diffusion during sintering (“Y-type” dopant). On the other hand, when doped barium zirconates have the same phase relationship at between the sintering temperature and synthesizing temperature, grains of the doped barium zirconates is large and homogeneous because long-distance diffusion of cations is not needed for grain growth during sintering (“Sc-type” dopant).

Chapter 7

Yttrium-doped barium zirconate have the highest protonic conductivity among trivalent cation doped barium zirconates. However, the microstructure of yttrium-doped barium zirconate consists of mixture of coarse and fine grains, which cause the grain-boundary resistance high. On the other hand, the microstructure of scandium-doped barium zirconate consists of well-grown grains. However, the bulk conductivity of scandium-doped barium zirconate is much lower than that of yttrium-doped barium zirconate. Thus, if scandium and yttrium is co-doped to barium zirconate, the grain-boundary resistance might be

lower with keeping the high bulk conductivity of yttrium-doped barium zirconate. Scandium and yttrium co-doped barium zirconate ($BaZr_{0.85}Sc_xY_{0.15-x}O_{3-\delta}$ (x=0, 0.05, 0.075, 0.10, 0.15)) have been investigated in terms of phase relationship, microstructures, and proton conductivity. The bulk conductivity of the scandium and yttrium co-doped barium zirconate increased with the dopant ratio of yttria. $BaZr_{0.85}Sc_{0.05}Y_{0.10}O_{3-\delta}$ had the highest grain-boundary conductivity among the scandium and yttrium co-doped barium zirconates in this study. But, $BaZr_{0.85}Sc_{0.15}O_{3-\delta}$, $BaZr_{0.85}Sc_{0.10}Y_{0.05}O_{3-\delta}$, $BaZr_{0.85}Sc_{0.075}Y_{0.075}O_{3-\delta}$ and $BaZr_{0.85}Sc_{0.05}Y_{0.10}O_{3-\delta}$ consisted of a single cubic perovskite phase at 1600 °C and their grain-boundary concentrations were smaller than that of $BaZr_{0.85}Y_{0.15}O_{3-\delta}$. From the observation of microstructure and results of grain boundary-conductivity measurement, we can say that yttrium is a dopant which increases specific grain-boundary conductivity and bulk conductivity, and scandium is a dopant which increases the grain size. Thus, there is a trade-off relation between the grain size and specific grain-boundary conductivity based on the mixing ratio of scandia to yttria. The total conductivity of $BaZr_{0.85}Sc_{0.05}Y_{0.10}O_{3-\delta}$ at 600 °C was estimated to be 1.6×10^{-2} S cm^{-1}, which is the highest-class conductivity among reported trivalent cation-doped barium zirconates.

Chapter 8

The effects of isovalent cation substitution in yttrium-doped barium zirconate were examined. Substitution of titanium ion for zirconium ion and that of strontium ion for barium ion reduce the bulk conductivity and promote grain growth. Substitution of titanium ion for zirconium ion increases the difference of average ionic radius between host cation of B site (Zr^{4+} and Ti^{4+}) and dopant cation for B site (Y^{3+}), and substitution of strontium ion for barium ion decreases the average ionic radius of A site. Those make it easy that a part of the dopant cation dissolves into A site (Barium site), which might cause the reduction of bulk

conductivity. Well grown grains might be an evidence of the dissolution of the dopant cation into A site because it has been reported that extra barium oxide promotes grain growth.

Chapter 9

One of the ways to obtain large and homogeneous grains of yttrium-doped barium zirconate is to have a particle size of synthesized powder which is finer than that of synthesized powder by the solid state reaction method at 1300 °C. This is because the diffusion distance for cations in fine powder becomes short during sintering at 1600 °C. In this study, we employed the nitrate freeze-drying method for obtaining a fine powder of $BaZr_{0.85}Y_{0.15}O_{3-\delta}$ and investigated sintering property and conductivity of $BaZr_{0.85}Y_{0.15}O_{3-\delta}$. Very fine 15 % yttrium-doped barium zirconate powder was obtained by synthesizing powder obtained by nitrate freeze drying method at 500 °C in vacuum, and the particle size was about 30 nm. The particle size was not a big difference from powder obtained by solid state reaction method at 1300 °C for 10 hours in air and ball-milling for 100 hours (40 nm). However, large and homogeneous grains of 15 % yttrium-doped barium zirconate sintered at 1600 °C are easily obtained using the powder synthesized at 500 °C for 10 hours in vacuum from the powder mixed by nitrate freeze-drying method, although mixture of coarse and fine grains of 15 % yttrium-doped barium zirconate sintered at 1600 °C are obtained using the powder obtained by solid state reaction method at 1300 °C for 10 hours in air and ball-milling for 100 hours. From these results, synthesis of yttrium-doped barium zirconate at low temperatures has a merit that it is possible to obtain a finer powder and suppress a phase separation of yttrium-doped barium zirconate, while the powders by solid state reaction method at 1300 °C might have phase separation. Grain-boundary resistance of the 15 % yttrium-doped barium zirconate was not improved although large and homogeneous grains were obtained. Specific grain-boundary conductivity might vary with samples. Impurities and evaporation loss of

barium oxide might affect the grain-boundary resistance in 15 % yttrium-doped barium zirconate.

List of Publications

Papers

"A Pseudoternary Phase Diagram of the BaO-ZrO_2-$ScO_{1.5}$ System at 1600 °C and Solubility of Scandia into Barium Zirconate"

S. Imashuku, T. Uda, T. Ichitsubo, E. Matsubara and Y. Awakura

Journal of Phase Equilibria and Diffusion, **28** (6), 517-522 (2007).

"Sintering Properties of Trivalent Cation Doped Barium Zirconate at 1600 °C"

S. Imashuku, T. Uda, and Y. Awakura

Electrochemical and Solid-State Letters, **10** (10), B175-B178 (2007).

"Improvement of Grain-boundary Conductivity of Trivalent Cation-doped Barium Zirconate Sintered at 1600 °C by Co-doping Scandium and Yttrium"

S. Imashuku, T. Uda, Y. Nose, K. Kishida, S. Harada, H. Inui, and Y. Awakura

Journal of the Electrochemical Society, **155** (6), B581-B586 (2008).

"Dependence of Dopant Cations on Microstructure and Proton Conductivity of Barium Zirconate"

S. Imashuku, T. Uda, Y. Nose, G. Taniguchi, Y. Ito, and Y. Awakura

Journal of the Electrochemical Society, **156** (1), B1-8 (2009).

"Effect of Isovalent Cation Substitution on Conductivity and Microstructure of Sintered Yttrium-doped Barium Zirconate"

S. Imashuku, T. Uda, Y. Nose, Y. Ito, and Y. Awakura

Submitted to *Solid State Ionics*.

"Processing of Fine Powder, Sintering Behavior and Interpretation of Impedance Spectra for Yttrium-doped Barium Zirconate"

S. Imashuku, T. Uda, Y. Nose, and Y. Awakura

Submitted to *Journal of Materials Chemistry*.

Proceedings

"Conductivity Measurement of Scandium Doped Barium Zirconate for Fuel Cell Application"

S. Imashuku, T. Uda, and Y. Awakura

Sohn International Symposium on Advanced Processing of Metals and Materials: Principles, Technologies and Industrial Practice, 519-531 (2006).

"Improvement in Sintering of Barium Zirconate by Doping with Scandium"

S. Imashuku, T. Uda, and Y. Awakura

ECS Transactions - Solid Oxide Fuel Cells 10 (SOFC-X), **7**(1), 2321-2329 (2007).

"Improvement of Grain-boundary Conductivity of Trivalent Cation Doped Barium Zirconate"

S. Imashuku, T. Uda, and Y. Awakura

The 3rd International Conference Process Materials for Properties.

Oral Presentation

International congress

"Solubility of Scandium in Barium Zirconate and Electric Conductivity of Scandium Doped Barium Zirconate"

S. Imashuku, T. Uda, T. Ichitsubo, E. Matsubara and Y. Awakura

GIST/KAIST/Kyoto University/Tohoku University Joint Symposium on Materials Science

and Engineering for 21st Century, Kawatabi, Japan, July 2006.

"Conductivity Measurement of Scandium Doped Barium Zirconate for Fuel Cell Application"

S. Imashuku, T. Uda, and Y. Awakura

Sohn International Symposium on Advanced Processing of Metals and Materials, San Diego, U.S.A., August, 2006.

"Improvement of Grain-boundary Conductivity of Trivalent Cation Doped Barium Zirconate by Doping Scandium"

S. Imashuku, T. Uda, and Y. Awakura

The 58th Annual Meeting of the International Society of Electrochemistry, Banff, Canada, September, 2007.

"Grain-boundary Conductivity of Co-doped Barium Zirconate"

S. Imashuku, T. Uda, Y. Nose, and Y. Awakura

Joint Symposium on Materials Science and Engineering for the 21st Century, Hsinchu, Taiwan, October, 2007.

"Grain-boundary Conductivity of Trivalent Cation Doped Barium Zirconate"

S. Imashuku, T. Uda, Y. Nose, and Y. Awakura

International Symposium on Environment, Energy, and Materials, Otsu, Japan, December, 2007.

"Sintering Mechanism of $BaZr_{0.85}Y_{0.15}O_{3-\delta}$ and $BaZr_{0.85}Sc_{0.15}O_{3-\delta}$"

S. Imashuku, T. Uda, Y. Nose, and Y. Awakura

Joint Symposium on Materials Science and Engineering for the 21st Century, Gyeongju, Korea, September, 2008.

Domestic congress

"Improvement of sintering properties of barium zirconate by doping scandium"

S. Imashuku, T. Uda, and Y. Awakura

The 32nd Symposium on Solid State Ionics in Japan, Fukuoka, November, 2006.

"Conductivity of barium zirconate co-doped scandium and yttrium"

S. Imashuku, T. Uda, and Y. Awakura

The 74th meeting of the electrochemical society of Japan, Noda, April, 2007.

"Conductivity of barium zirconate co-doped scandium and yttrium"

S. Imashuku, T. Uda, and Y. Awakura

The 141st fall meeting of the Japan institude of metals, Gifu, September, 2007.

"Sintering Property, Phase Relationship, and Processing of B-site Doped $BaZrO_3$"

S. Imashuku, T. Uda, Y. Nose, and Y. Awakura

The 33rd Symposium on Solid State Ionics in Japan, Nagoya, December, 2007.

"Sintering property and processing of yttrium-doped barium zirconate"

S. Imashuku, T. Uda, Y. Nose, and Y. Awakura

2008 spring meeting of the mining and materials processing institute of Japan, Tokyo, March, 2008.

"Interpretation of Impedance Spectrum in Barium Zirconate"

S. Imashuku, T. Uda, Y. Nose, and Y. Awakura

2008 fall meeting of the mining and materials processing institute of Japan, Sendai, October, 2008.

Poster Presentation

International congress

"Solubility of Scandium in Barium Zirconate and Electric Conductivity of Scandium Doped Barium Zirconate"

S. Imashuku, T. Uda, T. Ichitsubo, E. Matsubara, and Y. Awakura

2nd International Symposium on New Materials Science, Kyoto, Japan, September, 2006.

"Processing and Microstructure of Doped Barium Zirconate and its Phase Relationship"

S. Imashuku, T. Uda, T. Ichitsubo, E. Matsubara, and Y. Awakura

The 2nd Summer Seminar on Nanoionics, Tsuna, Japan, September, 2006.

"Improvement in Sintering of Barium Zirconate by Doping with Scandium"

S. Imashuku, T. Uda, and Y. Awakura

Tenth International Symposium on Solid Oxide Fuel Cells (SOFC-X), Nara, Japan, June, 2007.

"Effect of Isovalent Cation Substitution on Conductivity and Microstructure of Sintered Yttrium-doped Barium Zirconate"

S. Imashuku, T. Uda, and Y. Awakura

The 14th International Conference on Solid State Protonic Conductors (SSPC-14), Kyoto, Japan, September, 2008.

Domestic congress

"Solubility of Scandium in Barium Zirconate and Electric Conductivity of Scandium Doped Barium Zirconate"

S. Imashuku, T. Uda, T. Ichitsubo, E. Matsubara, and Y. Awakura

The 73rd meeting of the electrochemical society of Japan, Hachioji, April, 2007.

Acknowledgements

I would like to express my gratitude to Professor Yasuhiro Awakura for his comments and advice in discussion as well as his sincere encouragement throughout the work. I am deeply grateful to Associate Professor Tetsuya Uda for his patient support and tireless support throughout the course of my thesis work. His advice was very helpful for my career as a researcher, and I am really happy to work with him. I also would like to thank Assistant Professor Yoshitaro Nose for his frequent and helpful suggestion. I am obliged to Mr. Tokuji Tanaka for his assistance in experimental works.

I am grateful to Professor Isao Tanaka and Professor Hiroyuki Sugimura for their helpful support. I would like to express my gratitude to Professor Eiichiro Matsubara and Associate Professor Tetsu Ichitsubo for letting me use FE-SEM. I would like thank Professor Haruyuki Inui, Associate Professor Kyosuke Kishida, Mr. Shunta Harada and Mr. Kengo Goto for their help with TEM images. I also express my acknowledgement to Mr. Kenji Kazumi for TEM images. I am obliged to Mr. Teruyoshi Unesaki for his technical support. I am deeply indebted to Professors S. Yamaguchi of the University of Tokyo, S.M. Haile of the California Institute of Technology and T. Omata of Osaka University for their aid in the scientific discussion of this work. I would like to thank Daiichi Kigenso Kagaku Kogyo Co., Ltd and Shin-Etsu Chemical Co., Ltd for the supply of zirconia powder and yttria powder, respectively.

I am grateful to Mr. Gennichi Taniguchi, Mr. Yuji Ito, Mr. Koichi Suehiro, Mr. Takafumi Katakami, Mr. Yusuke Okumura and Takaaki Tanaka for their assistance and supports in the course of this work. Also, I express would like to express my gratitude to all other members of Professor Awakura's research group. Of course, I have to thank Kyoto University, and specially, Department of Materials Science and Engineering, for giving me such a wonderful opportunity to study.

Finally, I have to express my acknowledgement to my parents, Akio Imashuku and Kayoko Imashuku, for their support throughout my academic career, without which none of this work would have been possible. I would like to thank my brother, Hiroshi Imashuku, my grandfather, Kuranosuke Hayata, and my grandmothers, Hiroko Imashuku and Toku Hayata, for their support and continuous engagement.